Effect of Doping and Coating on Magnetic and Optical Properties of NiO Nanoparticles

by:

HUR ABBAS

(32-FBAS/PHDPHY/S-14)

Supervisor:

Dr. Kashif Nadeem
Associate Professor (Tenured)

Department of Physics

Faculty of Basic and Applied Sciences

International Islamic University, Islamabad

(2020)

i Condensed matter physics

ii Optical and Electronic material

iii Nanomaterial

Effect of Doping and Coating on Magnetic and Optical Properties of NiO Nanoparticles

by:

Hur Abbas

(32-FBAS/PHDPHY/S-14)

A thesis is submitted to

Department of Physics

for the award of the degree of

Doctor of Philosophy in Physics

Chairman
Department of Physics, FBAS
International Islamic University
Islamabad

Signature______________________________

Chairman, Department of Physics,

International Islamic University, Islamabad

Signature______________________________

Dean, Faculty of Basic and Applied Science

International Islamic University, Islamabad

Department of Physics

Faculty of Basic and Applied Sciences

International Islamic University, Islamabad

(2020)

Final Approval

It is certified that the work printed in this thesis entitled **"Effect of Doping and Coating on Magnetic and Optical Properties of NiO Nanoparticles"** by **Hur Abbas**, registration no. 32-FBAS/PHDPHY/S-14 is of sufficient standard in scope and quality for award of degree of PhD Physics from Department of Physics, International Islamic University, Islamabad, Pakistan.

Viva Voce Committee

Chairman (Physics) ______________________________

Supervisor ______________________________

External Examiner 1 ______________________________

External Examiner 2 ______________________________

Internal Examiner ______________________________

بسم الله الرحمن الرحيم

DEDICATED

To

My Parents

&

All Family Members

Declaration

It is hereby declared that the work presented in this thesis has not been copied out from any source, neither as a whole nor a part. Furthermore, work presented in this dissertation has not been submitted in support of any publication other than those included in this thesis, any other degree or qualification to any other university or institute and is considerable under the plagiarism rules of Higher Education Commission (HEC) of Pakistan.

Hur Abbas

(32-FBAS/PHDPHY/S-14)

Dated: 01-12-2020

Certificate

The thesis entitled **"Effect of Doping and Coating on Magnetic and Optical Properties of NiO Nanoparticles"** submitted by **Hur Abbas** in partial fulfilment of PhD degree in Physics has been completed under my guidance and supervision. I am satisfied with the quality of student's research work and allow him to submit this thesis for further process to graduate with Doctor of Philosophy degree from Department of Physics, as per IIU rules and regulations.

Dated: 01-12-2020

Supervisor

Dr. Kashif Nadeem

Associate Professor (Tenured)

Department of Physics,

International Islamic University,

Islamabad.

ACKNOWLEDGMENT

First and foremost, praises and thanks to the Almighty **ALLAH** for His showers of blessings throughout my research work to complete the research successfully. I am extremely thankful to the Holy Prophet **Hazrat MUHAMMAD (P.B.U.H) and His AHLEBAIT (A.S)** who forever provide me a torch of guidance. By virtue of their guidance, today I am able to carry out my research work and going to present it.

I would like to express my sincere gratitude to my supervisor **Dr. Kashif Nadeem** for the continuous support during my Ph.D research. I would also like to acknowledge the Higher Education Commission of Pakistan (HEC) for providing funding grant to work at The University of Western Australia and University of New South Wales, Sydney, Australia in collaboration. I would also like to thank Australian Government for providing opportunity and research grant to work at the Australian Nuclear Science and Technology Organization (ANSTO) to conduct a very sensitive Neutron beam experiments. It is a matter of great pleasure and honor to express my gratitude to **Prof. Dr. Mikhail Kostylev, Prof. Dr. Clemens Ulrich, Dr. James Hestler and Prof. Dr. Heniz Krenn,** for valuable discussion and measurements. I shall express my heartiest thanks to all my research colleagues especially **Dr. Faisal Zeb, Khalid Khan, Zareef Khan, Adnan Razzaq, Naman Noshahi** and all other lab fallows including **Noman Saeed, Zafar Iqbal, Farhan Farooq** for being very supportive and co-operative all throughout my research work. I would also like to thank **Dr. Sajjad Ahmed, Dr. Fazal Abbas, Sibt ul Hassan, Jabir Zamir, Umer Farooq** for their help and moral support during research work.

I am very much thankful to my father **Safdar Hussain,** my mother **Haleema Bibi**, my brothers **Taswar Abbas** and **Muhammad Wasi Haider**, my sisters and especially my wife for continuous support through difficult times of my research. I would also like to thank my all other family members including my daughters **Eshaal Zainab** and **Anaya Zainab**, who prayed for my success. May ALLAH Almighty bless all of them.

Hur Abbas

List of Publications from Thesis

[1]. "Photocatalytic activity and two-magnon behavior in nickel oxide nanoparticles with different silica concentration"

Hur Abbas, K. Nadeem, N. Saeed, A. Hassan, S. Rahman, H. Krenn, and I. Letofsky-Papst

*Journal of Applied Physics **125**, 144305 (2019).* Impact Factor: 2.32

[2]. "A Comparative study of Magnetic, Photocatalytic and Dielectric Properties of NiO nanoparticles Synthesized by Sol-gel and Composite Hydroxide Mediated Method"

Hur Abbas, Kashif Nadeem, Abdul Hafeez, Ather Hassan, Noman Saeed, Heinz Krenn

*Ceramics International **45**, 17289-17297 (2019).* Impact Factor: 3.45

[3]. "Enhanced Photocatalytic activity of ferromagnetic Fe-doped NiO Nanoparticles"

Hur Abbas, K. Nadeem, A. Hassan, S. Rahman, H. Krenn

*Optik **202**, 163637 (2020).* Impact Factor: 1.914

[4]. "Magnetic homogeneity in Fe-Mn co-doped NiO nanoparticles"

Hur Abbas, K. Nadeem, H. Krenn, M. Kostylev, J. Hester, A. T. Murdock, S. Yick, Ilse-Letofsky Papst, C. Ulrich

Nanotechnology 31, 475701 (2020). Impact Factor: 3.551

[5]. "Unusual M-H loop splitting in core-shell NiO nanoparticles"

Hur Abbas, K. Nadeem, J. Hester, F. Perves, S. Yick, C. Ulrich, M. Kostylev, Ilse-Letofsky Papst, B. Ali, H. Krenn

Submitted to: Physical Review B. Impact Factor: 3.736 (2nd Revision in progress)

Other Publications as co-author

[6]. "Reduced surface spin disorder in ZrO_2 coated γ-Fe_2O_3 nanoparticles"

F. Zeb, M. Shoaib Khan, K. Nadeem, M. Kamran, **Hur Abbas**, H. Krenn, D.V. Szabo

*Solid State Communications **284–286**, (2018) 69–74.* Impact Factor: 1.549

[7]. "Comparison of temperature dependent magnetic properties of uncoated and SiO_2 coated $BaFe_{12}O_{19}$ nanoparticles"

K. Nadeem, J. Z. Minhas, F. Zeb, Misbah Sajjad, **Hur Abbas** and M. Zareef Khan

*Materials Research Express **6**, 116117 (2019).* Impact Factor: 1.449

[8]. "Vortex dynamics in $(NiFe_2O_4)_x$/CuTl-1223 nanoparticles-superconductor composites"

S. Ahmed, M. Z. Khan, K Nadeem, **Hur Abbas**, M. Mumtaz

*Physica B: Condensed Matter **581**, 411954 (2020).* Impact Factor: 1.874

[9]. "Comparison of surface effects in bare and titanium oxide coated $CoFe_2O_4$ nanoparticles"

M. Zareef Khan, K. Nadeem, F. Zeb, **Hur Abbas**, Basit Ali, I. Letofsky-Papst

*Solid State Sciences **103**, 106186 (2020).* Impact Factor: 1.435

[10]. "Magnetic phase diagram and dielectric properties of Mn doped $CoCr_2O_4$ nanoparticles"

K. Nadeem, Habib Ur Rehman, F. Zeb, E. Ali, M. Kamran, N.A. Noshahi, **Hur Abbas**

*Journal of Alloys and Compounds **832**, 155031 (2020).* Impact Factor: 4.175

[11]. "Ferrimagnetic to antiferromagnetic transition and complex impedance analysis of Cr-doped magnesium ferrite nanoparticles"

K. Khan, Z. Iqbal, **Hur Abbas**, A. Hassan, K. Nadeem

*Journal of Materials Science, Materials in Electronics **31**,* 8578–8588 *(2020).* Impact Factor: 2.195

Table of Contents

List of Figures

List of Tables

Abstract

In this dissertation, non-magnetic SiO_2 coating and single/co-doping effects on the magnetic and optical properties of NiO nanoparticle have been studied. SiO_2 coating has been preferred due to its chemical stability, bio-compatibility, non-toxic nature, adjustable pore diameter, chemical inertness and its ability to reduce the average crystallite size, agglomeration and dipolar interactions. The average crystallite size of NiO showed decreasing trend (57 to 14 nm) with increasing SiO_2 concentration. The diminishing 2M band with increasing SiO_2 concentration was attributed to generation of defects and achieving superparamagnetism in these nanoparticles. It was observed that the large SiO_2 concentration also behave as UV wave guiding medium that provided maximum energy to activate the NiO nanoparticles (NPs) as photocatalyst. The maximum net magnetization was observed for smallest (14 nm) obtained NiO NPs which was further magnetically investigated for the possible existence of core-shell magnetic structure. An unusual and novel M-H loop splitting at a particular temperature was observed which was attributed to the competing magnetic interactions between superparamagnetic, blocking and Néel transition states. These competing magnetic interactions induced concomitant slow magnetic relaxation which was confirmed by the field cooled relaxation experiments. The M-H loop splitting behavior was found to be particle size dependent and suppressed for diameters above and below 14 nm. Neutron diffraction confirmed the competing core-shell volume for this critical size of 14 nm. Doping with different metal ions also plays a key role in controlling the magnetic and optical properties of the NiO NPs. In the case of single doping, there is a tendency of cluster formation between transition metals that manipulate the observed magnetic nature of the host material. To observe the doping effect on the optical and magnetic properties, initially Fe was singly doped and then Fe-Mn were co-doped in NiO NPs. It has been observed that the increasing Fe doping concentration enhanced the photocatalytic activity of NiO NPs whereas net magnetization starts decreasing after 6% of Fe doping concentration in NiO. In Fe-Mn co-doped samples, cavity and broadband ferromagnetic resonance measurements showed the smaller structural and local magnetic inhomogeneity for 4%Mn-4%Fe co-doped NiO NPs. The M-H loops revealed the room temperature ferromagnetism like behaviour for higher Fe doping concentration and lower Mn doping concentration which was attributed to the

double exchange interactions. The neutron diffraction pattern confirmed the antiferromagnetic core of 4%Mn-4%Fe co-doped NPs which indicates the antiferromagnetic coupling of Fe^{2+}/Fe^{3+} and Mn^{2+} ions with Ni^{2+} ions by super-exchange interaction. Therefore, small and equal doping concentration of Fe and Mn in NiO NPs increase the magnetic homogeneity and reduces the structural defects that make it attractive for magnetic applications. Thus, both coating and doping in NiO nanoparticles are important for optical and magnetic applications.

CHAPTER NO. 1

INTRODUCTION

1.1 Magnetism

The magnetic nature of a material is characterized by placing it in an applied magnetic field. The nuclear spin creates much smaller magnetic moment due to large nucleon mass and can be neglected in comparison to electronic magnetic moment. The magnetic moment of electron originates mainly from the two types of motion, spin and orbital motion as depicted in Figure 1.1.

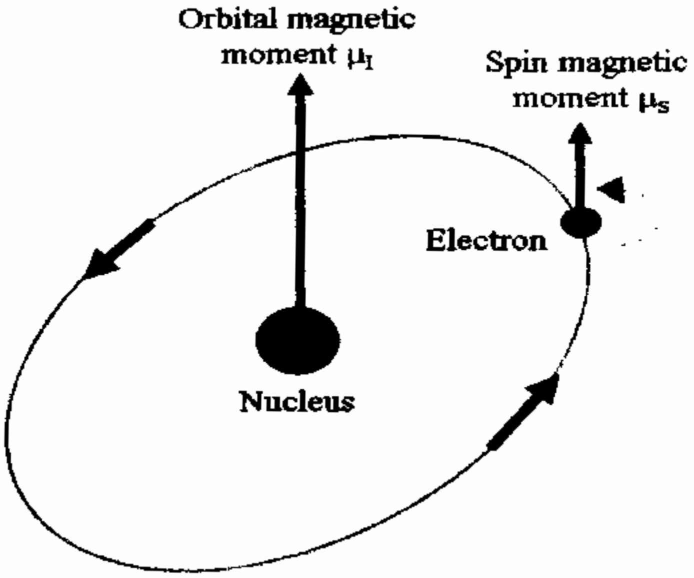

Figure 1.1: Spin and orbital motion of electron.

The contribution of electron's orbital motion to the magnetic moment is,

$$\mu_l = \frac{eL_l}{2m} \tag{1.1}$$

The angular momentum L is defined as the integral multiple of Plank's constant $\hbar$, i.e, $L = l\hbar$,

Therefore,

$$\mu_l = \frac{e\hbar}{2m} l \tag{1.2}$$

For $l = 1$, $$\frac{e\hbar}{2m} = \mu_B \tag{1.3}$$

Where, μ_B is called Bohr's magneton. The contribution of electron's spin motion to the magnetic moment is given by,

$$\mu_S = \frac{eS}{2m} \tag{1.4}$$

Where, $S = \pm\frac{\hbar}{2}$ is called spin quantum number. However, it is observed that the contribution to the spin magnetic moment is twice as the predicted value, therefore 'g' factor is introduced whose value is 1 for orbital motion and 2 for spin motion. The magnetic moment due to the proton and neutron is given by,

$$\mu_N = \frac{e\hbar}{2m_p} \cong \frac{e\hbar}{2m_n} \tag{1.5}$$

As the nucleus contains protons and neutron which are more massive than electrons, therefore the net magnetic moment contribution due to the nucleus is much smaller as compared to electrons which are much lighter in mass. The filled electronic shells with paired electrons have zero net magnetic moment. Therefore, the main contribution to the net magnetic moment is due to the spin motion of unpaired electrons. The net magnetization of material is directly proportional to the net magnetizing field and can be expressed as,

$$M = \chi H \tag{1.6}$$

1.2 Magnetic Materials

In the presence of applied magnetic field, the materials which show some magnetic response are classified as magnetic materials and can be categorized as diamagnetic, paramagnetic, ferromagnetic, ferrimagnetic, and antiferromagnetic materials.

1.2.1 Diamagnetic Materials

In this material, the direction of magnetic moment gets oppositely aligned to the applied magnetic field as stated by Lenz's law and shows negative susceptibility ($\chi < 0$). All materials contain weak diamagnetic effect due to their paired electrons in lower energy shells [1]. The materials with all filled electrons shell are diamagnetic such as helium and oxygen etc. are few of the examples of diamagnetic materials. Figure 1.2 depicts the response of a diamagnetic material without and with the applied magnetic field and also M-H loop.

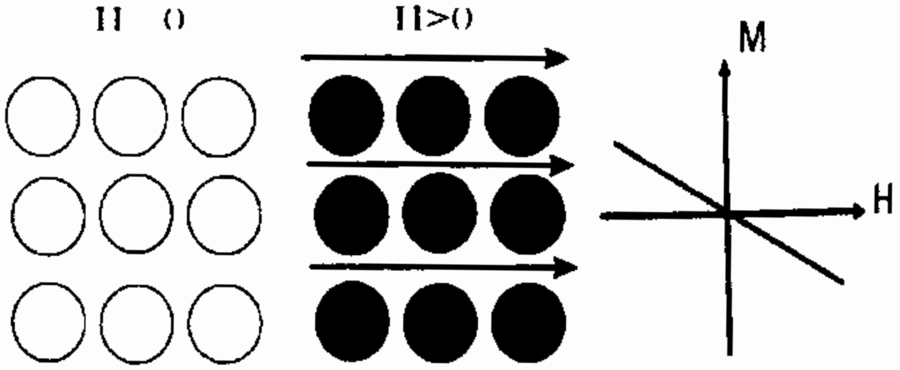

Figure 1.2: Diamagnetic behavior without and with applied magnetic field, and M-H loop.

1.2.2 Paramagnetic Materials

The paramagnetic materials contain randomly aligned magnetic moments in the absence of magnetic field. There is no exchange interaction (J=0) between magnetic moments and these materials do not retain magnetization after the removal of magnetic field. The paramagnetic materials have positive susceptibility ($\chi > 0$). Manganese, platinum, aluminium and potasium, etc are few of its examples. Figure 1.3 depicts the response of a paramagnetic material in the absence and presence of applied magnetic field with its M-H loop.

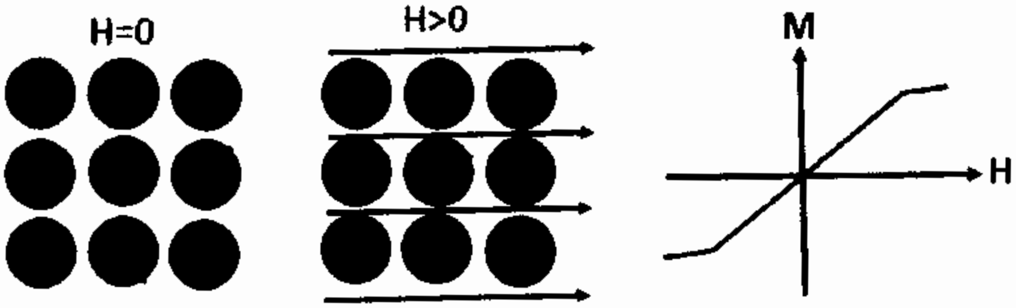

Figure 1.3: Paramagnetic behavior in the presence and absence of applied magnetic field and M-H loop.

1.2.3 Ferromagnetic Materials

These materials show permanent magnetic response to the applied magnetic field. The materials such as iron, cobalt, nickel and gadolinium are examples of it. Figure 1.4 depicts the behavior of ferromagnetic (FM) material with or without applied magnetic field.

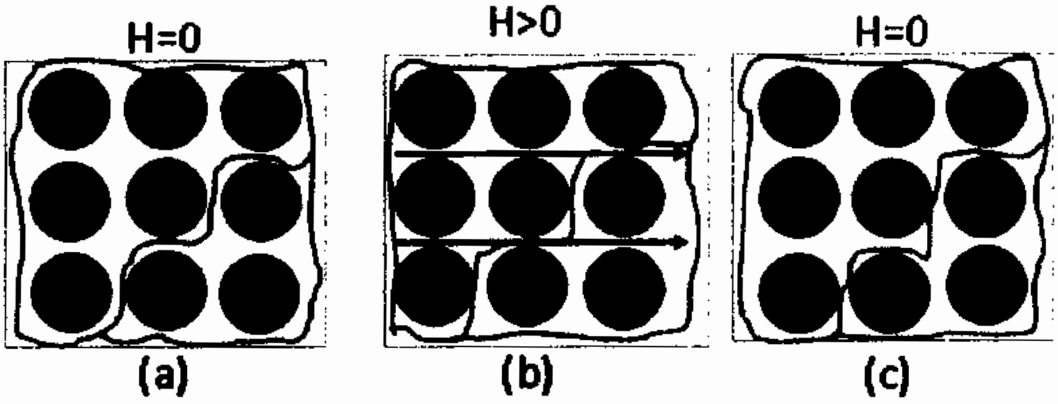

Figure 1.4: Magnetic response of FM material without and with applied magnetic field.

The magnetic dipole moment in a FM material is due the presence of unpaired electrons. In bulk FM material, number of FM domains exist ranging from 1 to 10^4 nm in dimension. These FM domains are responsible for the magnetization and contain $\sim 10^{15}$ to 10^{16} atoms. Each domain is separated from the neighboring domain by a boundary known as domain wall. Figure 1.4 (a) shows the random direction of two domains in the absence of applied magnetic field. However, when magnetic field is applied, magnetic domains aligned with the field and saturation is obtained as shown in Figure 1.4 (b). The magnetic response of a FM material in an external applied magnetic field is different from the paramagnetic and hysteresis phenomenon is observed in which magnetization lag behind the applied magnetic field [2]. After saturation, if magnetic field is removed, the magnetic moments remained in parallel alignment as shown in Figure 1.4 (c). Figure 1.5 depicts the M-H loop of FM material.

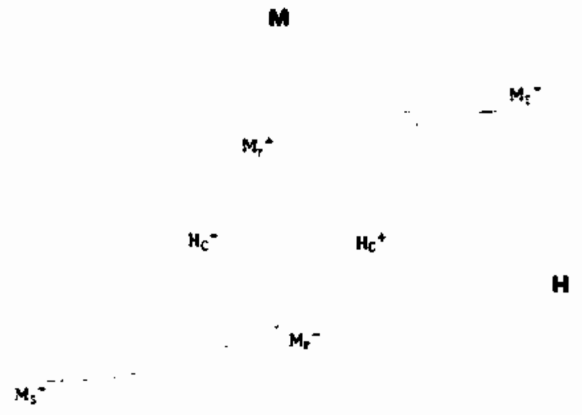

Figure 1.5: M-H loop of a FM material.

By increasing the DC magnetic field, magnetic dipoles starts aligning with the applied magnetic field and magnetization M reaches to a maximum possible value where it become independent of applied magnetic field and shows plateau is known as saturation magnetization (M_S). It gives the estimate of the total magnetization M of a given material. The value of M_S is calculated from the M-H loop as,

$$M_S = \frac{M_S^{+} + M_S^{-}}{2} \tag{1.7}$$

When saturation magnetization is achieved, the decrease in applied magnetic field from H to zero did not drop the magnetization form M_S to zero. However, there is some residual magnetization at $H = 0$, which is known as remnant magnetization (M_r). This phenomena is known as remanence or retentivity and considered as very important parameter for the data storage devices. The value of M_r from M-H loop is calculated as,

$$M_r = \frac{M_r^{+} + M_r^{-}}{2} \tag{1.8}$$

The value of coercive field (H_C) from M-H loop is calculated as,

$$H_C = \frac{H_C^{+} + H_C^{-}}{2} \tag{1.9}$$

The temperature at which the FM material turns into paramagnetic state is known as Curie temperature described by the Curie-Weiss law [3] given below:[1]

$$\chi = \frac{C}{T - T_C} \tag{1.10}$$

Above T_c, thermal energy ($K_B T$) overcomes the exchange coupling energy and magnetic moments behave as uncoupled (paramagnetic) [4].

1.2.4 Ferrimagnetic Materials

The materials which show magnetization similar to FM materials but smaller in magnitude are called ferrimagnetic (FiM) materials. It contains sublattices with magnetic dipoles having unequal magnitude and opposite direction and therefore have non-zero net magnetic moment. FiM materials also have magnetic domains, just like ferromagnetic materials. The difference between FM and FiM material is the exchange interactions which are positive in FM and negative in FiM. Figure 1.6 depicts the magnetic response of FiM

---

material without and with applied magnetic field. In the presence of very high field, magnetic moments of FiM material get aligned. However, it is usually not observed at laboratory scale magnetic field.

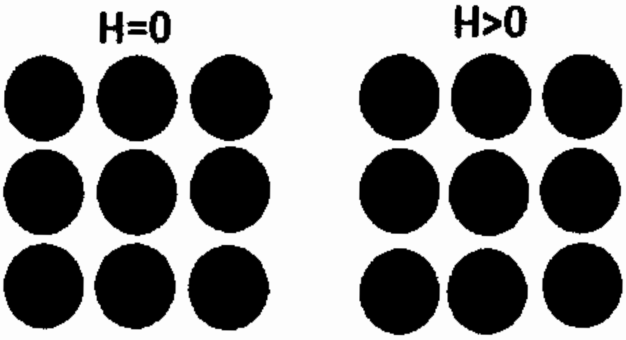

Figure 1.6: Magnetic response of FiM material without and with applied magnetic field.

1.2.5 Antiferromagnetic Materials

These materials have magnetic moment equal in magnitude but opposite in direction. Therefore, the net magnetic moment of an ideal bulk antiferromagnetic (AFM) material is zero when there is no magnetic field. However, when the magnetic field is applied, the spin flip and spin flop occur at higher applied magnetic field and a net magnetization can be observed in AFM material. The reason behind antiferromagnetism is due to the negative exchange integral first observed in MnO [5]. In NPs, the size gets reduced and surface disorder become large which ultimately affect the core. The AFM alignment of core gets disturb and some un-compensation induces in the antiparallel alignment of spins which result into a smaller net magnetization. Figure 1.7 demonstrates the response of an AFM material in the absence and presence of applied magnetic field.

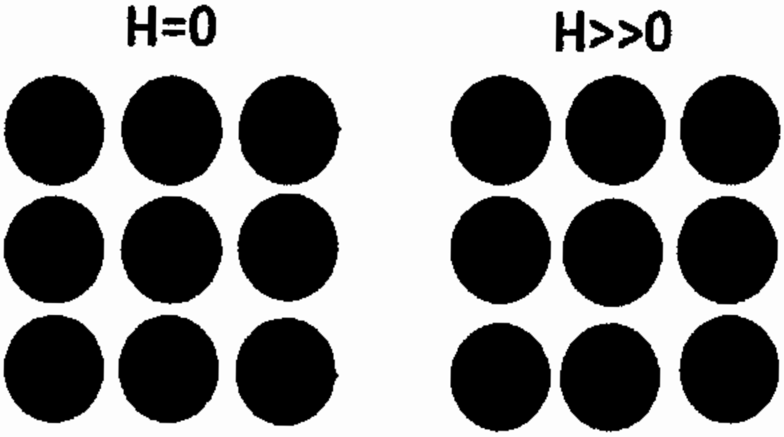

Figure 1.7: Magnetic response of an AFM material in the absence and presence of applied magnetic field.

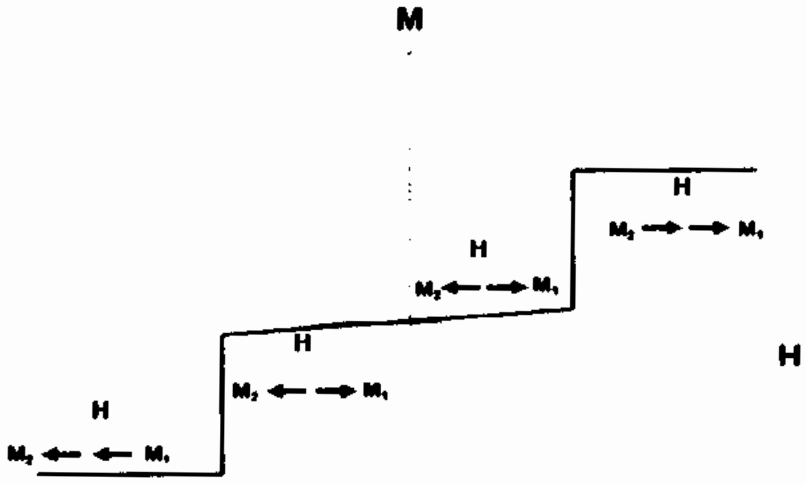

Figure 1.8: M-H loop of an AFM material.

Figure 1.8 shows the magnetization of an AFM material with varying applied magnetic field. The AFM material shows spin flip phenomenon which is described in detail in coming section.

1.3 Néel Temperature

The temperature at which the AFM material turns in to paramagnetic is known as Néel temperature (T_N). The relation that describe this phenomenon is known as Curie-Weiss law and magnetic susceptibility (χ) is given by [6].

$$\chi = \frac{C}{T+T_N} \qquad (1.11)$$

Above T_N, thermal energy overcome the exchange coupling energy between magnetic dipole moments and as a result magnetic dipole moments behave as uncoupled (paramagnetic). For bulk NiO, $T_N = 523\ K$, reported as highest among all monoxide AFM materials that possess cubic lattice structure [7]. The Néel temperature of nanostructured materials is reported to be lower than the bulk value due to the weak exchange coupling. The variation in particle size, lattice distortion, growth morphology and defect density are few of the factors which can affect the Néel temperature at nano-scale. Tadic *et al.* [8] reported $T_N = 56\ K$ for 5 nm NiO NPs dispersed in silica matrix which is much smaller value than bulk value ($523\ K$), due to existence of weak exchange interactions in these smaller sized NPs.

1.3.1 Spin Flip

If AFM material has large magneto-crystalline anisotropy (large anisotropy effective field H_A), then sublattices magnet moments M_1 and M_2 align antiparallel along easy axis up to coercive field H_C [9]. However, when the applied magnetic field (H) is increased form the coercive field H_C, sharp rotation of antiparallel spins (M_1) occur and all sub-lattices spins get directed to the applied magnetic field. As a result, sharp increase in net magnetization is observed as shown in Figure 1.9.

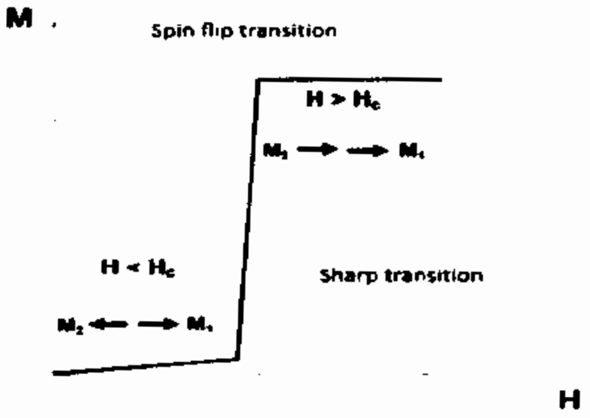

Figure 1.9: Spin flip mechanism in AFM material.

1.3.2 Spin Flop

If AFM material has smaller magneto-crystalline anisotropy (small anisotropy effective field H_A), then sublattices magnet moments M_1 and M_2 align antiparallel along relatively weak easy axis up to coercive field H_C. When applied magnetic field (H) starts increasing from the coercive field H_C, both the spins (M_1 and M_2) starts moving in the direction of applied magnetic field. Therefore, the saturation is not achieved suddenly as in the case of spin-flip transition [10] as shown in Figure 1.10.

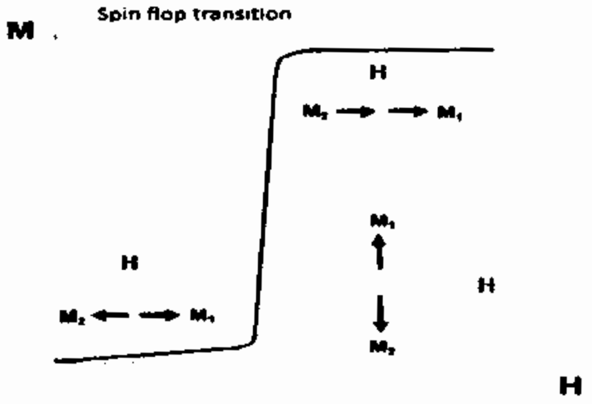

Figure 1.10: Spin flop mechanism in AFM material.

1.4 Exchange Interactions

The exchange interactions of electrons between atoms is due to Columbic interactions and responsible for the magnetic ordering in FM, AFM and FiM materials. Consider a system of two electrons (a and b) with wave function,

$$\psi(a,b) = \emptyset(\vec{r_1},\vec{r_2})\ \chi(a,b) \tag{1.12}$$

Where $\emptyset(\vec{r_1},\vec{r_2})$ is orbital part and symmetric and antisymmetric wave functions associated with it are,

$$\emptyset_{sy}(\vec{r_1},\vec{r_2}) = \frac{1}{\sqrt{2}}[\psi_a(\vec{r_1})\psi_b(\vec{r_2}) + \psi_a(\vec{r_2})\psi_b(\vec{r_1})] \tag{1.13}$$

$$\emptyset_{an}(\vec{r_1},\vec{r_2}) = \frac{1}{\sqrt{2}}[\psi_a(\vec{r_1})\psi_b(\vec{r_2}) - \psi_a(\vec{r_2})\psi_b(\vec{r_1})] \tag{1.14}$$

$\chi(a,b)$ is a spin part and has two states,

(i) **Singlet state (S=0) which has antisymmetric wave function χ_{an},**

$$\chi_{an}(a,b) = \frac{1}{\sqrt{2}}[\chi\uparrow(a)\,\chi\downarrow(b) - \chi\downarrow(a)\,\chi\uparrow(b)] \tag{1.15}$$

(ii) Triplet state (S=1) which has symmetric wave function χ_{sy}.

$$\chi_{sy}(a,b) = \frac{1}{\sqrt{2}}[\chi\uparrow(a)\,\chi\downarrow(b) + \chi\downarrow(a)\,\chi\uparrow(b)] \tag{1.16}$$

As electrons are fermions and all fermions have anti-symmetric wave function according to the Pauli's exclusion principle. Therefore, $\psi(a,b)$ should be overall anti-symmetric. For that,

$$\psi(a,b) = \begin{cases} \emptyset_{sy}(\vec{r_1},\vec{r_2})\ \chi_{an}(a,b) \\ \emptyset_{an}(\vec{r_1},\vec{r_2})\ \chi_{sy}(a,b) \end{cases} \tag{1.17}$$

Therefore, wave function associated with singlet state is,

$$\psi_S(a,b) = \frac{1}{\sqrt{2}}[\psi_a(\vec{r_1})\psi_b(\vec{r_2}) + \psi_a(\vec{r_2})\psi_b(\vec{r_1})]\chi_{an}(a,b) \tag{1.18}$$

Similarly, wave function associated with triplet state is,

$$\psi_T(a,b) = \frac{1}{\sqrt{2}}[\psi_a(\vec{r_1})\psi_b(\vec{r_2}) - \psi_a(\vec{r_2})\psi_b(\vec{r_1})]\chi_{sy}(a,b) \tag{1.19}$$

The Hamiltonian of two interacting electron system is,

$$\hat{H} = \hat{H}_a + \hat{H}_b + \hat{H}_{Exchange} \tag{1.20}$$

The two possible energy states of coupled electrons could be;

$$E_{Singlet} = \int \psi_S{}^* \hat{H} \psi_S \, dr_1 dr_2 \tag{1.21}$$

$$E_{Triplet} = \int \psi_T{}^* \hat{H} \psi_T \, dr_1 dr_2 \tag{1.22}$$

Now

$$E_{Singlet} - E_{Triplet} = \int \psi_S{}^* \hat{H} \psi_S \, dr_1 dr_2 - \int \psi_T{}^* \hat{H} \psi_T \, dr_1 dr_2 \tag{1.23}$$

After solving we have;

$$E_{Singlet} - E_{Triplet} = 2 \int \psi_a(\vec{r_1}) \psi_b(\vec{r_2}) \hat{H}_{ex} \psi_a(\vec{r_2}) \psi_b(\vec{r_1}) \, dr_1 dr_2 \tag{1.24}$$

$$J_{ex} = \frac{E_{Singlet} - E_{Triplet}}{2} = \int \psi_a(\vec{r_1}) \psi_b(\vec{r_2}) \hat{H}_{ex} \psi_a(\vec{r_2}) \psi_b(\vec{r_1}) \, dr_1 dr_2 \tag{1.25}$$

Where J_{ex} is the exchange interaction integral and defines the type of interaction present in the material [11]. The exchange energy $(\widehat{\mathcal{H}}_{ex})$ depends upon the spins operators $\widehat{S}_i$ and $\widehat{S}_j$ of both electrons,

$$\widehat{\mathcal{H}}_{ex} = -2J_{ex} (\widehat{S}_i \cdot \widehat{S}_j) \tag{1.26}$$

1.4.1 Direct Exchange Interactions

If $J_{ex} > 0$, then $E_S > E_T$, therefore spin magnetic moments are forced to align parallel and material is ferromagnetic.

If $J_{ex} < 0$, then $E_S < E_T$, therefore spin magnetic moments are forced to align anti-parallel and material is antiferromagnetic.

If $J_{ex} = 0$, then $E_S = E_T$, and spin magnetic moments may randomly align and material is paramagnetic.

All these magnetic interactions are called direct exchange interaction and considered as short range interactions with typical range of ~0.1 nm to 1 nm [12].

1.4.2 Indirect Exchange Interactions

The type of magnetic interactions in metal where conduction electrons play their part as mediator between atomic diploes are known as indirect exchange interactions. In these exchange interactions, the atomic dipoles get coupled over a large distance and may contain a large number of electrons as mediators. This is the dominant exchange interaction in metals where there is no direct exchange interaction exist between adjacent magnetic dipoles.

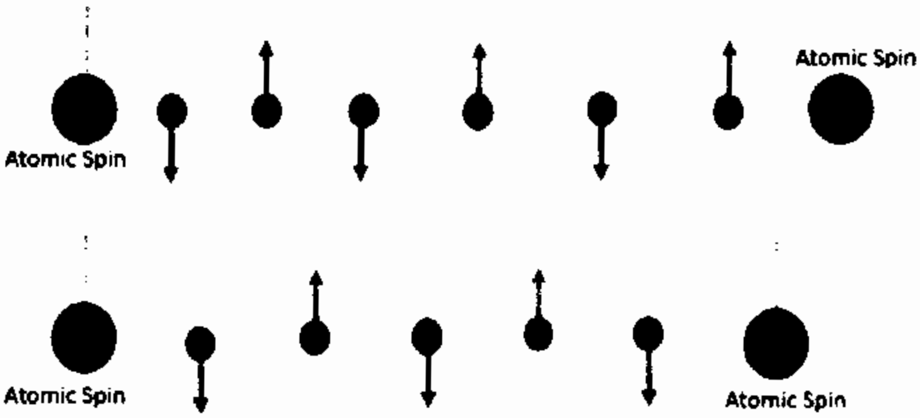

Figure 1.11: Indirect exchange interactions in metals.

In Figure 1.11, it is clear that the magnetic dipole induces spin polarization with neighbouring conduction electrons leading to indirect coupling of magnetic dipoles [13]. The distance between pair of magnetic dipoles decides whether the magnetic coupling will be parallel or antiparallel.

1.4.3 Super Exchange Interaction

The magnetic interactions which are present between the magnetic dipoles (mediated through non-magnetic ions, usually oxygen) are called super exchange interactions and found in many metal oxides. Let us take two metal Ni atoms A & B which are coupled via oxygen atom. The possible exchange coupling constants are, J_{A-O-A}, J_{A-O-B} and J_{B-O-B}. The ordering of "A" and "B" magnetic dipoles may be parallel or anti-parallel depending upon whether exchange integral is positive or negative [14]. Figure 1.12 shows the super-exchange interaction in two magnetic dipoles.

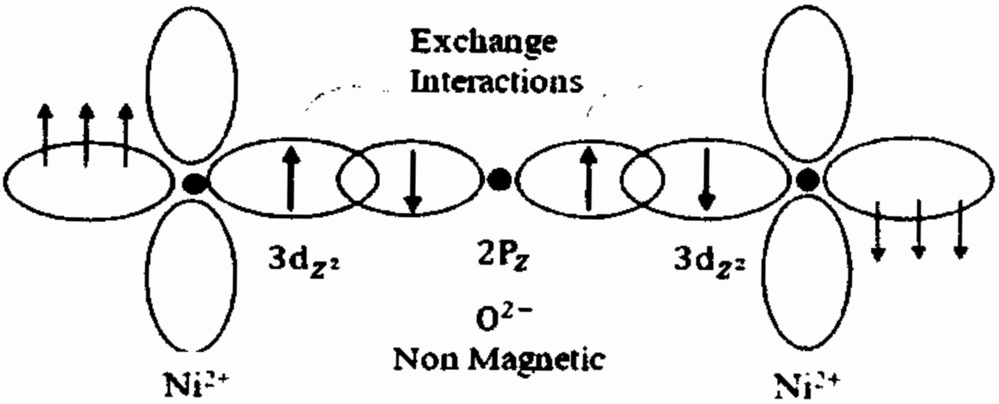

Figure 1.12: Super exchange interaction in magnetic dipoles.

The super-exchange interactions may depend on the following factors;

i Angles of $A-O-A$, $A-O-B, B-O-B$,

ii Separations between ions (bond lengths),

iii Symmetry of orbitals (d - orbital or p - orbital),

iv Distribution of cations and anions in structure (Positions of lattice sites "A" and "B").

1.5 Magnetic Properties of Nanoparticles

Magnetic properties of a bulk material change dramatically at the nanoscale. In NPs, surface to volume ratio become substantially high and surface dominated magnetic properties rule the whole nanoparticle's magnetization. The finite size, surface disordering and abstract geometry in NPs make it unique from magnetic point of view than other nanostructured materials. By decreasing the size of NPs, the net magnetic moment can become thermally unstable known as superparamagnetic size limit. In bulk AFM materials, net magnetic moment vanished due to equal and oppositely aligned magnetic moments. However in AFM NPs, some uncompensated magnetic moments present in the core and at the surface of NPs which results into net magnetization of the nanoparticle which increases on further reducing the particle size.

1.6 Magnetic Anisotropy and Nanoparticles

The net magnetic moment in a material has bias to stable along a particular direction known as magnetic anisotropy. The biased direction of magnetization depends on the crystal structure, shape of nanoparticle, residual stress, etc. and is known as easy axis of the magnetization. The total anisotropy (effective anisotropy, K_{eff}) is due to the contribution of some other anisotropies [15],

Therefore,

$$K_{\mathrm{eff}} = K_{\mathrm{Crystalline}} + K_{\mathrm{Stress}} + K_{\mathrm{Shape}} + K_{\mathrm{Surface}} + K_{\mathrm{Exchange}} \qquad (1.27)$$

For a spherical NPs, surface ($K_{surface}$) anisotropy is dominant [16]. Therefore, effective anisotropy (K_{eff}) for NPs can be given by,

$$K_{\mathrm{eff}} = K_{\mathrm{Bulk}} + \frac{6}{<D>} K_{\mathrm{Surface}} \qquad (1.28)$$

The factor "$\frac{6}{<D>}$" represents the average surface to volume ratio of a spherical nanoparticle. The energy required to rotate the net magnetic moment from its preferred direction to non-preferred direction is known as magnetic anisotropy energy. The total anisotropy energy (E_a) is the sum of all anisotropies energies given by;

$$E_a = E_{Crystalline} + E_{Shape} + E_{Stress} + E_{Surface} + E_{Exchange} \tag{1.29}$$

For the case of spherical NPs, surface ($E_{surface}$) anisotropy energy is dominant [17]. Therefore, the effective anisotropy energy (E_a) for the case of NPs is given by Stoner-Wohlfarth model given by;

$$E_a = K_{eff} V \sin^2\theta \tag{1.30}$$

The term $K_{eff}V$ represents the height of energy barrier between two stable minimum energy states at $\theta = 0$ and $\theta = \pi$ in which net magnetic moment fluctuates when gets some thermal energy (k_BT) [18]. The uniaxial anisotropy energy barrier is shown in Figure 1.13.

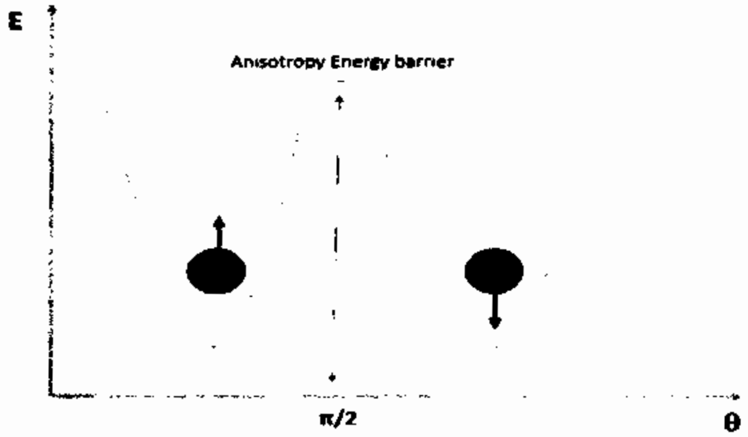

Figure 1.13: Uniaxial anisotropy energy barrier.

1.7 Magnetic Relaxation

The increase in thermal energy (K_BT) not only causes the magnetic dipole moments to flip across the easy axis but also applied magnetic field forces to (i) change the orientation of magnetic dipole moment and (ii) orientation of nanoparticle, known as Néel and Brown's magnetic relaxation process [19]. Néel's relaxation is the reversal of particle's net magnetic moment along easy axis orientation whereas Brown's relaxation is the physical rotation of the whole nanoparticle with its magnetization axis.

1.7.1 Néel Relaxation Model

Louis Néel was the first who proposed a theoretical model for the magnetic instability, therefore known as Néel relaxation model [20]. Due to the magnetic anisotropy of nanoparticle, there are two stable and anti-parallel orientations of net magnetic dipole moments. These orientations are separated by an energy barrier. When the thermal energy K_BT is comparable to the anisotropy energy barrier E_a, then net magnetic dipole moment can flip between these two stable and antiparallel orientations. The mean flipping time between these two stable orientations is known as Néel relaxation time (τ_{Neel}) proposed by Néel-Arrhenius law,

$$\tau_{Neel} = \tau_o e^{\left(\frac{E_a}{k_BT}\right)} \tag{1.31}$$

Where, $E_a = K_{eff}V$, so above equation takes the form

$$\tau_{Neel} = \tau_o e^{\left(\frac{K_{eff}V}{k_BT}\right)} \tag{1.32}$$

Where, τ_o is the atomic spin flip time which the characteristic of any material and lies in the range $10^{-13} - 10^{-9}\ s$. As τ_{Neel} is the exponential function of particle volume, so it can be from few seconds to years depending on the size of particle [21].

1.7.2 Brown's Relaxation Model

Brown's relaxation occur when the magnetic particles are dispersed in liquid such as ferro-fluid [22]. In this case, nanoparticle rotates physically as a whole with characteristic relaxation time (τ_{Brown}) is given by;

$$\tau_{Brown} = \frac{<V>\eta}{k_BT} \tag{1.33}$$

Where η is the viscosity of fluid and $< V >$ represents the average hydrodynamic volume of particle.

1.8 Superparamagnetism

At a finite temperature, the net magnetic dipole moment of smaller NPs (5-50 nm) become unstable and starts fluctuating, this phenomena occurs below T_c and is known as superparamagnetism. This state occurs when thermal energy dominates over the anisotropy energy barrier E_a [23] and the condition for superparamagnetism is given by;

$$\tau_{Neel} = \tau_o e^{\left(\frac{K_{eff}V}{k_BT}\right)} \tag{1.34}$$

$$\ln\left(\frac{\tau_{Neel}}{\tau_o}\right) = \frac{K_{eff}V}{k_BT} \tag{1.35}$$

For atomic spin flip time, $\tau_o = 1 \times 10^{-9}\, s$ and measurement time, $\tau_{Neel} = 100\, s$ for nanoparticle, we get

$$E_a = K_{eff}V = 25k_BT_B \tag{1.36}$$

Where, T_B is the temperature after which net magnetic dipole moment of nanoparticle become unstable and starts fluctuating, known as its blocking temperature.

1.9 Blocking Temperature

For a single-domain magnetic nanoparticle, the transition temperature between thermally stable and unstable state of net magnetic dipole moment is known as its blocking temperature (T_B) [24]. The net magnetic dipole moment of NPs remains in blocked state below T_B due to smaller thermal energy and dominated anisotropy energy barrier. However, above T_B, the thermal energy overcomes the anisotropy energy barrier and the net magnetic dipole moment starts fluctuating, known as superparamagnetic state. In superparamagnetic state, net magnetic moment of whole nanoparticle behave as paramagnetic with no magnetic interactions with other particle's net magnetic moment. Blocking temperature is a very important parameter which has a key role in fabricating new magnetic devices and depends on the size of nanoparticle (V) [25], measurement time (τ) [26] and inter-particle interactions [27]. After zero field cooling of sample, magnetic relaxation with increasing thermal energy is used to find the blocking temperature. Néel relaxation occurs if M-H loop is taken in superparamagnetic state because net magnetic moment starts aligning with the field. However, if M-H loop is taken in blocked state, then both Néel and Brown's relaxation are possible because if anisotropy energy barrier is sufficiently high and thermal energy is too low then nanoparticle can possibly physically rotate to align its net magnetic moment with the applied magnetic field.

1.10 Freezing Temperature

The surface spins in AFM NPs are not strongly coupled as core spins and show paramagnetic behavior even below the blocking temperature. In order to freeze these magnetic spins, much lower temperature (~5-25 K) is required known as freezing temperature of NPs. The smaller peak in ZFC at low temperature represent the freezing temperature of AFM NPs. The M-H loop taken below the freezing temperature shows huge coercivity due to strong coupling effect at low temperature.

1.11 Magnetic Structure of Nickel Oxide

Nickel oxide (NiO) is a 3d-transition metal oxide and also known as bunsenite after discovery by R. Bunsen in 1858. Bulk NiO belongs to *Fm3m* space group and has face centered cubic (fcc) rock-salt crystal structure with lattice constants a=b=c=0.4177 nm. In the fcc structure of NiO, Ni^{2+} ion occupy the octahedral site and each Ni ion is surrounded by 12 nearest neighbor Ni ions with 6 aligned in parallel spin and remaining 6 antiparallel. It is type-II AFM material with antiparallel alignment of magnetic spins adjacent to (111) plane. It has T_N=523 K [28] which is highest reported among other AFM monoxides. It has green color in bulk and black in NPs. There are two types of magnetic interactions present in the NiO AFM system, (i) the direct exchange interaction between Ni atoms and, (ii) the super-exchange interactions between Ni atoms via oxygen atom. Figure 1.14 shows the crystal structure of NiO with AFM alignment of spins along (111) plane.

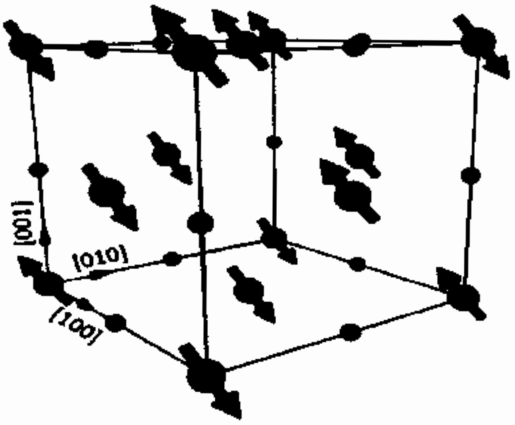

Figure 1.14: Crystal structure of NiO with AFM spin alignment [29].

1.12 Optical Properties

The optical properties of the material signifies its interaction with light and leads to a variety of interesting phenomenon such as reflection, polarization, absorption, photoluminescence, transmittance, diffraction, dispersion, scattering and photocatalysis, etc. The absorbance of light in a given material at different wavelengths is expected to depend on several factors such as impurities, surface roughness, oxygen deficiency and energy band gap etc [30]. The wide band gap transition metal oxide semiconductors such as NiO is widely used as photocatalyst. In metal oxides, oxygen vacancies play an important role in controlling the optical properties and therefore have wide applications in optoelectronic devices.

1.12.1 Energy Band Gap

The energy band gap (E_g) of material define its optical response the incident light. The E_g can be altered by making alloy or adding some impurity (doping) that may change the structural or elemental composition.

Based on electronic band structure, E_g can be either be direct or indirect as demonstrated in Fig 1.15. Those materials have direct E_g in which lowest energy state in conduction band and highest energy state in the valance band have same momentum.

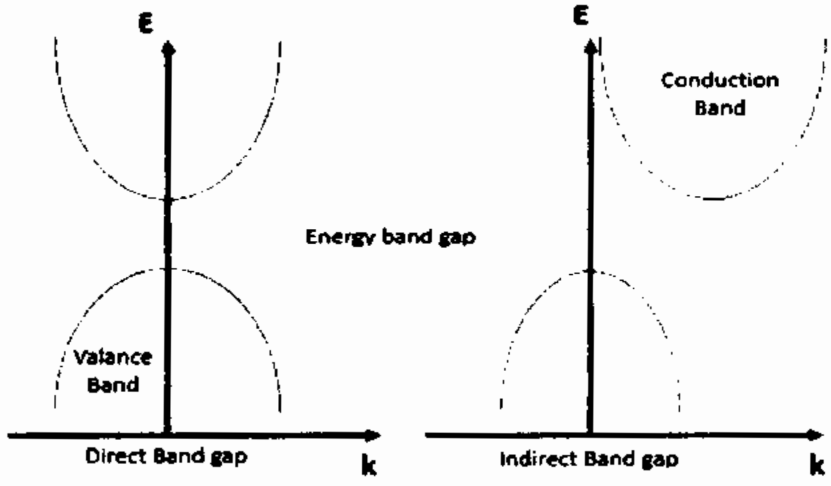

Figure 1.15: Direct and indirect band gap semiconductors.

In a material with direct E_g, valance electrons can be excited to the conduction band by photons if the photons energy is equal or greater than the E_g. However, in indirect band gap material, photon and phonon (for momentum conservation) are both required for such a transition from valance band to the conduction band. Therefore, the absorption and emission properties of direct band gap material are much better than indirect band gap material. The direct band gap materials tend to be better for light emitting diodes, photovoltaics and laser diode, etc. The $E_g$for a bulk material is fixed due to continuous energy states, however it changes when its dimensions are confined down to nanoscale known as quantum confinement effect.

1.12.2 Quantum Confinement Effect at Nanoscale

At nanoscale, optical and electronic properties deviate from bulk, known as quantum confinement effect. When the confining dimensions of a particle are large, then it has continuous energy states and its E_g remain same as original. However, when the dimensions are reduced, typically to nanoscale then the energy states become discrete and as result E_g become size dependent as shown in Figure 1.16.

The blue shift was observed upon the decrease in size of NPs, which indicate that energy band gap increases with decrease in size. The relation between energy band gap and size of particles is explained by the Brus equation [31],

$$E_{g\,(nano)} = E_{g(bulk)} + \frac{\hbar^2}{8R^2}\left(\frac{1}{m_e^*} + \frac{1}{m_h^*}\right) - \frac{1.786e^2}{4\pi\epsilon_o\varepsilon_r R} \qquad (1.37)$$

Where R being the radius of nanoparticle. The experimental method for finding the optical energy band gap is through Tauc's relation [32].

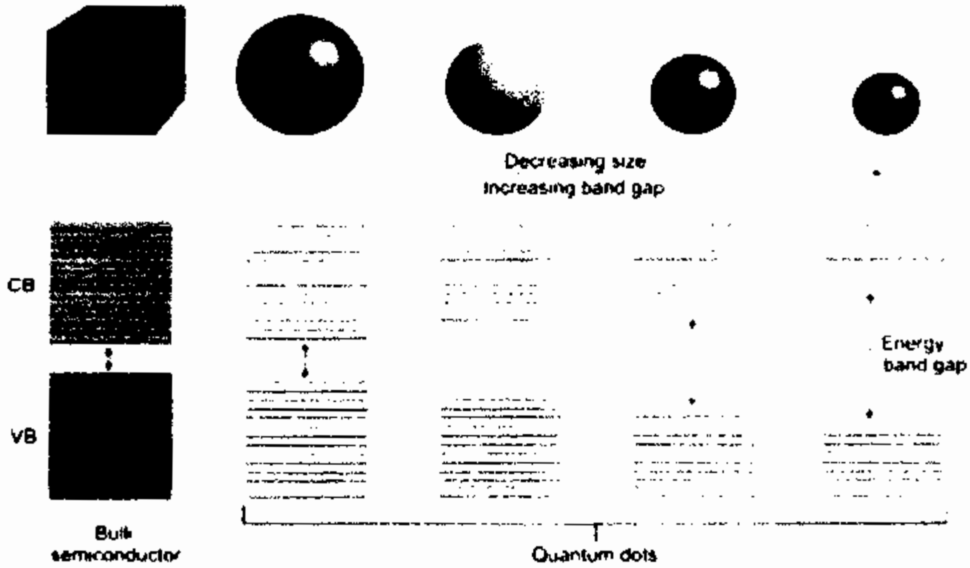

Figure 1.16: Quantum confinement effect [33].

1.12.3 Moss-Burstein Effect

Moss-Burstein effect explains the apparent increase in the E_g of a material. The absorption edge shifts to higher energy states when some energy states get populated near the conduction band and is usually observed for degenerate electron distribution. It happens when the electron carrier concentration increases from the conduction band edge density of sates. The Fermi level usually lies between the conduction and valance band for nominal doping. However, when degenerate level of doping percentage is increased, fermi level moves to a high energy in conduction band due to population of high energy electron states in conduction band.

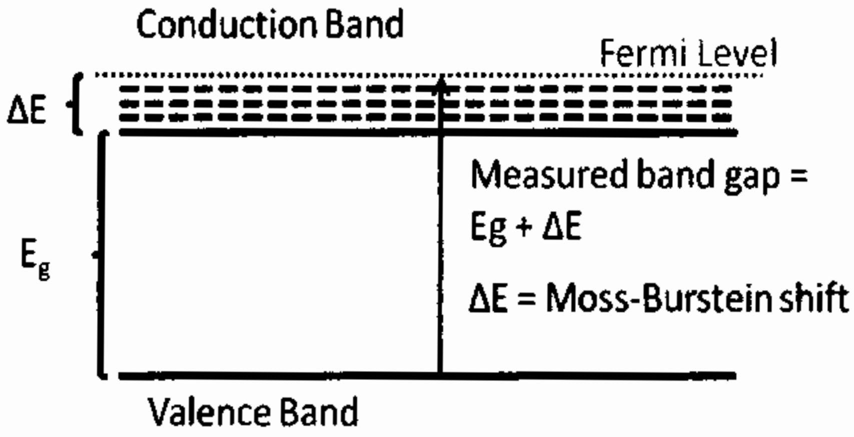

Figure 1.17: **Moss-Burstein effect [34].**

For a degenerate semiconductor, valance electrons are excited above the Fermi level in conduction band only if all the states are occupied below Fermi level in accordance with Pauli's exclusion principle. Thus, apparent enhancement in optical energy band gap is observed which is equal to the addition of actual band gap and Moss-Burstein shift as shown in Figure 1.17. The negative Moss-Burstein effect is also possible due to the doping induced structural defects.

1.12.4 Tauc' Relation

Tauc's relation is widely used to estimate the optical energy band gap of any material as given below [32],

$$(\alpha h\nu)^n = B(h\nu - E_g) \tag{1.38}$$

Where, $h\nu$ is the photon energy, α is absorbance coefficient, B is a constant, $n = 2$ for direct band gap and $n = ½$ for indirect band gap [35]. The extrapolation of $(\alpha h\nu)^n - h\nu$ curve to zero gives an estimate for optical E_g. The absorbance coefficient (α) can be found by Kubelka-Munk function F(R) [36] by taking diffuse reflectance spectra of given material,

$$F(R) = \frac{(1-R)^2}{2R} \tag{1.39}$$

The absorbance coefficient (α) can also be found by taking transmittance data from UV-Vis spectrophotometer [37],

$$\alpha = \frac{1}{d}\ln(1/T) \tag{1.40}$$

Where, d is the thickness of cuvett and T is the transittance.

1.12.5 Photocatalysis

Pollution is a worldwide problem and needs to be addressed efficiently to main the eco-friendly nature of earth. The various pollutants in the environment and especially in water are severe threat to the human life due to poor sanitation, untreated hazard disposal, discharge of hazard material into water by chemical industry and industrial/textile dyes. Organic dyes are the leading group of pollutants with highly suspended solids, acidity, heat, color and chemical oxygen demand etc. Therefore, a water treatment technique is required which is flexible, efficient, good recycling capability, cost-effective and eco-friendly. Photo catalysis is considered as one of the most efficient technique for water treatment due to oxidation of organic compounds and harmless by products such as H_2O and CO_2 are obtained. In photocatalysis, light and photocatalyst simultaneously speed up the chemical reaction and it can be classified into two categories;

1.12.5.1 Homogenous Process

In this process, higher oxidation state generate hydroxyl radicals (under photon and thermal condition) which react with organic matter to destruct the toxic matter. In this process, both photocatalyst and reactant remain in same phase.

1.12.5.2 Heterogeneous Process

This method is used to degrade a number of organic pollutants present in water. It has several advantages such as no waste disposal problem, full mineralization, and low cost, etc. The semiconductors such as TiO_2, ZnO, CeO_2, SnO_2, etc act as heterogeneous photo catalysts due to their favorable electronic structure.

Semiconductor photo-catalysts are emerging as promising candidates that are photoactive, utilize most of visible light, biologically and chemically inert, photo stable, cost effective and non-toxic. The fundamental steps of phocatalysis in semiconductor are; when light (photons) falls on the surface of a semiconducting material, the electrons in the valance band jumps to the conduction band, if photons have sufficient energy. The shifted electrons leave behind holes in the valance band which oxidize the donor molecules and generate hydroxyl radicals. These hydroxyl radicals are known for their strong oxidizing power and play vital role in pollutants degradation. However, excited electrons present in conduction band react with the dissolved oxygen and generate superoxide anions. Both the electrons and holes undergo oxidation and reduction process simultaneously and generate by-products. Figure 1.18 depicts the schematic demonstration of photocatalytic mechanism.

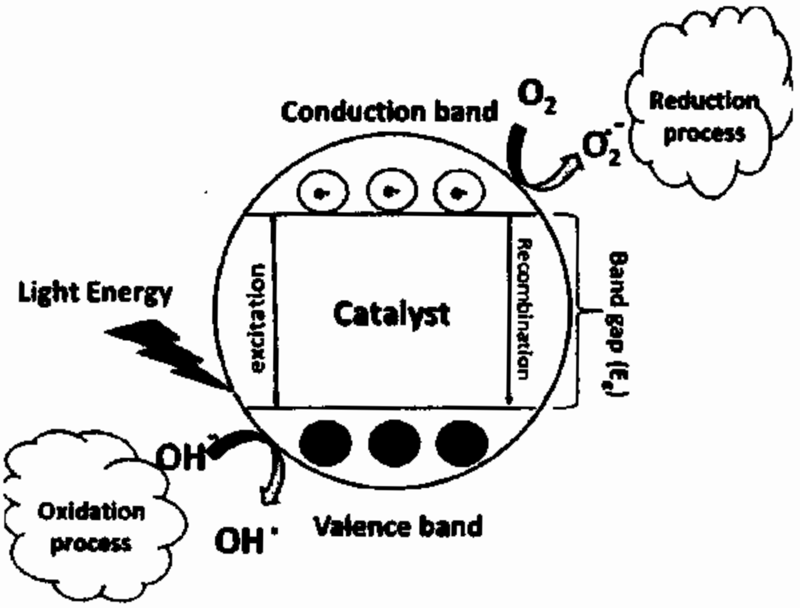

Figure 1.18: Schematic illustration of photocatalytic mechanism [38].

1.12.5.3 Oxidation Process

The holes in the valance band oxidize the water molecules near the surface of water and generate hydroxyl radicals. These hydroxyl radicals have strong oxidative decomposing power and therefore react with the organic matter to degrade.

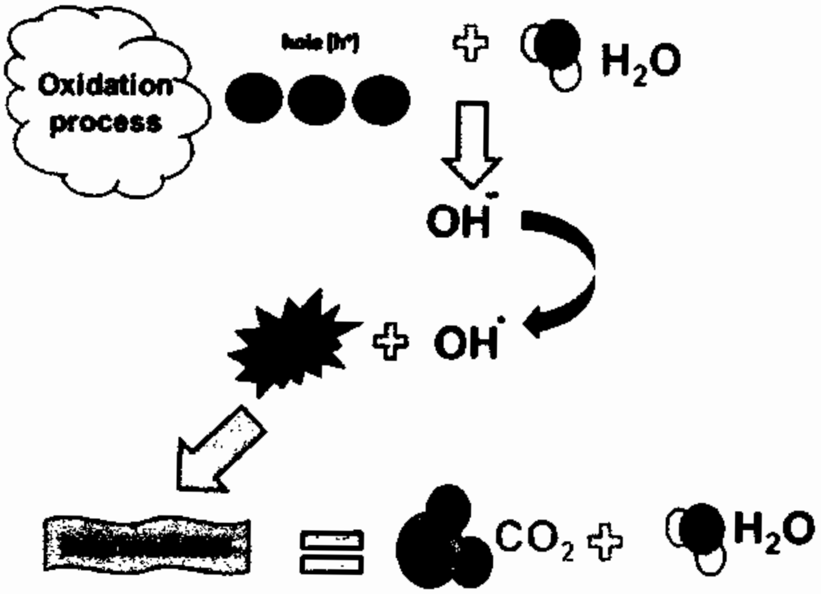

Figure 1.19: Schematic illustration of oxidation process [38].

The intermediate radicals in the organic compound undergo radical chain reaction. The organic matter converts into carbon dioxide and water which are harmless byproducts. Furthermore, the positive holes directly interact with the organic compound and yield oxidative decomposition. The oxidation process is shown in Figure. 1.19.

1.12.5.4 Reduction Process

The dissolved oxygen species interact with the electrons in the conduction band and superoxide anions are formed which get attach to intermediate products in the oxidation process and produce hydrogen peroxide and water. Thus, reduction process is much favorable in organic matter than in water. The reduction process is illustrated in Figure. 1.20.

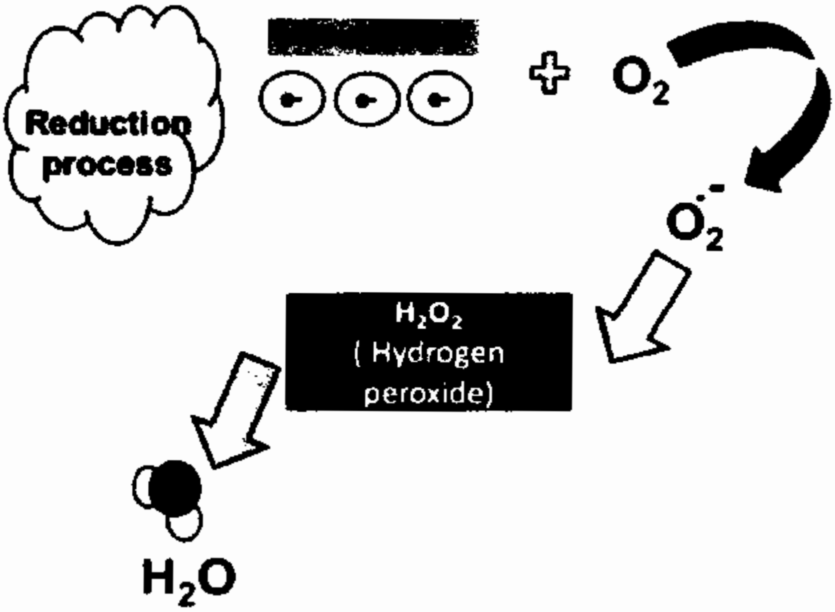

Figure 1.20: Schematic illustration of reduction process [38].

1.12.6 Parameters Affecting Photocatalysis

The rate of photocatalytic reaction depends on the synthesis technique and many other physical parameters such as shape and size of NPs, structure, surface area of catalyst, pH of solution, reaction temperature, light intensity, concentration of waste water, amount of catalyst, etc. The effect of change in some parameters is given below in detail;

1.12.6.1 Crystal Structure

The crystal structure of catalyst acts as potential role in attaining the much better photocatalytic activity of crystalline material. For example, three different phases of TiO_2, such as anatase, rutile and brookite has different photocatalytic activity. Anatase has the superior photocatalytic activity than rutile and brookite due to its conduction band position, thermal stability, adsorption and much higher degree of hydroxylation.

1.12.6.2 Size of Photocatalyst

The photocatalytic activity of some materials at nanoscale is much superior as compared to their counter bulk part. At nanoscale, large number of atoms appear on the surface which is important for increased reaction rate. The large number of atoms at the surface attributes to the large number of active sites and also as a result interfacial charge carrier transfer rate increases which are responsible for higher photocatalytic activity. The photocatalytic redox reaction take place at the surface of photocatalyst, therefore the materials with large surface to volume ratio (small size) are much better photocatalysts.

1.12.6.3 Reaction Temperature

The reaction temperature also influence/control the rate of photocatalysis. If the temperature is high, the electron-hole recombination rate is higher which is attributed to lower photocatalytic activity. Heat is not essential for photocatalytic process due to photonic activation and the process can run even at room temperature. The most favorable temperature range in photocatalytic reaction is dependent on the excitation energy.

1.12.6.4 Effect of pH value

The pH value of the solution is important for controlling the rate of photocatalytic reaction due to impact on surface charge properties of the catalyst. The pH value affects the electrostatic interactions between charge particles and contaminants which is basically defined as the rate of reaction.

1.12.6.5 Effect of Light Intensity

In photocatalysis, the catalyst is driven by the light, therefore intensity of light is an important parameter in controlling the photocatalytic reaction. The more light absorbed by the catalyst, the fast reaction will be. However, there is a critical value for the light intensity above which electron-hole recombination rate starts increasing and thereby reduces the rate of photocatalytic reaction. The quantum yield is defined as the ratio of rate of photocatalytic reaction to the rate of light absorption. The rate of reaction is also controlled by varying the wavelength of light which actually corresponds to the photon energy.

1.12.6.6 Amount of Catalyst

The photocatalytic reaction also depends upon the amount of catalyst. It is quite obvious that the large quantity of catalyst provides large number of active sites which in turn produces large number of hydroxyl radicals and certainly reaction rate get increased. However, there is an optimum value for the amount of photocatalyst and beyond that value, degradation rate become unfavorable due to decrease in light penetration depth and increase in light scattering.

1.12.6.7 Concentration of Pollutants in Wastewater

The pollutant type and its concentration has great impact on the photocatalytic degradation rate. The same catalyst under same operating conditions have different response for different pollutants concentration. Therefore, different irradiation time is required for the complete mineralization.

1.13 Effect of Coating in Nanoparticles

In order to avoid the agglomeration of magnetic nanoparticles (NPs), the materials with non-magnetic nature can be embedded between the NPs. The choice of those materials is very important in order to obtain the desired outcome. The materials with less probability of interaction and ability to surround the host material are more favorable. For achieving this purpose, different types of organic surfactants and polymers are being used which are biocompatible and thermally stable. The silicon dioxide (SiO_2) which is obtained from TEOS (tetraethyl orthosilicate) is also being widely used for the coating of metal oxide NPs. It is a non-magnetic, amorphous material having ability to surround the material without much interaction with the host material. The large number of nucleation sites in silica restrict the crystallite size and different sized NPs can be obtained by varying the silica concentration. It also reduces the agglomeration of magnetic NPs and its amorphous nature makes it suitable candidate for composite formation due to less doping probability. Being non-magnetic in nature, when SiO_2 surrounds magnetic NPs, the dipolar inter-particle interactions decreases and induces super-paramagnetism. It has remarkable properties such as thermal stability, non-toxicity, low cost, high specific surface area and biocompatibility. For NiO NPs, the use of SiO_2 coating can decrease its average crystallite size and potentially can generate oxygen vacancies which are important for optical applications. Also the use of SiO_2 coating on NiO increases the surface disorder, and ultimately generate the uncompensated spins at the surface and in the AFM core of NiO NPs which is important for magnetic applications.

1.14 Effect of Doping in Nanoparticles

Doping plays a key role not only in stabilizing the crystal structure of any material but also attaining improved physical properties. The structural, magnetic, optical and such other physical properties can be substantially changed by the choice and level of doping. It is also common to observe that the doping technique increases the structural, magnetic and thermal stability of host material. From structural point of view, slight variation in lattice parameters is possible when a doped ion with different lattice constant replaces the host ion. From optical point of view, dopant may introduce some new intermediate energy levels that can possibly alter the energy band structure and also can generate energy traps which could possibly decrease the electron-hole recombination rate which is important for photocatalysis. From magnetic point of view, when dopant ion replaces the host ion, it introduces new magnetic interaction and changes the net magnetic moment. The dopants in NiO can change its magnetization by adopting the parallel/antiparallel coupling to the Ni atoms or/and introducing frustrating into the magnetic structure. NiO is an AFM material below 523 K, however room-temperature ferromagnetism is reported for NiO NPs doped with transition metals, e.g. Fe^{2+} and Mn^{2+} ions [39, 40]. The use of single or double dopants in NiO can possibly increase the magnetic homogeneity, thermal stability and strengthen the intra-atomic magnetic interactions which are important for various magnetic applications.

1.15 Motivation

NiO is a promising AFM material with unusual magnetic properties, which have been reported in many studies [41-55]. For AFM material at nanoscale, a large number of spins on the surface as well as in the core get uncompensated. This uncompensation leads to increase the net magnetization of AFM nanomaterial. However, upon further decreasing the size of NPs, uncompensated spins in the core also tends to increase in number which give further contribution to the net magnetization. Therefore, synthesizing small size AFM NiO NPs were of primary interest for studying magnetic properties. The use of different concentration of SiO_2 may provide different number of nucleation sites and can result into achieving small sized NiO NPs. For a critically small sized NPs, the disordered surface of

AFM NiO may behave as FM shell and AFM NiO NPs can become bi-magnetic core/shell NPs. Cooper *et al.* [56] reported the bi-magnetic structure of NiO NPs by neutron diffraction technique. The bi-magnetic core-shell structure is considered as potential material for application in spintronic [57] and particularly important in tuning the magnetic parameters such as coercivity, blocking temperature, etc. Furthermore, fabrication of bi-magnetic NPs can enhance the effective exchange coupling which is important for cooperative magnetic switching. The blocking temperature is usually observed at low temperature for AFM NPs and after that magnetic moments become thermally unstable. To overcome this problem, bi-magnetic structure can be useful in controlling the magnetic properties of AFM NPs. The magnetic properties of NiO NPs can be also controlled by doping process [58-61]. The dopant can couple parallel/antiparallel to Ni^{2+} ions depending on the type of interaction or it may induce the frustration in the magnetic structure which may enhance the net magnetization. The room temperature ferromagnetism is reported in AFM NiO NPs by use of single dopants [39, 40]. However, co-doping of suitable metal ions is also becoming promising strategy to control the physical properties of NPs. Paul [62] reported that the clustering tendency of Mn ions (when used as dopant) can be reduced by doping Fe ions in Ge matrix. Therefore, the co-doping of Fe and Mn ions into NiO could be interesting due to very small difference in ionic radii, Ni^{2+} (0.69 A^o) Mn^{2+} (0.67 A^o), Fe^{2+} (0.74 A^o) or Fe^{3+} (0.64 A^o) [63, 64] and can possibly have smaller impact on the crystal structure of NiO

CHAPTER NO. 2

Literature Review

Here in this section, we will discuss some important research work related to optical and magnetic properties of undoped, single doped, co-doped, and coated NiO nanoparticles (NPs) carried out by researchers from all over the world.

Nadeem *et al.* [65] synthesized Ni/NiO NPs at air annealing temperatures (400-800 °C) via sol-gel method. They observed decrease in Ni content with increasing annealing temperature. The Ni phase (~ 6%) was still present at maximum annealing temperature of 800 °C. For the complete removal of Ni phase, temperature higher than 800 °C was required which was expected to result into larger <D> and suppression of magnetization as being pure AFM NiO. The magnetic measurements such as M-H loops showed decrease in saturation magnetization with increasing annealing temperature due to decrease of Ni phase content and large <D>.

Shahid *et al.* [66] utilized the composite hydroxide mediated approach to synthesize the NiO nanocrystals. The sodium hydroxide and potassium hydroxide were used as reaction media. The melting temperature of both hydroxides is ~400 °C, however it lowers to ~200 °C when mixed in a specific ratio. Different samples of NiO have been prepared at different temperatures ranging from 180-250 °C and observed that the sample annealed at 220 °C has better morphology than other samples. Structural characterization such as XRD, FTIR and SEM confirmed the formation of single phase NiO nanocrystals with <D> lies in the range 23-36 nm. The E_g of all these samples was estimated and reported to be in the range of 4.0-4.8 eV which is relatively larger in comparison to reported in other studies. The main aim of the whole study was to introduce a simple, cost effective and low temperature technique for the synthesis of NiO NPs without presence of Ni phase.

Tadic *et al.* [8] reported the sol-gel fabrication of crystalline NiO NPs dispersed in amorphous silica matrix. XRD confirmed the fabrication of pure NiO NPs. The <D> was found to be 5 nm and spherical shape of these NPs was observed by TEM. They observed two maximum in ZFC curve at 5 and 56 K which they attributed to blocking temperature and Néel temperature, respectively. The low value of Néel temperature than bulk (523 K) is due to weaken magnetic coupling. The weak inter-particle interactions which may be present by the presence of silica were confirmed by fitting the Vogel-Fulcher law to frequency dependent blocking temperature. They fit the Curie-Weiss law to experimental data above 100 K and obtained Curie constant, C=1.026 emu K/mol. Oe and Curie-Weiss temperature θ=24°. The positive and low value of C and θ indicated the FM Ni atoms interaction at the surface and low value indicate the weak AFM interactions which are main reason for the reduction of Néel temperature. Finally, magnetic moment was calculated to 2.87 μ_B per NiO unit.

Nikolic *et al.* [67] reported the magnetic properties of NiO NPs dispersed in silica matrix at different annealing temperatures. The samples were prepared at different annealing temperature of 500, 800, 950, 1100 °C by sol-gel method. For sample annealed at 800 °C, a significant broadness of zero filed cooled magnetization curve, higher irreversibility temperature, decreased magnetization, increased coercivity and weak inter-particle interactions has been observed in comparison to other samples which is attributed to the agglomeration of NPs due to the removal of thin silica wall between them. For the sample with higher annealing temperature, i.e 1100 °C, the size of NiO NPs get further increased which result into strong inter-particle interactions confirmed by magnetic measurements.

Kodama *et al.* [68] reported the anomalous magnetic response of AFM NiO NPs. They observed large magnetic moment and coercivity and loop shift up to 10 kOe. All these finding were difficult to explain on the basis of two-sublattice model which is widely accepted for AFM ordering of bulk NiO. For explaining the spin structure in NiO NPs, they presented 4-, 6-, and 8-sublattice model with a new finite size-effect and explained the change in magnetic ordering throughout the nanoparticle due to lesser coordination of surface spins.

Montes *et al.* [69] observed the size dependent reduction of Néel temperature of NiO by neutron diffraction technique. For this purpose, they synthesized four samples of NiO at different heating temperature for controlling the crystallite size. The diameter of the synthesized NiO NPs heated at 573, 613, 643 and 673 K was found to be 4, 6, 7 and 9 nm, respectively. They reported the size dependence of Néel temperature as phase transition in low dimension system as thick layer of canted spins is supposed to be exist on the surface of nanoparticle. XFAS gave insight to the fact that how the breakage of local magnetic symmetry affect the environment of surface atoms. It has been observed that the decrease of Néel temperature with decrease in size is due to the bond relaxation, under-coordination and static disorder which are the key factors for maintaining the AFM order.

Pradeep *et al.* [70] prepared 1, 5 and 10 % Fe doped NiO NPs by hydrothermal method. There was no other secondary phase observed even for maximum (10%) doping percentage. They observed from the XPS that Fe is in trivalent state (Fe^{3+}) and replaced the Ni^{2+} ion at the octahedral site of FCC structure of NiO. However, EPS characterization revealed the formation of FM clusters at 5 and 10 % of Fe doping concentration. The M-H loop for pure NiO taken at 5 K showed strong FM signal due to the blocked state of surface and core uncompensated spins. The ZFC/FC curves showed increasing blocking temperature with increasing Fe doping concentration due to strong FM coupling of Fe and Ni atoms.

Layek *et al.* [40] synthesized the 0, 2, 4 and 6 % Mn doped NiO NPs by hydrothermal method and reported the RTFM in AFM NiO NPs for 2% Mn doping concentration. It has been observed that the 2% Mn doped sample showed maximum magnetization which starts decreasing by increasing the Mn doping concentration. At low concentration of Mn, Ni and Mn atoms coupled ferromagnetically and results into higher net magnetization. As Mn has paramagnetic nature, therefore at higher concentration it increase the magnetic inhomogeneity in the system and thus magnetization starts decreasing. They also reported the FM Curie temperature of 653 K for 2% Mn doped sample by temperature dependent magnetic measurement.

Sankar *et al.* [71] synthesized Mn doped NiO NPs with Mn doping concentration of 1, 2, 3 and 4% by sol-gel synthesis technique. The formation of NiO phase is confirmed by XRD analysis and spherical morphology of synthesized NPs is confirmed by SEM and TEM. They observed decrease in crystallite size from 35 to 30 nm when Mn doping concentration was increased from 1 to 4 %. The optical study revealed that the energy band gap of 4% Mn doped sample is greater than undoped sample which is due to the quantum size effect. They tested the photocatalytic activity of 0 and 4 % Mn doped NiO samples and observed the photo degradation MB. It has been observed that the photo catalytic activity of 4% Mn doped sample was much better than the undoped NiO sample. The much better photocatalytic results were attributed to the generation of more activation sites by Mn doping.

Srikesh *et al.* [72] synthesized Mn and Co co-doped NiO nanostructures by chemical synthesis route for supercapacitor electrode application. The FCC structure of NiO was confirmed by XRD whereas morphology was identified by SEM. It has been observed that the NPs are of spherical shape with average diameter lies in the range 14-28 nm. The EDS analysis confirmed the presence of appropriate amount of elements in the sample. The electrochemical performance of samples was investigated for all samples and observed that the doping level of Mn and Co has significant impact on the capacitive behavior of NiO nanostructured material. The sample with equal Mn and Co doping showed maximum specific capacitance. Finally, they compared the performance of equal doping level sample with blank graphite sheet which has excellent electrochemical properties.

Manna *et al.* [73] investigated the magnetic properties of Li and Fe co-doped NiO NPs. They synthesized the samples with fixed 2% Fe doping concentration and varying the Li ions doping concentration as 0, 3 and 5 %. XRD confirmed no other impurity phase whereas SEM indicate the granular nature of prepared samples. They reported the paramagnetic to FM transition around 242 K and large coercivity in Li doped samples was attributed to the disorder generated by Li ions in NiO matrix. The hysteresis appear at room temperature (RT) which indicate that the Tc lie above RT for Fe doped samples. However, doping of Li along with Fe doped NiO modified the transition temperature. The doping of Li and Fe in AFM NiO also induces FM phase due to cationic disorder and lead to the spin glass behavior in the NiO system.

Madhu *et al.* [74] synthesized NiO nanostructured material by chemical route with <D> in the range 32-45 nm. The Ni^{2+} and O^{2-} vacancies were observed by the DC conductivity measurements and antioxidant activity of samples. It is observed that the oxygen vacancies get reduced with increasing annealing temperature and magnetization get suppressed. They also confirmed the core-shell structure of NiO NPs with AFM core and spin glass (SG) like shell. It is observed that the total uncompensated moment and net magnetic moment is directly proportional to the O^{2-} vacancy concentration and the FM nature increases with decrease in crystallite size. They also presented a model to explain the FM interactions in the presence of O^{2-} and Ni^{2+} vacancies.

Aragon *et al.* [75] synthesized NiO NPs by polymer precursor method. XRD technique was employed for the phase analysis and the crystallite size was observed to be 22 nm in accordance with the transmission electron microscopy. The M-H loop at RT showed paramagnetic behavior whereas it showed FM like behavior at 5 K. Two peaks were observed in the ZFC curve, the high temperature peak is assigned to thermal relaxation of uncompensated spins in the core of NPs and low temperature peak is attributed to the thermal relaxation of uncompensated spins on the surface of NP.

Duan *et al.* [76] synthesized NiO NPs with size of 3.5, 4.8, 5.6, 10.3 and 12.4 nm for different annealing temperatures. They observed the size effect on vibration modes, exciton ground state energy, magnetic and optical properties. They reported the increase in E_g with decrease in particle size in according with quantum confinement effect. The red shift in the longitudinal optical (LO) mode and increase in its intensity has been observed with decrease in size of NPs which is indication of defect generation. The two magnon band was not observed in any sample which shows that the NPs are not in AFM state. The small size of NPs weaken the exchange interactions and its Néel temperature is below room temperature, therefore it may be concluded that the NPs are in paramagnetic state. It is observed that the blocking temperature and bifurcation temperature decreases with decrease in particle size. However, net magnetization and coercivity increased with the decrease in crystallite size which is characteristic of AFM NPs.

Limori *et al.* [77] synthesized NiO NPs with mean diameter of 5 nm and decomposed the magnetization curve to the sum of AFM component and superparamagnetic components observed from the M-H loop. They observed two maxima at 18 and 140 K, and ascribed it to the magnetization induced from the uncompensated spins of surface and core, respectively. The stated that the magnetization of the same size AFM system could be different due to the presence of inhomogeneity and different magnetic orders.

Popkov *et al.* [78] fabricated NiO NPs with size ranges from 4.5 to 23 nm and observed their magnetic behavior. They observed the increased FM contribution of AFM NiO NPs with the decreasing size. It has been observed that the induced uncompensated exchanged coupled spins increases with decrease in size of NPs. The formation of FM subsystem in the small sized NiO NPs was ascribed to the generation of defects at the surface and in the core of the system. They also observed that the saturation magnetization of such FM subsystem of AFM NPs is almost comparable to the saturation magnetization value for the FiM oxide NPs of same size.

CHAPTER NO. 3

Synthesis and Characterization Techniques of Nanoparticles

The synthesis techniques being employed for the synthesis of the nanoparticles (NPs) have significant influence on its physical properties. Basically, there are two well-known synthesis approaches used for the synthesis of NPs, top-down and bottom-up approach [79]. Both these synthesis techniques have their own advantages and limitations. The brief introduction of these approaches is given below:

3.1 Top Down Approach

In this synthesis approach, NPs are fabricated by sizing down the bulk material to nano-scale. The mechanical ball milling, sputtering, lithography, plasma etching, electro-spinning etc. are the few of examples of top down approach. For unique and tuned physical properties of NPs, uniform size distribution is very important, This technique has inability for achieving uniform size distribution and considered as its main drawback.

3.2 Bottom Up Approach

In this synthesis approach, atoms or molecules are assembled by physical forces to form nanostructures. The sol-gel, sonochemical, hydrothermal, electrodeposition, chemical vapor deposition, molecular beam epitaxy, arc discharge etc. are few of the examples of bottom up approach. The precise shape, structure, chemical composition and relatively uniform size distribution are few of the advantages of this synthesis approach. Figure 3.1 shows the schematic diagram of Top-down and Bottom-up synthesis approaches.

In this thesis, we have used bottom up approach such as sol-gel (SG) and composite hydroxide method (CHM) for the synthesis of uncoated, SiO_2 coated, single doped and co-doped NiO NPs. Sol-gel method is used for the fabrication of uncoated and SiO_2 coated NiO NPs whereas CHM method is used for the pure, single doped and co-doped NiO NPs. In the following section, both these synthesis methods are discussed in detail.

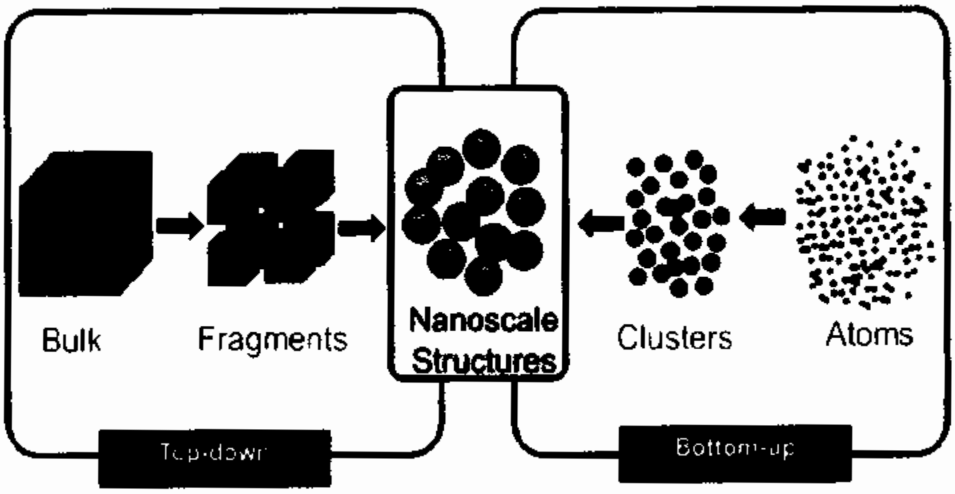

Figure 3.1: Top-down and Bottom-up approach [80].

3.2.1 Sol-gel Method

To fabricate the metal oxide NPs. The word ''sol'' is used for the homogenous mixing of colloidal particles where ''gel'' is a 3D continuous chain network in a liquid. This method undergoes in few steps (hydrolysis, condensation and drying) to deliver the metal oxide NPs [81]. Firstly, the precursor of metal oxide undergoes hydrolysis to produce metal hydroxide solution and then condensation that leads to form the 3D gel. Finally, this gel is subjected to the drying process to obtain the resultant product.

For the preparation of uncoated NiO NPs, nickel-citrate complex precursor was utilized [65]. First, Ni(II) solution was prepared by dissolving 5g (mmol) nickel nitrate hexahydrate [$Ni(NO_3)_2.6H_2O$] in 60 ml of deionized water. Then, the nickel-citrate synthesis was started by the dropwise addition of 40 ml solution of 3.3 g (mmol) of citric acid monohydrate [$C_6H_8O_7.H_2O$], using 1:1 molar ratio of nickel-to-citric acid. Afterwards, pH=5 was adjusted with the help of ammonia. The resulting solution was stirred at 70°C for 2 h to allow the Ni-chelate formation. The resultant material was then calcined at 900°C for 4 h in air to get NiO NPs. For SiO_2 coated NiO NPs, TEOS was added dropwise in the main solution during the synthesis process and all the other parameters kept constant. The different concentration of TEOS such as 0, 30, 50, 60, and 70 at.% was used for preparation of SiO_2 coated NiO NPs.

The citric acid acts as a polydentate ligand, which forms a number of complexes with Ni(II) in acidic as well as basic media. At different pH values it forms different anions, as is evident from its dissociation constants: $pK_1 = 3.08$, $pK_2 = 4.39$, $pK_3 = 5.49$ and $pK_4 = 11.6$. In alkaline solutions containing Ni(II) ions not only the three —COOH groups dissociate but also the —OH group gets dissociated. The coordination of these three $-COO^-$ groups with Ni(II) substantially lowers the pK value of citrate —OH group. When Ni(II) and citric acid are used in 1:1 molar ratio, the ionization of —OH group occurs at pH 8.7. The pH plays a crucial role during Ni(II)-citrate complex formation. When the solution is too alkaline, there are two competing reactions which give insoluble $Ni(OH)_2$ and polynuclear Ni(II)-citrate complex. The same competing reactions also occur when the concentration of Ni(II) is higher than citric acid. The residual Ni(II) will be precipitated as $Ni(OH)_2$. Actually, $Ni(OH)_2$ start to precipitate at pH 7.7. Therefore, to avoid the formation of insoluble $Ni(OH)_2$, optimum pH 5 was maintained with ammonia. At pH 2 to 7 citric acid exists as: H_2Citr^-, $HCitr^{2-}$, and $Citr^{3-}$.

$$Ni(II) + H_2Citr^- \equiv NiH_2Citr^+ \tag{3.1}$$

$$Ni(II) + HCitr^{2-} \equiv NiHCitr \tag{3.2}$$

$$Ni(II) + Citr^{3-} \equiv NiCitr^- \tag{3.3}$$

But at lower pH dissociation of three —COOH groups and —OH group of citric acid decreases, thus decreasing the complex formation, whereas at higher pH dissociation of carboxylate and hydroxyl groups increases complex formation. Therefore, optimum pH 5 was selected for complex formation to better control the NPs size. If the ratio of Ni(II) is lesser than citric acid, then, even at pH 5, Ni(II) tends to form polynuclear insoluble complexes, which give higher sized NPs. Hence, equimolar ratios of Ni(II) and citric acid were used to form NiO NPs from complexes.

3.2.2 Composite Hydroxide Mediated Approach

It is one of the simple and unique technique to synthesize the metal oxide NPs [82]. This technique is based on the chemical reactions of hydroxide melts ~200°C in the absence of capping agent and organic dispersants. The individual KOH and NaOH melt at 404 and 323°C, respectively, however their mixed hydroxide in a ratio of KOH:NaOH = 48.5 : 51.5 melts at 165°C. These mixed hydroxide play the role of a reaction medium and the reaction of metal oxide. The dissolution of reactants in hydroxide melt is based on the fact that H_2O and O^{2-} ions formed by the dissociation of hydroxide as:

$$2OH^- \leftrightarrow H_2O + O^{2-} \tag{3.4}$$

The solubility in melts can be controlled by the variation of H_2O and/or O^{2-} ions content. The water content in the melt is ~8.7% when NaOH and KOH are in eutectic mixture. The acidity of the mixture increases by the presence of that water content which considerably increases the solubility of metal oxide and results in the isotropic growth of nanocrystals. This water content present in the melt play a key role in controlling the particle size during synthesis process. The synthesis of pure NiO NPs can be summarized by the following reactions:

$$Ni(NO_3)_2.6H_2O + KOH + NaOH \rightarrow Ni(OH)_2 + +KNO_3 + NaNO_3 + 6H_2O \tag{3.5}$$

$$Ni(OH)_2 \rightarrow NiO + H_2O \tag{3.6}$$

For the synthesis of NiO NPs, NaOH-KOH in a ratio of 51.5 : 48.5 were taken in a Teflon beaker and desired amount of nickel nitrate hexahydrate was added into it. After thorough mixing, the beaker was placed in an oven at 200°C for 24 h. The formed NPs were washed 2-3 times with distilled water to remove the impurities. For the single or co-doping, relevant precursors were added with the nickel nitrate in the initial step and rest of the conditions were kept same.,'

3.3 Characterization Techniques

For the analysis of synthesized samples, different characterization tools/techniques were engaged to obtain the structural, morphological, optical and magnetic characteristics of the synthesized samples. These characterization techniques are discussed briefly in the next section.

3.3.1 X-ray Diffraction (XRD)

To obtain the structural information such as phase identification of the synthesized samples, XRD is the most ,widely used technique. The average crystallite size, lattice parameters, strain in the unit cell, etc. can also be found using this technique.

3.3.2 Working Principle

In XRD, the X-rays fall on the array of atoms in a crystalline sample and diffract by satisfying the Bragg's law. In powder diffraction method, the fine powder of desired sample is irradiated by the monochromatic beam of X-ray. The diffraction takes place from the planes of each NP and diffraction pattern is obtained. The obtained pattern corresponds to the different crystallographic structure of sample and matched with the standard JCPDS card to identify the phase.

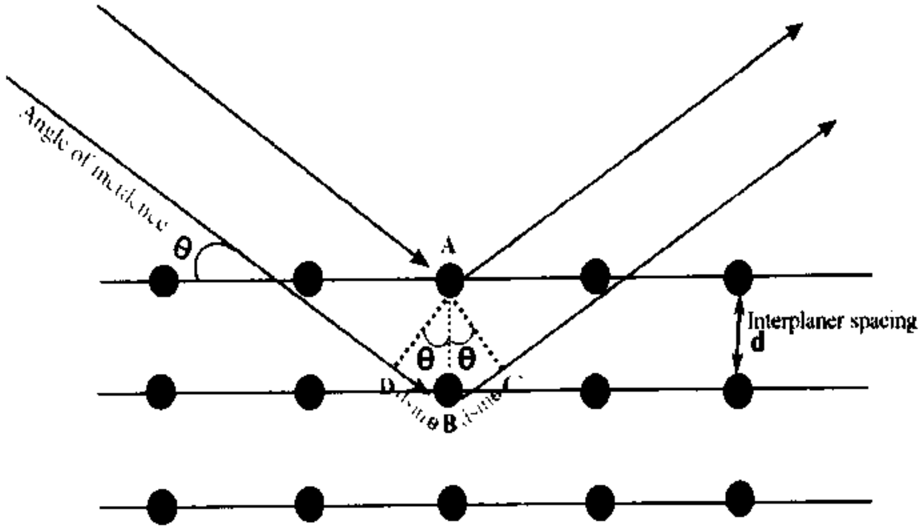

Figure 3.2: Interpretation of Bragg's law diffraction through the crystal.

The single diffraction peak belongs to each atomic plane of the crystallite. The variation in width of the diffraction peaks gives the information about the size of crystallite. The narrow and sharp peak is obtained for the bulk material due to long range atomic arrangement which are responsible for sharp constructive interference pattern. However, in smaller crystallites, such long arrangement of atoms is not present and thereby produces relatively wider constructive interference patterns. The <D> can be estimated by using the Debye's Scherer's formula [83].

3.3.3 Fourier Transform Infrared Spectrophotometer (FTIR)

FTIR is a device used to obtain the IR spectrum of emission or absorption of liquid, solid or gas sample. The actual spectrum is obtained from the raw data by the mathematical process of Fourier transformation. The basic principle behind any spectrophotometer is to measure the absorbed light by the sample at each wavelength. In FTIR spectroscopy, a beam of light (usually infrared) containing many frequencies is made to fall on the sample and absorbance or transmittance is observed as shown in Figure 3.3. After that, the light beam is modulated with different combinations of frequencies and second data point is acquired.

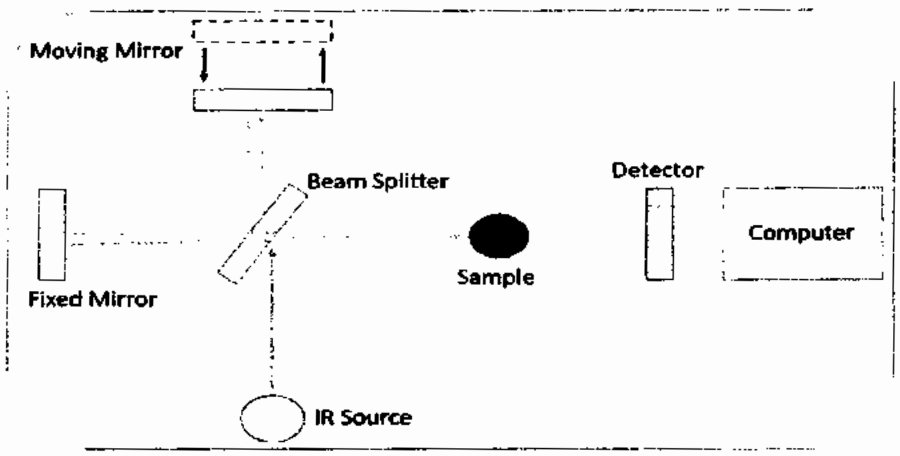

Figure 3.3: Schematic diagram representing the working principle for FTIR spectrophotometer.

This process is continuously repeated over a short time span and the data obtained is fed to the computer where it is processed and inferred that how much absorption is for each wavelength. Therefore, the light source used for the measurement should be broadband containing all spectrum of wavelengths. The light beam falls on the Michelson interferometer which contain a fixed and a movable mirror. Each wavelength is periodically blocked or transmitted, by the movement of mirror. Hence, different modulated wavelengths were obtained at different rates with each minor movement of mirror and the spectrum of light beam is obtained. The raw data obtained is called interferrogram which is processed by the computer and absorption at each wavelength is monitored. The algorithm used for the processing is called Fourier transform which converts one domain (displacement of mirror in cm) to other domain (wavenumber in cm^{-1}). The most common source of light used for FTIR spectrophotometer is silicon carbide element which is heated upto 1200 K and mid-IR region (2-25 μm or 5000-400 cm^{-1}) is obtained.

3.3.4 Scanning Electron Microscopy (SEM)

SEM is widely used to observe the shape and surface morphology of NPs. There is a fine focused beam of electrons generated by thermionic emission from electron gun is made to fall on the sample surface as shown in Figure 3.4. The electron beam is accelerated towards anode by providing huge potential difference (~1-40 kV). In order to produce the fine focused beam of electrons, condenser lenses are used. The scanning coils help the electron beam to move along the x and y-axes to scan the whole sample under investigation.

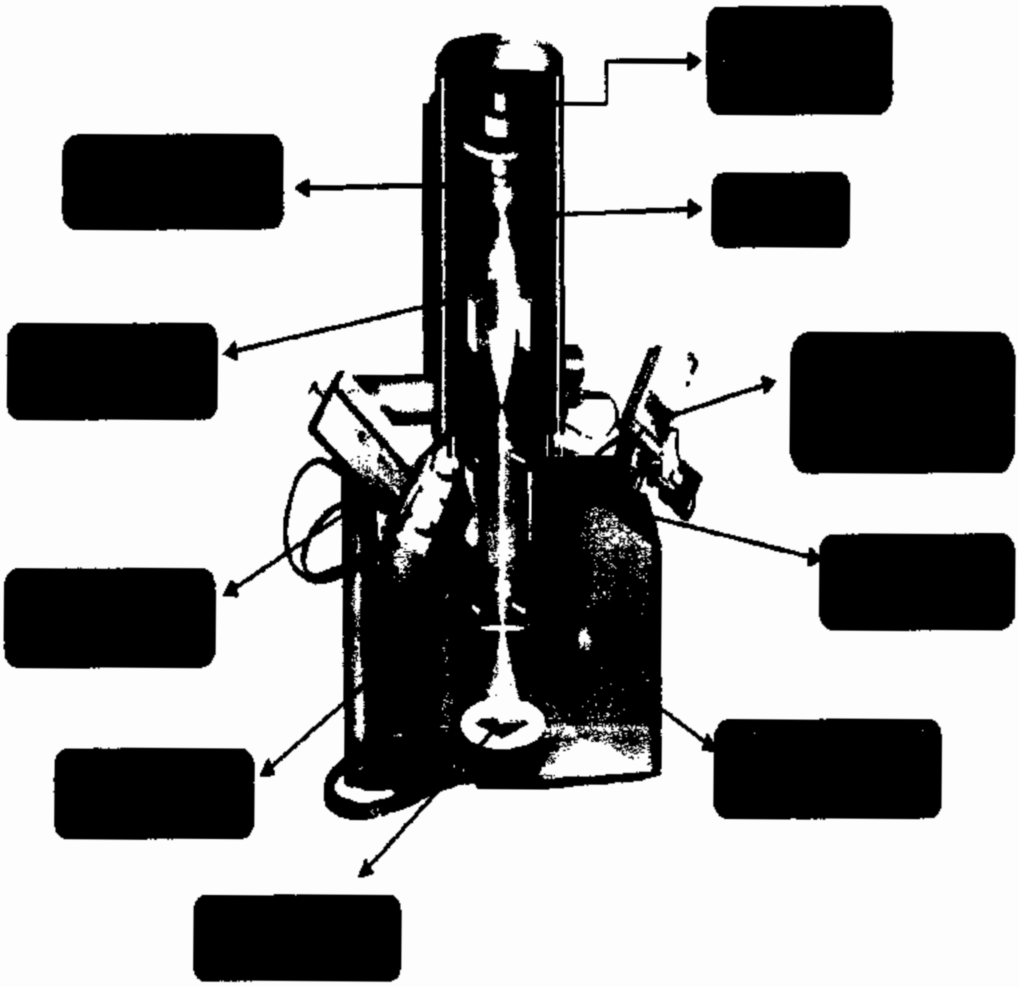

Figure 3.4: Scanning Electron Microscope with labeled components [84].

The primary beam of electrons from the electron gun interact with the sample at various depths and produces a number of signals such as characteristic X-rays, reflected or backscattered electrons (BSE), secondary electrons (SEs) and transmitted electrons. It is not common for a single machine to have all detectors installed, however SEs detector is common in all standard SEMs. The energy of the SEs is usually very low (~50 eV) which limit its mean free path in solid, therefore, it only emerges from the just few nanometer depth from the sample surface. The characteristic X-rays are generated when the electron beam strikes the atoms of the samples and remove inner shell electrons and as a result high energy electrons come to fill the shell by releasing excess energy as characteristic X-ray photons. The detector used to process the characteristic X-rays data helps to identify the material under investigation and its abundance. For the clear imaging, an evacuated chamber is used for the microscopic analysis of the sample.

3.3.5 Transmission Electron Microscopy (TEM)

TEM is a high resolution imaging technique used for the detailed analysis of material through transmission of high energy electrons.

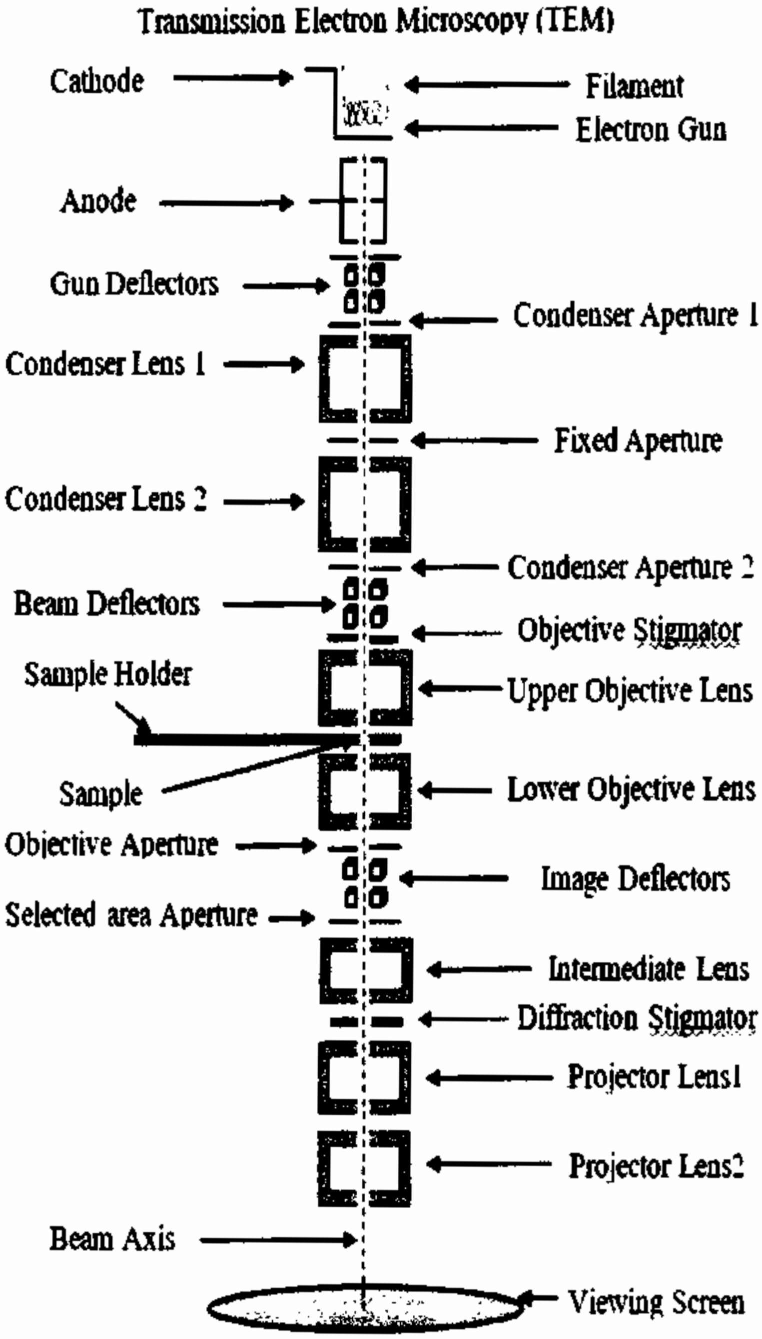

Figure 3.5: Schematic diagram for TEM.

The electromagnetic lenses are used in TEM instead of optical lenses which are commonly used in optical microscopy as shown in Figure 3.5. The Lorentz force is behind the working principle of electromagnetic lenses. The change in magnetic field adjust the focal length of electron beam to produce sharp image of the specimen. The beam of electron is produced by the electron gun and accelerated by applying large potential difference between anode and cathode. The electromagnetic lenses turn the electron beam into fine parallel beam to enhance the resolution of the system. The sample to be examined is adjusted between the magnetic objective lenses and electron beam is allowed to pass through it. The first image get formed after 1st projection lens, however its selected area is again projected for more magnification.

The different types of image contrast are implicated in TEM. The mass thickness contrast generates due to the thickness of sample. The energy get absorbed where the thickness is more and transmit easily at relatively thin portion. Therefore, the image obtained is dark where there is more mass and vice versa. The image obtained in TEM is not only by the transmitted electrons but also from the diffracted electrons from the crystalline sample. Therefore, the diffraction contrast appear in crystalline samples in comparison to amorphous where it is very difficult to get distinct image. The phase contrast is obtained if there is phase difference between the transmitted and diffracted electrons.

3.3.6 Superconductor Quantum Interference Device (SQUID) Magnetometer

For magnetic measurement of samples, SQUID magnetometer is considered as one of the most sensitive device to analyze the magnetic properties of the samples. The SQUID coils are superconducting and able to produce large magnetic field (latest up to 14 T). SQUID magnetometer consist of a super-conducting coil with small insulating layer known as Josephson junction. In order to produce the large field, a large amount of current is needed to pass through the coils, which is only possible if coils are superconductor. The phenomenon of superconductivity occur at low temperature due to generation of Cooper pairs [85]. The Cooper pairs are basically pair of free electrons that are bounded through electron-phonon interaction at low temperature. This Cooper pair state is responsible for the superconductivity phenomenon presented by BCS theory. The schematic diagram of SQUID containing closed superconducting loop and two Josephson junctions is shown below in Fig. 3.6.

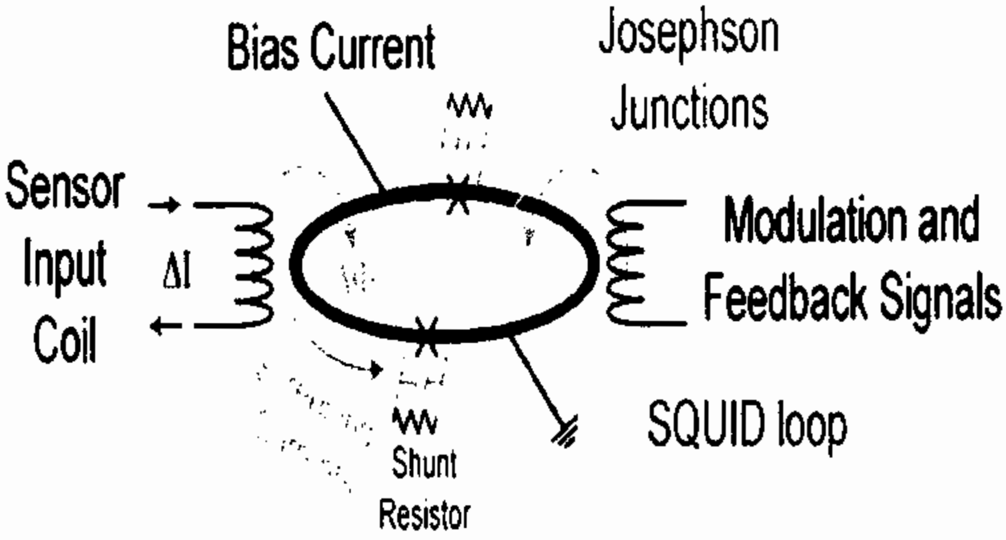

Figure 3.6: Schematic diagram for superconducting coil with Josephson junctions [86].

The Josephson junction consist of two superconductors disjointed by a very thin non-conducting (insulating) layer. The Cooper pairs are represented by wave functions on both sides of the junction similar to the free particle wave function.

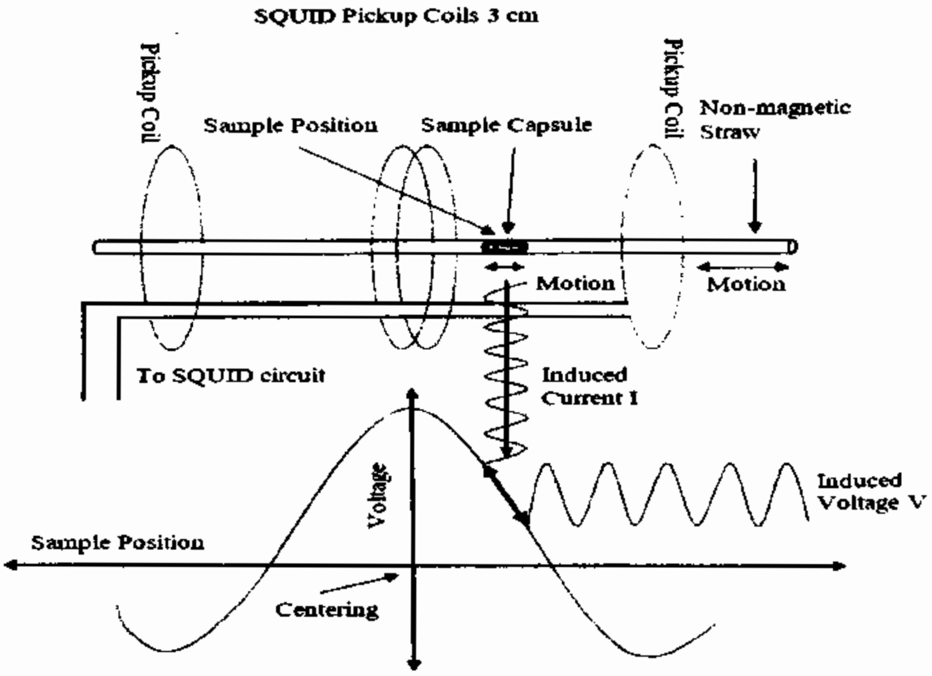

Figure 3.7: SQUID pickup coils setup with moving sample capsule and sample position verses coil voltage graph [86].

The current flows in the junction without presence of any voltage and found proportional to the phase difference of these two wave functions, known as DC Josephson effect.

Furthermore, time derivative of phase difference is directly proportional to the voltage induced across the contact. Hence, change in magnetic flux can be turned into electrical voltage which is the basic principle behind the SQUID magnetometer. However, in AC Josephson effect, Josephson junction oscillate with the frequency proportional to the voltage applied. Therefore, the Josephson junction has become standard measure of voltage due to capability of measuring frequencies with great accuracy.

For the measurement, sample is moved between the three pickup coils which are made up of superconducting material as shown in Figure 3.7. When the sample is moved, an alternating magnetic flux produces in the pickup coils which is transferred to the SQUID device where it is amplified and transformed to voltage.

The magnetic measurements that can be taken from the SQUID magnetometer are:

3.3.6.1 M-H Loop Measurement

The NPs magnetization is measured by static magnetization measurement and thus its saturation magnetization is estimated. The magnetization of the sample under investigation is measured as a function of external magnetic field for at least one complete cycle.

3.3.6.2 Zero Field Cooled and Field Cooled (ZFC/FC) Measurement

The temperature dependent ZFC/FC measurement of the sample is taken to observe the magnetic anisotropy, average blocking temperature, surface freezing temperature for AFM materials and inter-particle interaction of magnetic NPs. In ZFC protocol, the sample under investigation is first cooled in the absence of applied magnetic field from room temperature to lowest possible temperature (usually 5 K) without taking any measurement. Then a small dc field (50 or 100 Oe) is applied and magnetic moment is measured by warming the sample from 5 K to 300 K. In FC protocol, the sample is cooled again from 300 to 5 K in the presence of same applied dc field and magnetization is measured.

3.3.6.3 ZFC/FC Magnetic Relaxation Measurement

The magnetic relaxation phenomenon can be observed in ZFC/FC protocol. In ZFC protocol, the sample is cooled in the absence of any applied magnetic field and after reaching at desired low temperature, dc field is switched ON and magnetic relaxation is observed as a function of time. However, in FC protocol, sample is cooled to a desired low temperature in the presence of applied magnetic field and then field is switched OFF and magnetic relaxation is observed as a function of time.

3.3.6.4 AC-Susceptibility Measurement

In this protocol, a small ac magnetic field (amplitude of 5 Oe) is applied at different frequencies, e.g 1, 10, 100, 1000 Hz. The dynamic response built upon the relaxation mechanism of particle (Néel's and Brown's relaxation) and time constants that provide complex magnetic susceptibility $\chi(f)$, which consist of real $\chi'(f)$ and imaginary $\chi''(f)$ parts.

$$\chi(f) = \chi'(f) + \chi''(f) \tag{3.7}$$

The real part and imaginary parts of ac susceptibility is given by Debye's theory

$$\chi'(f) = \frac{\chi_{DC}}{1+(f\tau_{eff})^2} \tag{3.8}$$

$$\chi''(f) = \frac{\chi_{DC} f\tau_{eff}}{1+(f\tau_{eff})^2} \tag{3.9}$$

χ_{DC} is the DC magnetic susceptibility and τ_{eff} is the effective relaxation time of magnetic NPs.

3.3.7 UV-Vis Spectrophotometer

For the investigation of optical behavior of a material, UV-Vis spectrophotometer is commonly used to characterize the different materials. It usually compares the light intensity passing through the sample (I) to the light intensity passing without sample (I_o) in the holder. The ratio $({}^{I}/{}_{I_o})$ is called transmittance and usually expressed in (%T). The absorbance (A) can also be calculated from transmittance [87],

$$A = -\log({}^{\%T}/{}_{100\%}) \tag{3.10}$$

The basic parts of spectrophotometer are: light source, diffraction grating or prism to separate different wavelengths and a detector. The different types of radiation sources are being used in spectrophotometer such as tungsten filament (300-2500 nm), Xenon arc lamp (160-2000 nm), deuterium arc lamp (190-400 nm) and light emitting diodes for visible spectral region (400-700 nm). The different type of detectors are being employed in spectrophotometer such as photodiode array, photomultiplier tube, photodiode, and charged coupled device (CCD). The schematic diagram of the UV-Vis spectrophotometer is shown in Figure 3.8.

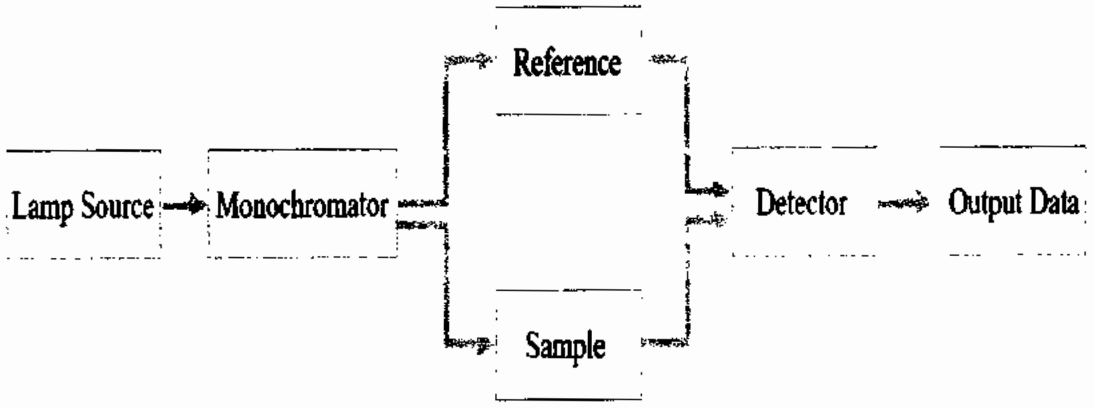

Figure 3.8: Schematic block diagram for UV-Vis spectrophotometer.

The single beam and double beam are the two types of spectrophotometers. In single beam spectrophotometer, the intensity of light is being measured without presence of sample in the cuvette and then again measured in the presence of sample. However, in double beam case, the initial beam divides into two parts. One passes through the sample solution under investigation while other passes through the solvent (used as reference). The intensity of the beam passing through the solvent (reference) considered to be 100 %. The specific wavelength of light get absorbed by the sample and the remaining light is collected by the spectrograph which consist of a diffraction grating and CCD sensor to record the data. The samples are most often in liquid solution form and located in a transparent cell (cuvette) which is typically in rectangular shape with cubic cross-section of side width 1 cm. It is made up of transparent material such as quartz glass and fused silica. The width of cuvette is taken as the path length (used in Beer-Lambert law).

The absorbance or reflectance of a part of ultraviolet and visible spectral regions gives the deep insight to the electronic transitions in atoms and molecules of that material. Basically, there are three types of ground state bonding orbitals, (i) σ bonding molecular orbital, (ii) π bonding molecular orbital, (iii) n non-bonding molecular orbital (contain lone pairs) and two types of anti-bonding molecular orbitals, (i) σ^* anti-bonding molecular orbital, (ii) π^* anti-bonding molecular orbital. The n^* anti-bonding molecular orbital does not exist due to the absence of n bonding electrons. Thus, transition of electron from σ

bonding orbital to σ^* anti-bonding molecular orbital is referred to as σ to σ^* transition same like π-π^*, n–σ^* and n–π^* transition.

The type of bond can be correlated by the wavelength of absorbing peak and can be useful in determining the functional group within a molecule. The absorption spectrum depends upon the nature of solvent, its temperature, pH of solution, electrolyte concentration and also presence of interfacing substances. Therefore, for accurate analysis, these parameters must be controlled to identify the material under investigation.

3.3.8 Raman Spectrometer

Raman spectrometer is a device used to determine the vibrational modes of a molecule. It gives the structural fingerprint of any material by which molecules can be identified. Raman spectrometer typically consist of four basic units:

3.3.8.1 Laser as Excitation Source:

Laser is used as excitation source and the sample under study is illuminated by laser. The bandwidth of the laser signifies the resolution of spectrum. The shorter wavelengths give stronger Raman scattering due to increase in Raman cross-section with frequency.

3.3.8.2 Sample Illumination and Light Collection Optical System:

The electromagnetic radiations are produces from the illuminated spot. These radiations are collected by the lens and sent through the monochromator.

3.3.8.3 Wavelength Selector such as Filter:

Rayleigh signal and reflected laser signal contain Raman scattered light which needs to be separated for achieving a high quality Raman spectra. This is done by using optical laser rejection filters such as long-pass, Notch filter, band pass filter, edge pass filter, etc.

3.3.8.4 Detector:

In earlier times, photon counting photomultiplier tubes (PMT) were being used as detectors. However, the main drawback was that, it took a substantial period of time for wavenumber scanning mode. Nowadays, detectors such as photodiode array (PDA) and charged coupled devices (CCDs) are being used. The performance and sensitivity of modern CCDs are much improved and being widely used by researchers all over the world. For different wavelength ranges, different types of CCDs are used to get optimized results. Generally, intensified CCDs are used when the signal strength is very weak. The focal length of spectrograph and size of CCD defines the spectral range.

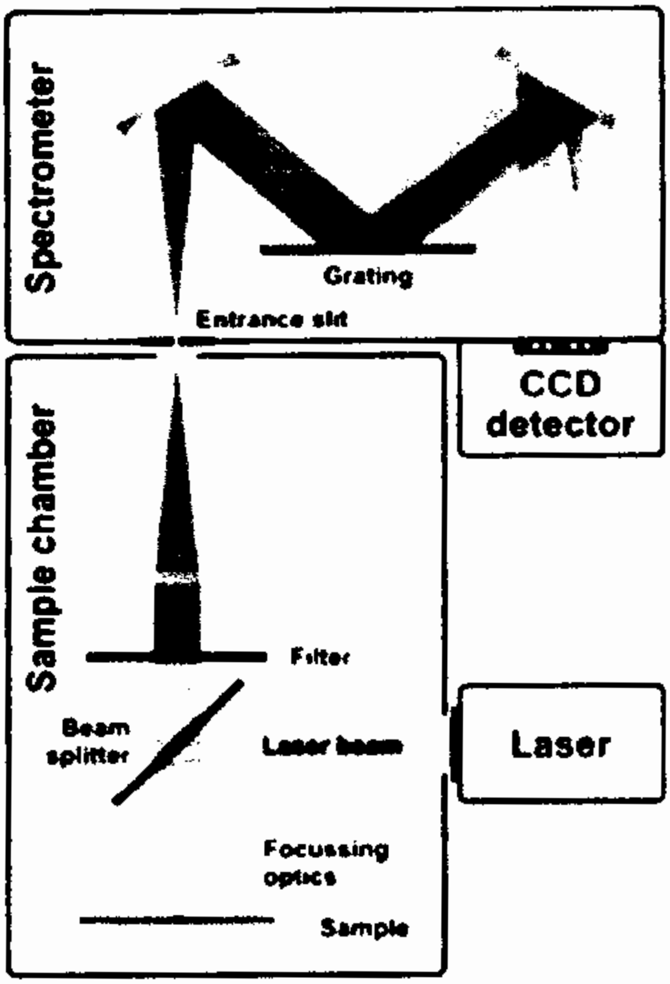

Figure 3.9: Schematic diagram representing the working principle for Raman spectrometer [88].

The basic principle behind Raman spectroscopy is; when photons are being scattered (from a molecule or crystal), then most of these photons scattered elastically (without losing any energy), known as Rayleigh scattering. However, a very small number of photons scattered in-elastically (gain or lose some energy) and have different frequency from the incident photon, known as Raman scattering or Raman effect. If a monochromatic light such as laser is illuminated on substance under study, a strong line in the frequency spectrum appears as incident photons, represents the elastic scattering of these laser photons. However, there will be two weaker lines (Stokes and anti-Stokes) on either side of strong line indicating the shift in energy (frequency) from the incident photons representing inelastic scattering of these laser photons as shown in Figure 3.10.

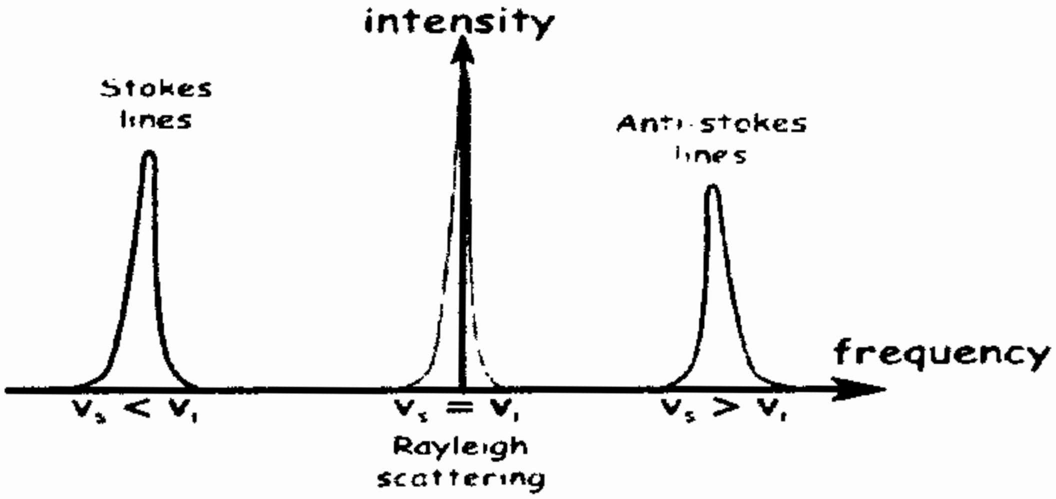

Figure 3.10: Categorizing Raman and Rayleigh scattering [89].

The laser photon excite the sample and put the molecules in a virtual energy state for a short time and finally comes to ground state after photon emission as shown in Figure 3.11.

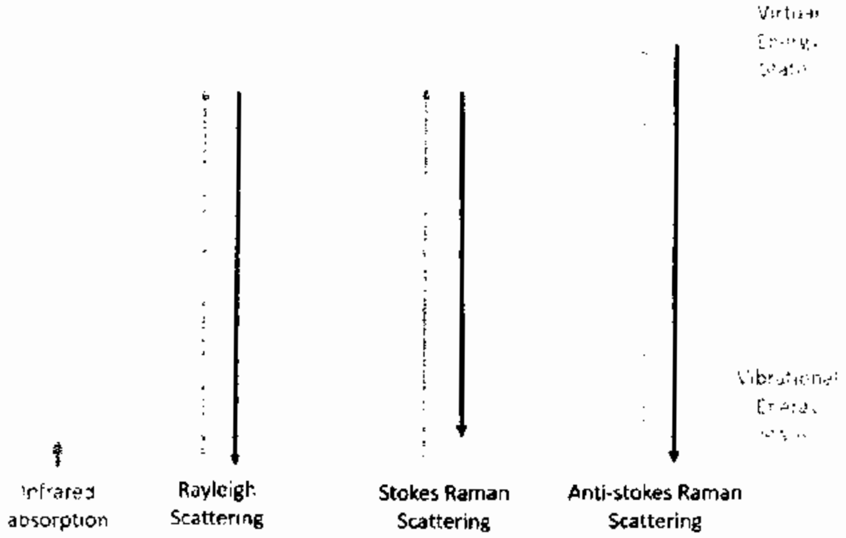

Figure 3.11: Virtual transition states of Raman and Rayleigh scattering [90].

The emitted photon may have greater or lower energy than the incident photon and the sample set into a different vibrational, rotational and electronic state. For the conservation of total energy, the emitted photons energy must have energy equal to the energy difference of initial and final vibrational, rotational and electronic energy state. There are two types of energy shifts:

Stokes shift: If the final state energy is higher than the initial state energy, then the scattered photon energy must be lower than the incident photon (as per energy conservation). Hence, the scattered photon shifts to the low frequency and known as Stokes shift.

Anti-stokes shift: If the final state energy is lower than the initial state energy, then the scattered photons energy must be greater than the incident photon and as a result scattered photon shifts to higher frequency known as anti-stokes shift.

Hence, Raman scattering intensity depends upon the rotational, vibrational and electronic state of the molecule before and after excitation by laser photons. Raman's effect is different in the sense that there is no real transition between the energy levels of molecules as it happen in absorption and emission process. When a complex molecule interact with a photon, some higher vibrational states get observed which are called normal modes of vibrations of a molecule. Each normal mode possess motion such as:

(i) Bending motion
(ii) Stretching motion
(iii) Out-of-plane deformation

The spectrum depends upon the strength of chemicals bonds, atomic arrangement and masses of atoms in a molecule. Therefore, different vibrational spectra ''fingerprints'' is observed for different molecules. The polarizability (P) is the interaction between the electron cloud of sample and external electric field of laser induces a dipole moment and given,

$$P = \alpha E \tag{3.11}$$

The proportionality constant α defines the polarizability of a molecules. The molecular vibration changes the polarizability and hence Raman scattering occur. Hence, there should be change in polarizability during the vibration (Q), that is

$$\frac{d\alpha}{dQ} \neq 0 \tag{3.12}$$

The collective vibrations in crystals are due to the superposition of virtually propagating plane waves, called normal mode of vibrations (phonons). The normal mode coordinate, $Q = Q_o \cos 2\pi \nu_{vib} t$, classify either stretching, bending or torsional mode.

For a solid with N unit cells and p atoms per unit cell, contains (3pN-6) phonons and all propagating with their wave vectors $(\vec{k})$. If the modes are with in-phase oscillation with the neighboring atoms, known as acoustic vibrations and for out of phase oscillation with neighboring atoms, known as optical vibrations. Phonons are also referred as longitudinal for parallel movement of atoms to the direction of wave propagation $(\vec{k})$ and transversal for perpendicular movement of atoms in the direction of wave propagation $(\vec{k})$.

3.3.9 Neutron Diffraction (ND)

It is used to study the nuclear and magnetic structure of a given material. The sample under investigation is exposed to the beam of neutrons and the observed diffraction pattern gives the information about the nuclear and magnetic unit cells. The principle of ND is almost similar to XRD, however neutrons have more penetrating power that make it suitable for studying the complex and bulky structures. Also X-rays interact with the electron cloud that surround the nuclei and therefore intensity contribution is large for atoms with greater atomic number. However, the neutrons directly interact with nucleus of atom and therefore can differentiate lighter nuclei even in the presence of larger nuclei. The neutron beam is directly sensitive to the position of nuclei in the atom and penetrate deeply into the material. Neutrons are highly sensitive for investigating the minority components of sample and equally good for to study the interfaces of atomic thickness.

This technique requires a neutron source. The naturally occurring free neutrons are very rare, however bound in atomic nuclei or present in neutron star. The artificial methods to free the neutron from the nuclei are fission process or spallation. The crystal monochromator and filters are used to obtain the desired wavelength of neutrons. The fission process in a nuclear reactor is common to produce the beam of neutrons. When this beam strikes with the material under investigation, it scatters at well-defined angles according to the Bragg's law. The obtained diffractograms show peaks even at high angles with superb high resolution indicating the precise atomic positions in the crystal structure. Neutron being a neutral particle, still carry a net magnetic moment that interact with magnetic moments and therefore reveal the magnetic structure of the given material under investigation. The vanadium cylinder is often used as a container for holding the powder sample due to the reason that its nuclei hardly scatters the neutrons.

3.3.10 Ferromagnetic Resonance Spectrometer

Ferromagnetic resonance (FMR) is technique used to measure the dynamic properties of magnetic materials. The FMR principle is based on the fact that the magnetic moments of atoms/ions rotate (called precession) with the same applied microwave frequency when resonance condition occur at applied resonance field H_r. The absorption of microwave frequency occur by the sample at resonance field H_r. The basic configuration of FMR experimental setup is shown in Figure. 3.12.

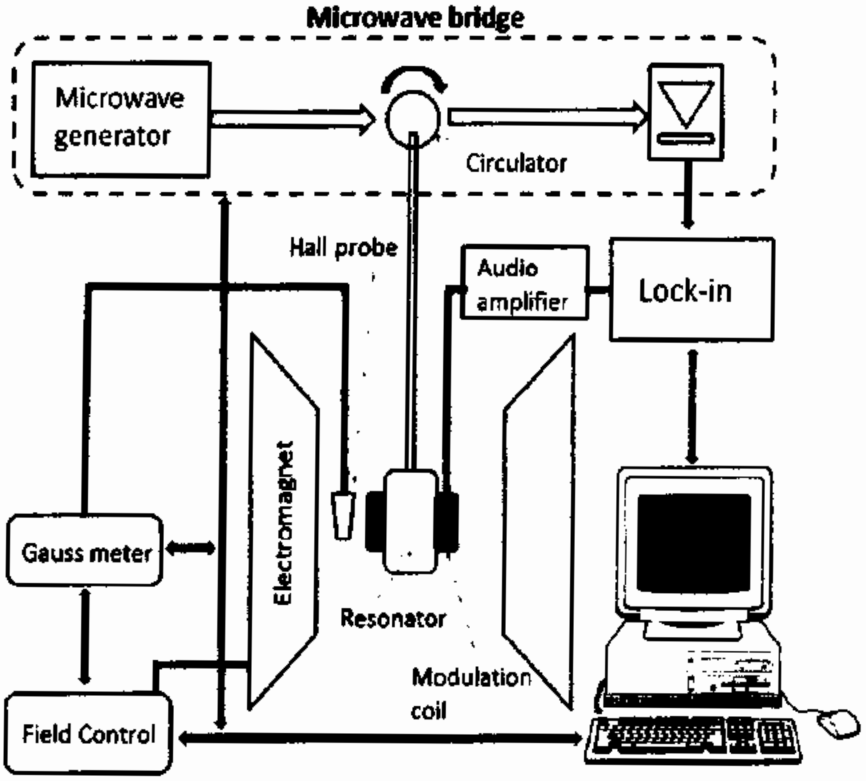

Figure 3.12: Basic configuration of FMR experimental setup [91]

FMR spectrometer is an instrument used to measure the EM waves absorbed by the sample under the influence of external DC magnetic field. It consists of an EM microwave generator, transmission line and detector. The magnetic materials have precessional frequency in the range of microwaves from 0.1 to 100 GHz, therefore absorption occur in this frequency range. For cavity resonator, sample is mounted inside the cavity in between the modulation coils where as in stripline, sample is placed on top of coplanar wave guide. The detector records the changes in either transmittance or reflectance of microwaves. Most of the FMR spectrometers measure the reflectance at a fixed frequency while sweeping the magnetic field. The EM waves travel through the metallic cavity via a wave guide and falls on the sample. The signal is reflected back from the sample and passes through the same waveguide to the detector while passing through the Schottky diode [91]. An additional small ac modulation field was applied to the samples, and the lock-in amplifier was referenced by the modulation signal. In these conditions, the output voltage of the lock-in amplifier scales as the first derivative of the FMR absorption signal with respect to the applied field ("differential absorption").

CHAPTER NO. 4

Effect of Silica Coating on Optical and Magnetic Properties of NiO Nanoparticles

In this chapter, effect of different SiO_2 concentration on the optical and magnetic properties of NiO nanoparticles have been studied.

4.1 Photocatalytic Activity and Two-Magnon Behavior in NiO Nanoparticles with Different Silica Concentration

The nanoparticles (NPs) are usually dispersed in SiO_2 matrix to reduce the average crystallite size (<D>), agglomerations and enhance optical and magnetic properties [92-96]. SiO_2 is usually preferred due to its chemical stability, bio-compatibility, non-toxic nature, adjustable pore diameter and chemical inertness [97]. Vaidya *et al.* [98] observed a decrease in core size with increasing SiO_2 concentration for the core-shell structure of NiO/SiO_2 NPs. *In-situ* formation of SiO_2 matrix has the ability to reduce the particle size which in turn can change the optical, magnetic and photocatalytic properties of NPs.

NiO NPs has been widely used as photocatalyst [99-102]. The smaller size NPs have large surface area and therefore reported as efficient photocatalyst [100]. In oxides, defects such as oxygen vacancies are important for controlling the properties of NPs. Li *et al.* [103] presented a brief study about the physical properties and oxygen vacancies in ZnO nanostructures. Though few reports of NiO nanocomposites are available in the literature [104-109] for photocatalytic degradation but the effect of different SiO_2 concentration on structural, optical, magnetic and photocatalytic properties of NiO NPs has not been yet studied in detail.

Bulk NiO is antiferromagnetic (AFM) due to antiparallel ferromagnetic (FM) sheets of Ni^{2+} ions along (111) plane. When the size of NiO NPs get reduced, the number of uncompensated surface spins increases due to large surface to volume ratio and magnetic transition from AFM to paramagnetic (PM) or superparamagnetic (SPM). Mironova *et al.* [110] observed the AFM to PM phase transition in NiO NPs on reducing <D>. On decreasing

<D>, the surface defects such as Ni or oxygen vacancies increases which alter the properties of NPs. The two-magnon (2M) peak of bulk NiO ~ 1500 cm^{-1} in Raman spectra has magnetic origin and vanishes at Néel temperature (T_N=523 K). The presence of 2M peak indicates the AFM ordering in NiO, which vanishes at the nanoscale due to the symmetry breaking of the superexchange interactions of Ni-O. The presence of one-phonon (1P) longitudinal optical (1LO) mode ~ 524 cm^{-1} in Raman spectroscopy indicates the non-stoichiometry in NiO. Fukushima *et al.* [111] presented a brief study on variation in peak intensity and Raman shift due to the presence of oxygen vacancies in ZnO single crystals. Cazzanelli *et al.* [112] observed a decrease in 1LO peak and increase in 2M peak with increasing synthesis temperature of Mg doped NiO polycrystalline solid solutions and attributed it to lower vacancy concentration at higher temperature.

In this chapter, we have studied the photocatalytic activity and two-magnon behavior of NiO NPs dispersed in different (0, 30, 50, 60, 70 at.%) SiO_2 concentration and then investigated the magnetic behavior of smallest obtained NiO NPs.

4.2 Results and Discussion

4.2.1 X-ray Diffraction (XRD)

It was used to identify the phase structure and purity of all the samples. Fig. 4.1 (a) shows the XRD patterns of NiO/SiO_2 (x) NPs with x = 0, 30, 50, 60 and 70% at room temperature. The peaks at angles 37.29°, 43.29°, 63°, 75.51° and 79° correspond to (111), (200), (220), (311) and (222) planes, respectively. All diffraction peaks are coinciding and matching with standard pattern (JCPDS No. 75-0197) of NiO. There were no peaks observed for SiO_2 due to its amorphous nature. The average crystallite size <D> of the NPs was calculated by Debye's Scherer's formula [83], $D = \frac{K\lambda}{\beta\cos\theta}$ where K is the shape constant and its value is taken as 0.91 for spherical morphology of NPs. λ is the wavelength of CuKα X-rays and its value is 0.154 nm. Fig. 4.1 (b) shows the variation in <D> of NiO/SiO_2(x) NPs with x = 0, 30, 50, 60 and 70%. The <D> of NiO/SiO_2(x) NPs with x = 0% was found maximum i.e. 57 nm and showed decreasing trend with increasing concentration (x) (minimum 14 nm at x = 60 %).

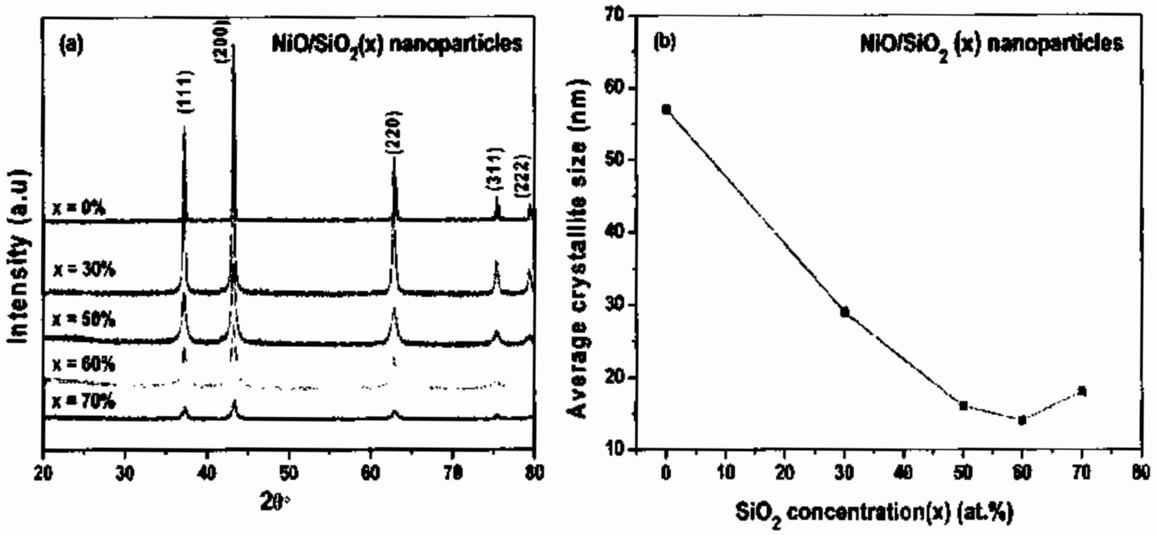

Figure 4.1: (a) XRD patterns of $NiO/SiO_2(x)$ nanoparticles with x = 0, 30, 50, 60 and 70% and (b) variation of <D> with x.

It is due to the generation of large number of nucleation centers which constraint the growth of NPs [113]. Casu *et al.* [31] reported that NiO NPs do not interact with SiO_2 and grow as a separate phase in SiO_2 matrix. The SiO_2 matrix acts as a spacer between magnetic NPs and reduced agglomeration [97].

4.2.2 Fourier Transform Infrared Spectroscopy (FTIR)

It is widely used technique to explore the chemical bonds present in the material under study. The information about the presence of amorphous phase of SiO_2 is not completely extracted from the XRD, therefore FTIR was used to unfold the presence of SiO_2. The potassium bromide (KBr) palletized method was employed to find the FTIR spectrum. Fig. 4.2 shows the FTIR spectra confirming the formation of $NiO/SiO_2(x)$ NPs with x = 0, 30, 50, 60 and 70%. The dip at 440 cm^{-1} is assigned to stretching vibration mode of Ni-O molecule [114]. The bands at 800 and 1050 cm^{-1} correspond to Si-O-Si symmetric and asymmetric stretching vibration modes respectively, which confirms the formation of SiO_2 matrix [115].

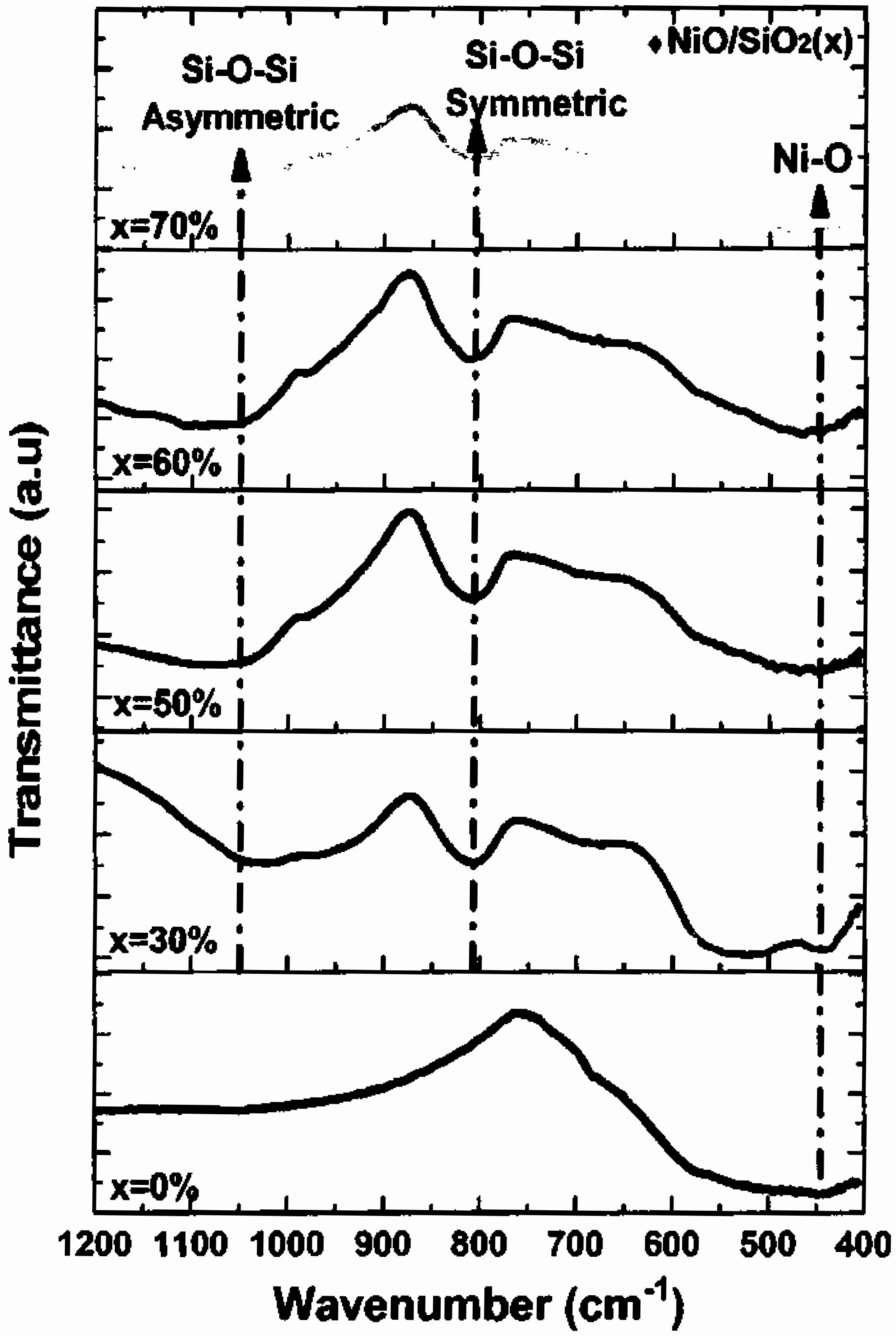

Figure 4.2: FTIR spectra of $NiO/SiO_2(x)$ nanoparticles with x = 0, 30, 50, 60 and 70%.

4.2.3 Energy Dispersive X-ray Spectroscopy (EDX)

EDX was used to confirm the elemental composition of the material. Fig. 4.3 (a) and (b) shows the EDX spectrum of $NiO/SiO_2(x)$ NPs with x = 0 and 60%. The peaks belonging to Ni, Si and O confirm the purity of samples. The presence of peak at 2.1 keV in both samples is due to gold sputtering.

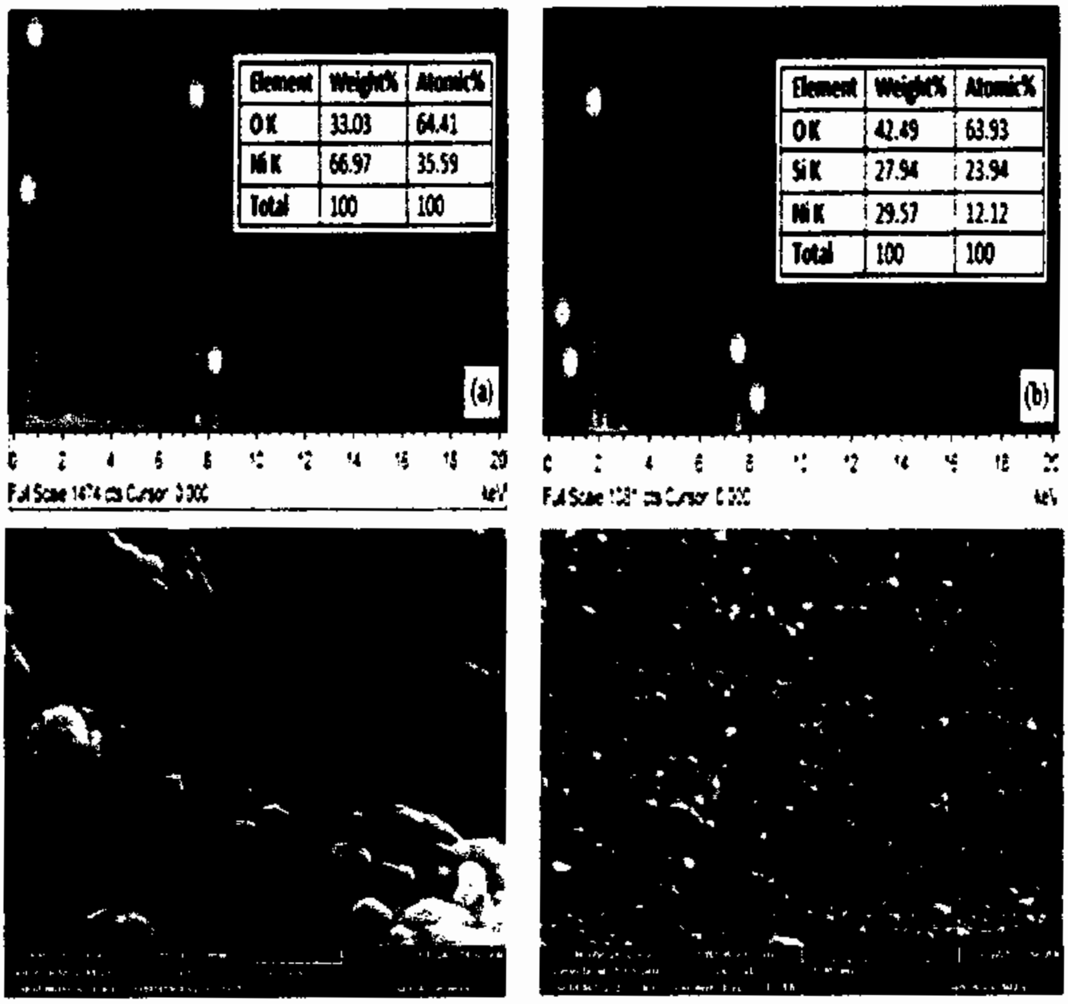

Element	Weight%	Atomic%
O K	33.03	64.41
Ni K	66.97	35.59
Total	100	100

Element	Weight%	Atomic%
O K	42.49	63.93
Si K	27.94	23.94
Ni K	29.57	12.12
Total	100	100

Figure 4.3: EDX spectrum of $NiO/SiO_2(x)$ nanoparticles with (a) x = 0% and (b) x = 60% and SEM images of $NiO/SiO_2(x)$ nanoparticles with (c) x = 0% and (d) x = 60%.

4.2.4 Scanning Electron Microscopy (SEM)

SEM was used to investigate the surface morphology of the NPs. Fig. 4.3 (c) and (d) shows the SEM images of $NiO/SiO_2(x)$ NPs with x = 0 and 60% at 500 nm scale. It is clear that for x = 0%, NPs are agglomerated and also have wide range of size distribution but for x = 60%, the NPs are smaller in size and have rather smaller size distribution.

4.2.5 Raman Spectroscopy

It is one of the most simple and useful probe to investigate the magnetic nature of AFM material. Raman spectroscopy together with FTIR spectroscopy gives the complete information about the vibrational spectrum of a molecule in ground state.

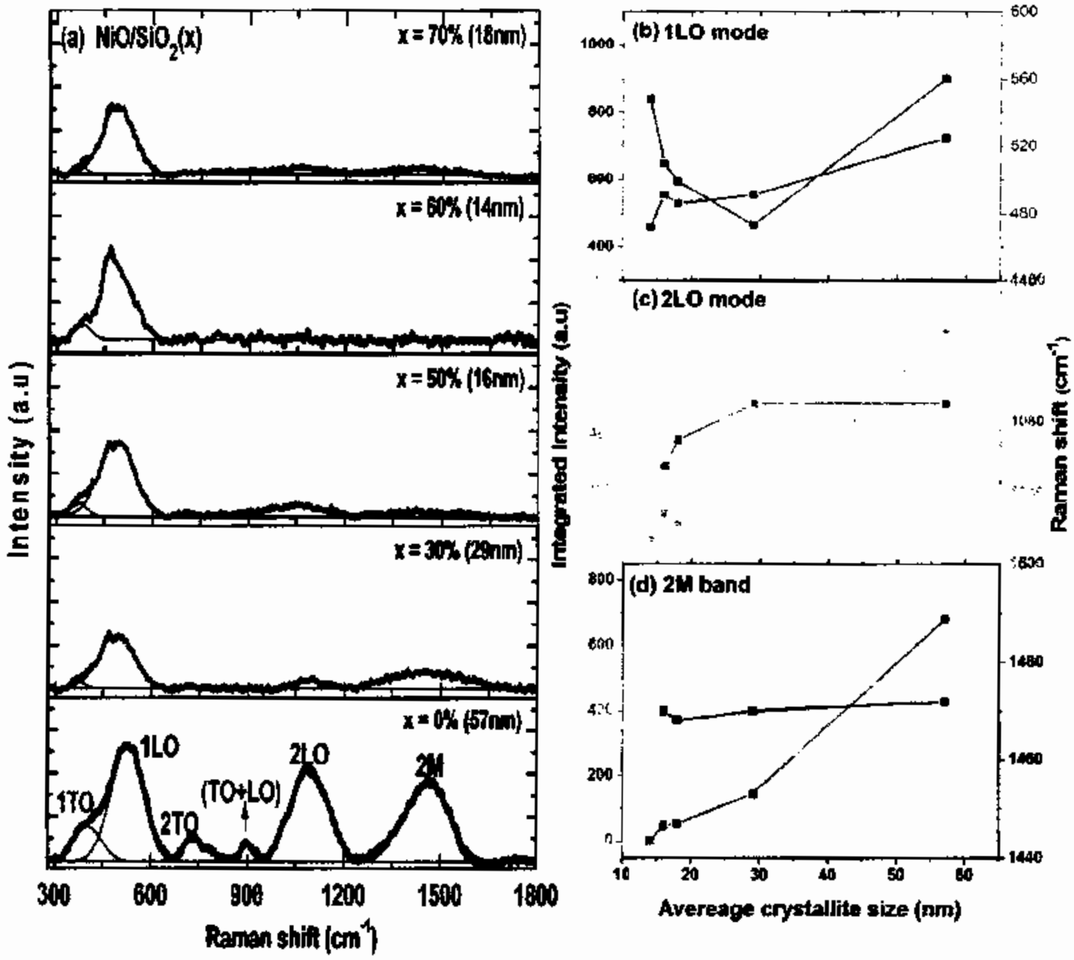

Figure 4.4: (a) Room temperature Raman spectra of NiO/SiO$_2$(x) nanoparticles with x = 0, 30, 50, 60 and 70%, where black, green and red curves represent the experimental data points, Gaussian fit and peak sum, respectively. Panels (b), (c) and (d) show the variation of relative peak height and Raman shift of 1LO, 2LO and 2M with <D>, respectively.

Fig. 4.4 (a) shows the Raman spectra of NiO/SiO$_2$(x) NPs with x=0, 30, 50, 60 and 70%. The Gaussian fit was performed to observe the peak positions accurately. The one-phonon (1P) optical vibrational modes 1TO and 1LO of Ni-O were observed in 300-650 cm^{-1} range due to their overlapping i.e. 1TO ~ 390 cm^{-1} and 1LO ~ 524 cm^{-1}. Patel *et al.* [116] observed the 1TO and 1LO modes of Fe doped NiO NPs at 390 and 534 cm^{-1} respectively. The perfectly stoichiometric cubic NiO did not show one-phonon optical modes, therefore presence of these modes in NiO NPs is attributed to surface defects, imperfectness and Ni or interstitial oxygen vacancies [116, 117]. It can be seen from Fig. 4.4 (b) that the peak intensity of 1LO mode is decreased initially and then increasing with decrease in <D>. The higher peak intensity in large sized uncoated NiO NPs is attributed to the presence of defects such as oxygen vacancies [118]. However, it gets reduced for x = 30% NPs which is attributed to the defects or reduced number of oxygen vacancies in these NPs. On further increasing SiO_2 concentration, the peak intensity showed increasing trend due to decrease in average crystallite and generation of more defects in these NPs in accordance with previous reported study [119]. Gandhi *et al.* [120] observed an increase in integrated intensity of 1LO mode of NiO NPs with decrease in <D> and attributed it to parity-breaking defects. It is also observed that the 1LO mode is shifted to lower wavenumber which is due to reduction in <D> [119]. The two-phonon (2P) optical vibration modes such as 2TO at 730 cm^{-1}, TO+LO at 900 cm^{-1} and 2LO at 1090 cm^{-1} [121] have been observed for x = 0% NPs due to their large <D> and these modes get suppressed in other samples. Patel *et al.* [122] attributed the absence of 2TO and TO+LO modes of Cu doped NiO to nanocrystalline nature. Fig. 4.4 (c) shows that the red shift and decrease in peak intensity of 2LO mode due to decrease in <D> in accordance with reported study on NiO NPs [76]. Ravikumar *et al.* [121] also observed red shift in the peak position of 2LO mode of NiO NPs and attributed it to size induced phonon confinement effect [123]. The peak that originates from two Brillouin zone edge magnons which propagate in opposite direction is known as two-magnon (2M) peak and it is the characteristic peak of AFM material. The band at 1472 cm^{-1} is attributed to two-magnon (2M) scattering and indicates the AFM coupling in the material. This band is present for x = 0 and 30 % NPs which confirms the AFM nature of these NPs due to relatively long spin correlation length in the core of these large size crystallites. However, it gets suppressed for x = 50 and 70 % NPs, and totally vanished for x = 60 % NPs due to decreasing smaller <D> NPs with increasing SiO_2 concentration which is in accordance with XRD results. Fig. 4.4 (d) shows no significant Raman shift in 2M peak, however peak intensity is decreased significantly with decreasing <D>. Wu *et al.* [124] observed decrease in intensity of 2M band of NiO nanowalls with decrease in nanowalls width and attributed it to reduced coordination of surface spins. The absence/suppression of this band at higher SiO_2 concentrations confirms the AFM to SPM transition in smaller NiO NPs. George *et al.* [118] reported the AFM to FM transition in NiO nanofibers due to smaller <D>. The structural disorder in smaller crystallites generates surface spin disorder and provide a net magnetic moment in AFM NPs [125].

4.2.6 Magnetic Properties

When the crystal structure of AFM material is restricted to few nanometers, the uncompensated surface spins play major role due to large surface to volume ratio and give a net magnetic moment. Thus magnetic properties of AFM NPs are strongly dependent on their <D>.

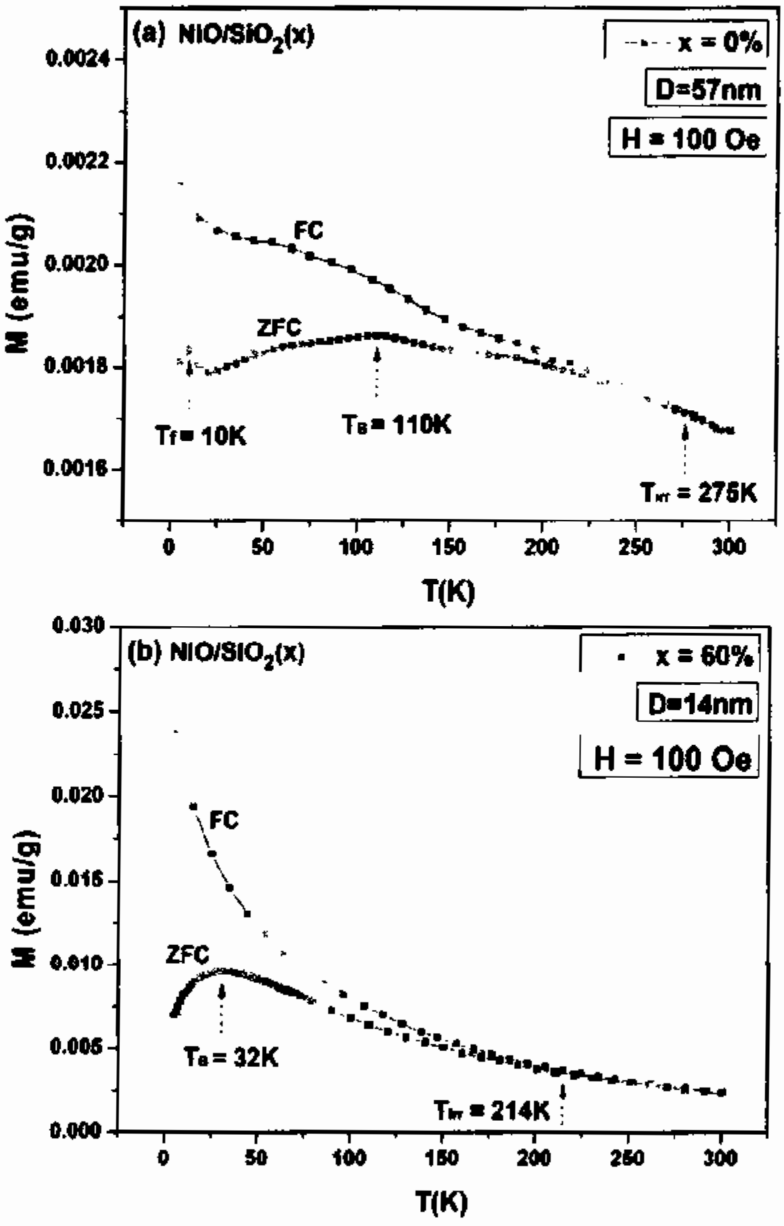

Figure 4.5: ZFC/FC magnetization curves of NiO/SiO$_2$(x) nanoparticles with (a) x = 0 and (b) x = 60%.

Fig. 4.5 (a) and (b) show the temperature dependent ZFC-FC magnetic curves of NiO/SiO$_2$(x) NPs with x = 0 and 60% in the temperature range 5-300 K under magnetic field of 100 Oe. There are two maxima observed in ZFC for x = 0% at 10 and 110 K which are designated as spin glass freezing temperature (T_f) and average blocking temperature (T_B), respectively [41]. Montes *et al.* [46] observed T_f = 6.2 & 6.7 K and T_B = 53 & 145 K for 5 & 10 nm NiO NPs, respectively. A small peak at T_f =10 K is due to the frozen uncompensated spins at the surface of NPs where broader peak at T_B = 110 K corresponds to the thermal relaxation of the uncompensated spins in the core of NPs known as blocking peak [76]. The broadening of ZFC curve around T_B indicates the broader distribution of magnetic moments due to broad size distribution of NPs [126]. On the other hand for x = 60% NPs, T_f was not found while T_B = 32 K which is rather sharp and indicating the relatively small particle size distribution in accordance with SEM image in Fig. 4.3 (d). The T_B value was also found to be decreased from 110 K (x = 0%) to 32 K (x = 60%) due to the decrease in <D> [127]. Above T_B, the thermal energy gets dominant over anisotropy energy and SPM state of NPs was achieved.

The FC curve gives an information about the inter-particle interactions. A sharp increase in the FC magnetization usually observed for non-interacting particles [128]. For NPs with x = 60%, a sharp increase in the FC curve has been observed at low temperatures which indicates the non-interacting NPs and is attributed to the presence of non-magnetic SiO$_2$ between the NPs. This sharp increase in FC can be also associated with their superparamagnetic state [129]. For x = 0% NPs, no such sharp increase in FC curve has been observed at low temperatures which indicates the strong inter-particle interactions. The joining of ZFC-FC curves at a particular temperature is known as irreversibility temperature (T_{irr}) [127] which was found to be decreased from 270 to 214 K with increasing x from 0 to 60% and is attributed to the decrease in <D> [130]. The separation between ZFC-FC at low temperatures is denoted by Δm and was found to be 0.00034 and 0.01685 emu/g for NiO/SiO$_2$(x) NPs with x = 0 and 60%. A smaller value of Δm for x = 0% shows the AFM nature of NPs and a relatively high value for x = 60% NPs shows their SPM nature. These findings are consistent with Raman spectroscopy shown in Fig. 4.4.

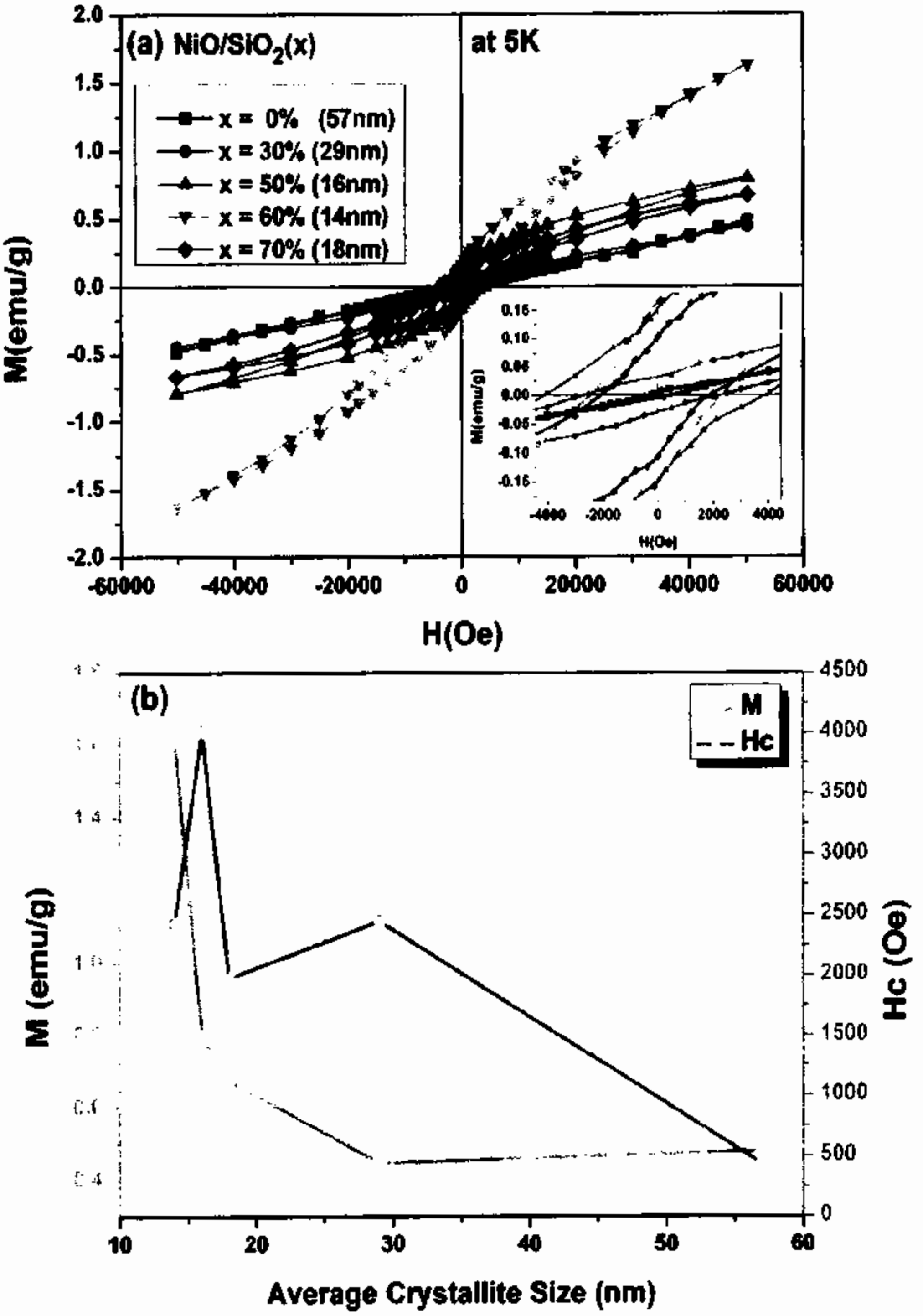

Figure 4.6: (a) M-H loops of NiO/SiO$_2$ (x) nanoparticles with x = 0, 30, 50, 60, and 70% at 5K and (b) variation of magnetization (M) and H$_c$ with <D>.

Fig. 4.6 (a) show the M-H loops of the NiO/SiO$_2$ (x) NPs with x = 0, 30, 50, 60 and 70% at 5 K. It is clear that NPs with x = 0 and 30% show AFM behaviour due to a significant contribution from the AFM core of large crystallites and is in agreement with the Raman spectra in Fig. 4.4. The net magnetization was found to be increased with decrease in <D> as shown in Fig. 4.6 (b). This behavior is quite opposite to FM materials in which magnetization usually decreases with decreasing crystallite size [131]. However, in AFM NPs, the contribution of the magnetization from core is almost negligible due to the equal but oppositely aligned spins and the net magnetization is due to surface spin disorder which increases with decrease in crystallite size [132]. The maximum magnetization and hysteresis was observed for smallest crystallite of 14 nm size for x=60% NPs and showed SPM state which was also observed in ZFC-FC in Fig. 4.5 (b). The coercivity also showed overall increasing trend with decrease in <D> due to frustrated spins at the surface of NPs [133]. Table 4.1 shows the net magnetization and coercivity of different sized NiO nanoparticles dispersed in silica matrix.

Table. 4.1: Net magnetization and coercivity for different sized NiO nanoparticles.

Average crystallite size (nm)	Net magnetization M (emu/g)	Coercivity H_c (Oe)
14	1.6135	2423
16	0.7975	4012
18	0.674	1975
29	0.4475	2447
57	0.481	430

4.2.7 Optical Properties

The optical nature of the material is very important to investigate for different applications such as photocatalysis. Diffuse reflectance spectroscopy (DRS) technique was employed to analyze the absorption spectra of NiO/SiO_2(x) NPs with x = 0, 30, 50, 60 and 70%. The spectra were taken in the wavelength range of 250-1200 nm at room temperature. Fig. 4.7 shows the absorbance spectra of NiO/SiO_2(x) NPs with x = 0, 30, 50, 60 and 70% by using the K.M function. It is clear that higher absorption is observed in wide range of spectrum due to thick SiO_2 layer and is expected to perform higher photocatalytic activity.

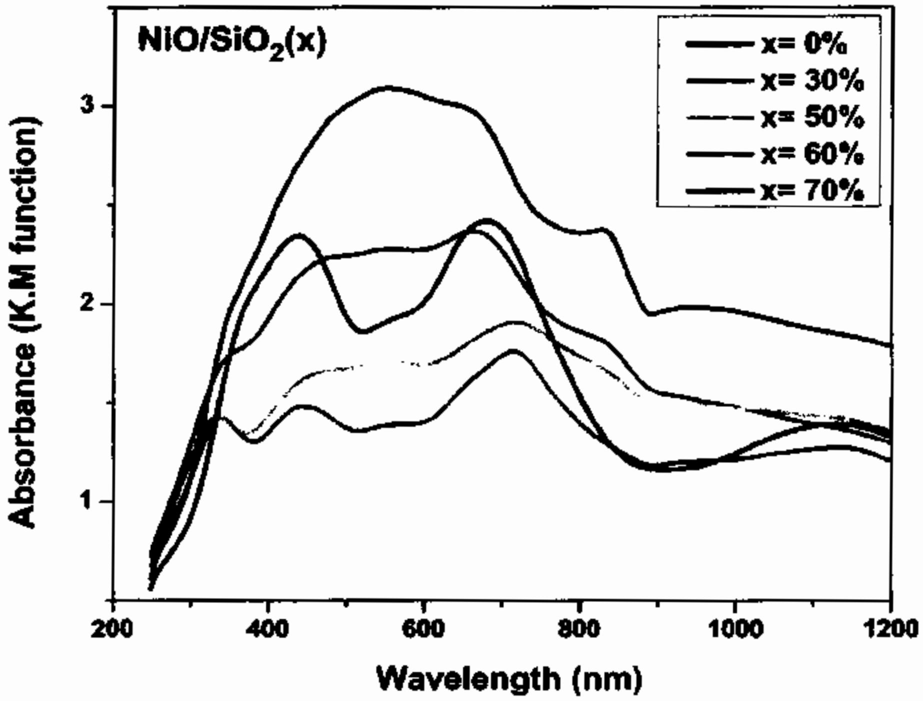

Figure 4.7: Absorbance spectra of NiO/SiO$_2$ (x) nanoparticles with x = 0, 30, 50, 60 and 70% by using Kubelka- Munk function.

The function F(R) is known as Kubelka-Munk (K.M) function [134-136].

$$F(R) = \frac{(1-R)^2}{2R} \tag{4.1}$$

Where R is the absolute reflectance and is found by dividing the percent reflectance of material to the reflectance of spectralon disk used as a reference. The function F(R) is equivalent to the absorption coefficient [137, 138].

4.2.8 Photocatalytic Activity

Methyl orange (MO) dye was to observe the photocatalytic activity of NiO/SiO$_2$(x) NPs with x = 0, 30, 50, 60 and 70%. The photo-degradation rate of MO dye molecules can be attributed to the efficiency of NiO/SiO$_2$ NPs being used as photocatalyst [139].

When ultra violet (UV) light (λ = 254 nm) is illuminated on the solution in the presence of catalyst, the absorbance peak gradually decreases with the irradiation time. The decreasing absorption peak and change in dye colour is attributed to the degradation of MO dye molecules and confirms the photocatalytic capability of NPs [140]. The photocatalytic degradation percentage can be calculated from the following equation [99].

$$\text{Degradation (\%)} = \left(\frac{A_o - A_t}{A_o}\right) \times 100 \tag{4.2}$$

Where A_o and A_t are the absorbance at 0 and t minute, respectively.

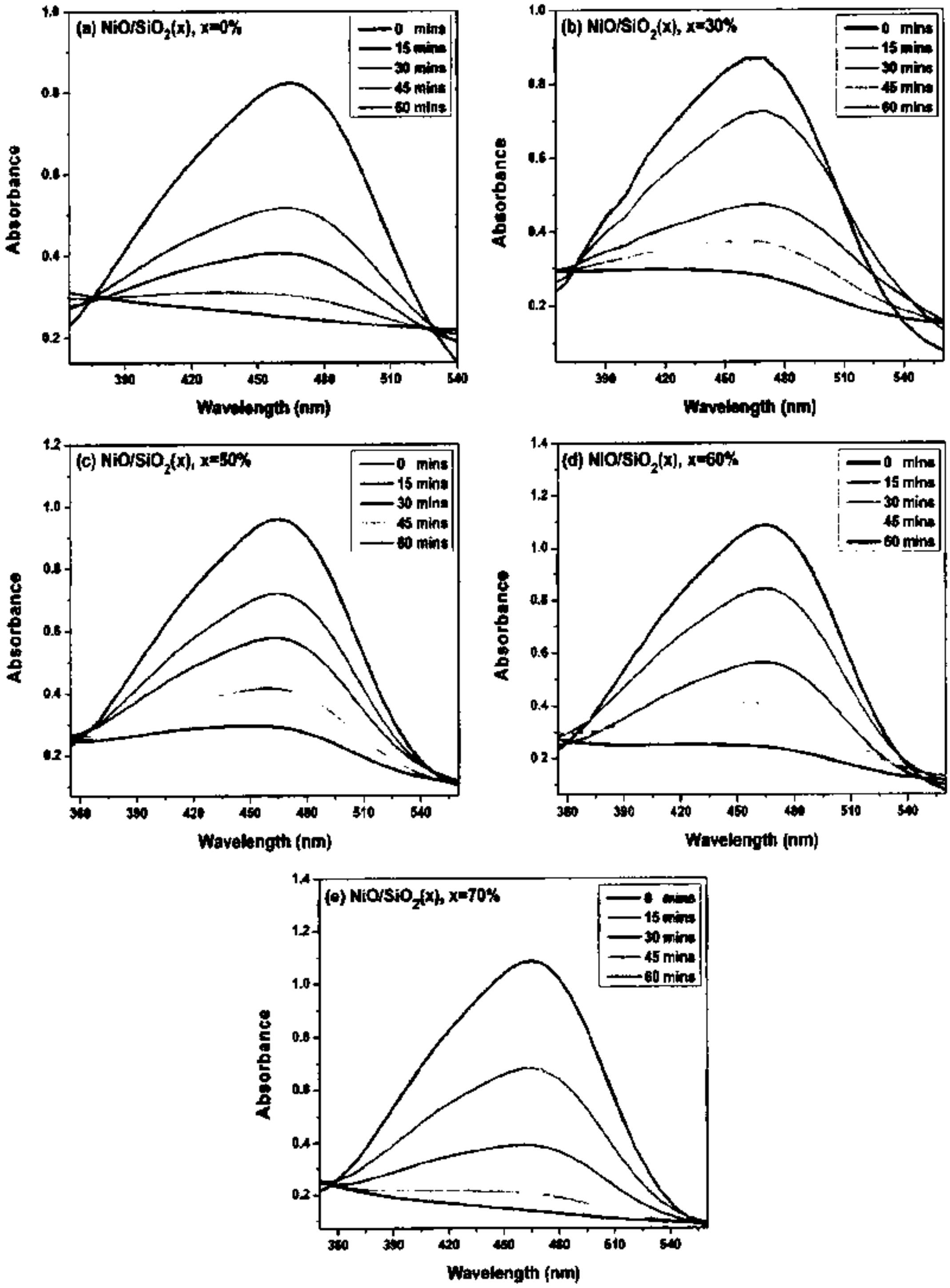

Figure 4.8: Absorbance spectra indicating the photocatalytic degradation of MO solution in the presence of NiO/SiO_2 (x) nanoparticles with (a) x = 0%, (b) x = 30%, (c) x = 50%, (d) x = 60% and (e) x = 70%.

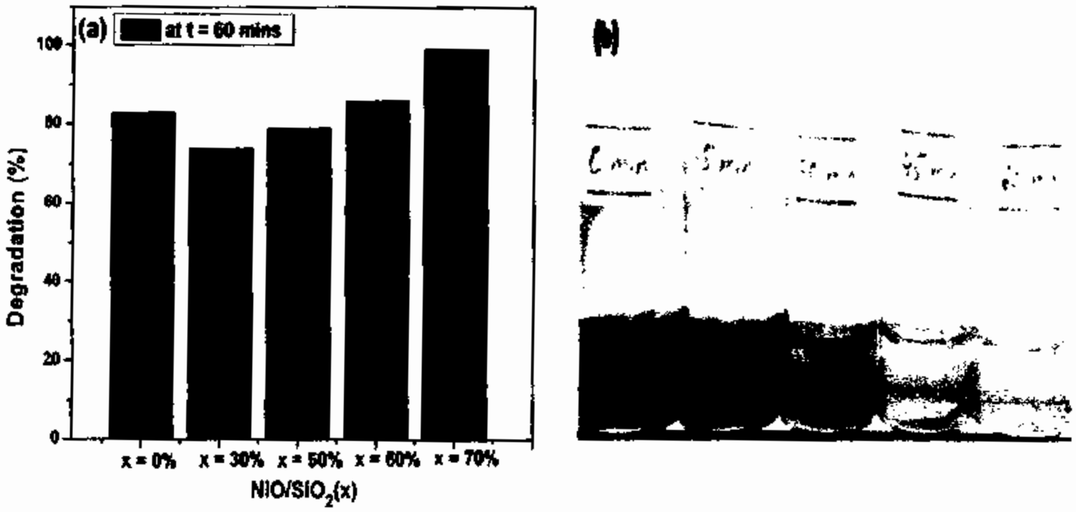

Figure 4.9: (a) Photocatalytic degradation % of MO in the presence of NiO/SiO_2 (x) with x = 0, 30, 50, 60, and 70% and (b) MO dye degradation for x = 70%.

Fig. 4.9 (a) shows the degradation percentage of MO dye in the presence of NiO/SiO_2(x) NPs with x = 0, 30, 50, 60 and 70% used as catalyst. Initially, the photocatalytic degradation efficiency decreased with SiO_2 concentration but then showed monotonous increasing trend with increasing SiO_2 concentration. Fig. 4.9 (b) shows the photo-degradation of MO in terms of change in colour. The MO solution gets transparent completely after 60 minutes of UV irradiation when x = 70% NPs used as catalyst which is also an indication of complete degradation of dye molecules.

Fig. 4.10 (a) and (b) show the TEM and HRTEM images of NiO NPs dispersed in SiO_2 matrix, at 100 and 20 nm, respectively. It is clear that NiO NPs are in well crystalline form whereas SiO_2 is in amorphous phase in accordance with XRD patterns. Fig. 4.10 (c) shows the interplaner distance (d_{hkl}) of 0.24 and 0.21 nm which correspond to (111) and (200) crystal planes of NiO NPs, respectively, in accordance with XRD. The left inset shows the fast Fourier transform (FFT) of the whole HRTEM image that is showing the orientation of the crystal planes growth and also confirming the presence of NiO planes.

Fig. 4.10 (d) shows the model diagram of NiO/SiO_2 structure for photocatalytic process. The amorphous SiO_2 is usually inactive as photocatalyst [141, 142] and has wide absorption spectrum in UV-Vis region (see Fig. 4.7) due to its porous nature [143-145]. Therefore, it can play the role as UV wave guiding medium to provide maximum absorbed energy to the NiO NPs to activate as photocatalyst. Lv *et al.* [146] reported the enhanced photocatalytic activity of TiO_2 and ZnO by the addition of fused SiO_2. It is also clear from 1LO mode of

Raman spectra that a small concentration of SiO_2 (x = 30%) reduces the surface defects and also the thin layer of SiO_2 was not sufficient to capture more light energy. Therefore, its photocatalytic activity is observed to be inferior to uncoated NiO NPs. However, on increasing the SiO_2 concentration, <D> starts decreasing thereby increasing the surface defects such as oxygen vacancies which may serve as charge carrier traps to suppress electron-hole recombination rate [147]. Tang *et al.* [148] reported the enhanced photocatalytic activity of ZnO NPs and attributed it to the generation of oxygen vacancies that worked as traps for photo-generated electrons.

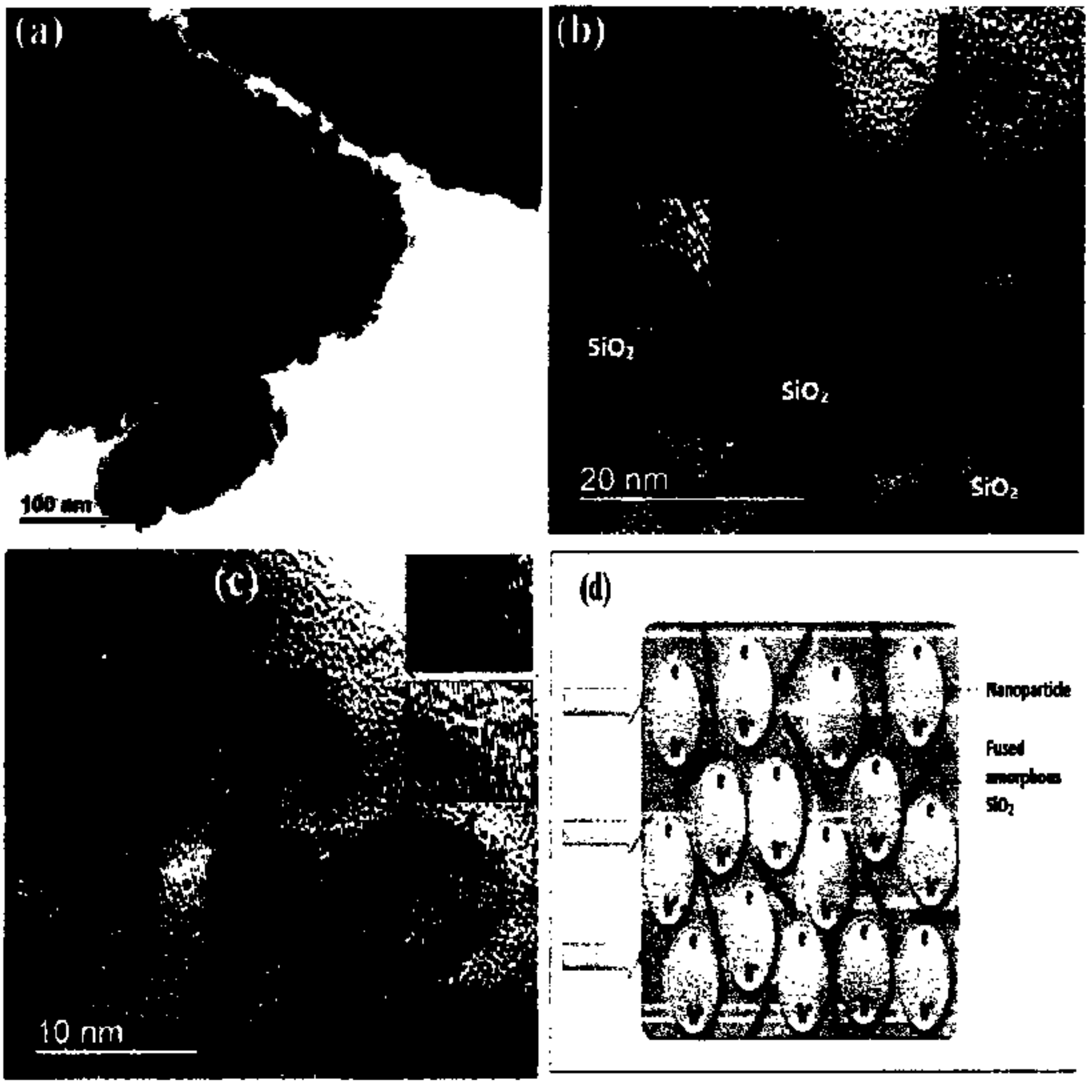

Figure 4.10: (a) TEM image at 100 nm scale, (b) HRTEM (insets with arrows show the crystalline NiO and amorphous SiO_2 phases) at 20 nm scale, (c) HRTEM at 10 nm scale indicating (111) and (200) planes of $NiO/SiO_2(x)$ nanoparticles with x = 60% (left inset shows the FFT image) and (d) model diagram of NiO/SiO_2 structure for photocatalysis.

The thick amorphous layer of SiO_2 is also grabbing more energy to provide to the NiO photocatalyst. Therefore, as a result, photocatalytic degradation performance shows increasing trend with increasing SiO_2 concentration. The exposed facets also have intriguing impact on the photocatalytic activity and researchers reported the effect of TiO_2 facets on its photocatalytic activity [149, 150]. However, in NiO/SiO_2 composite, detailed investigation is required to make a solid argument.

4.3 Unusual M-H Loop Splitting in SiO_2 Coated NiO Nanoparticles

Magnetic nanoparticles (NPs) exhibits features such as dangling bonds, large surface to volume ratio, surface defects and broken symmetry which can give rise to uncompensated spins at the surface. The net magnetization of AFM core can also be increased on reducing the size of NPs due to increased un-compensation of spins in the magnetic sublattices [68]. Montes *et al.* [54] attributed the net magnetic moment in AFM NPs to the collective blocking of both the uncompensated spins at the surface and to an imbalance of the two AFM sublattices in the core. Therefore, a net magnetic moment is observed in AFM NPs [133, 151] and they can behave as magnetically blocked (synonymous with ferromagnetic, in the following called FM) at the disordered surface, or as de-blocked superparamagnetic (SPM) spins in the core. In bulk form, NiO is an AFM material with a relatively high T_N=523 K [152]. However, T_N is reduced with decreasing particle size due to weak magnetic coupling in the core [69]. Tadic *et al.* [8] reported T_N=56 K for 5 nm NiO NPs dispersed in silica (SiO_2) matrix. For a critical particle size, a competition between blocked magnetic (FM) surface and AFM core spins appears that creates a bi-magnetic core/shell nanostructure. Neutron diffraction can be used to determine the AFM core diameter and the thickness of the spin glass shell [56]. The presence of a FM/AFM interface indicated the existence of an exchange bias between the core and the shell [153, 154]. The bi-magnetic core/shell nanostructure has some novel magnetic properties and is considered as a highly promising candidate for potential applications in spintronic and random access memory devices [57]. The core/shell structure is also particularly important to control the magnetic properties more easily such as tuning of the blocking temperature (T_B), coercivity (H_c) as well as other magnetic parameters. The temperature at which magnetic NPs become thermally unstable and the magnetization starts decreasing is known as SPM limit. To overcome the SPM limit, controlling the interaction between FM/AFM of the shell and the core is very important so that the magnetic properties can be stabilized under thermal influence. In AFM NPs, the shift of T_N closer to T_B can effectively enhance the SPM limit and also stabilize the transition of unblocked surface- as well as AFM core-spins toward the PM phase which is an interesting phenomenon to be investigated.

In this next section, the unusual intra-particle magnetic interactions and concomitant slow magnetic relaxation in 14 nm NiO NPs were studied by magnetization measurements, where the core and shell thickness was calculated by neutron diffraction experiment.

4.4 Results and Discussion

4.4.1 Transmission Electron Microscopy (TEM)

Fig. 4.11 (a) shows the TEM image at a 50 nm magnification and indicates the dispersion of 14 nm NiO NPs dispersed in 60 at.% SiO_2 matrix. The inset shows the histogram of the particle size distribution. The average particle size was found to be 14.8 nm which almost agrees with XRD. Fig. 4.11 (b) shows the SAED pattern of NiO NPs dispersed in SiO_2 matrix at 5/nm scale. The well-ordered white circles indicate the crystallinity of NiO NPs which correspond to the (111), (200), (220), (311) and (222) lattice planes of NiO. The radius of each circle depends on the d-spacing of the lattice planes of NiO NPs and the obtained d-spacing was found to be consistent with the results of XRD data. Fig. 4.11 (c) shows the HRTEM image of 14 nm NiO NPs dispersed in SiO_2 matrix at a 20 nm scale bar. The inset (i) shows the magnified image of inside NiO nanoparticle with a d-spacing of 0.21 nm for its (200) lattice plane. The inset (ii) shows the FFT diffraction spots which corresponds to the distance of 0.21 nm of the (200) lattice planes of NiO. Fig. 4.11 (d) shows the HRTEM image magnified in the inset (i) with d-spacing of 0.24 and 0.21 nm corresponding to its (111) and (200) lattice planes, respectively. The measured angle between the (111) and (200) planes was 54.7° and found in perfect agreement with the theoretically calculated angle of 54.736° between these two planes. The inset (ii) Fig. 4.11 (d) shows two types of spots with radial distance of 0.24 and 0.21 nm representing the (111) and (200) planes, respectively. The measured angle between the orientation vectors of the two planes was also found to be 54.7° which further confirms the assignment to the (111) and (200) planes in accordance with XRD results.

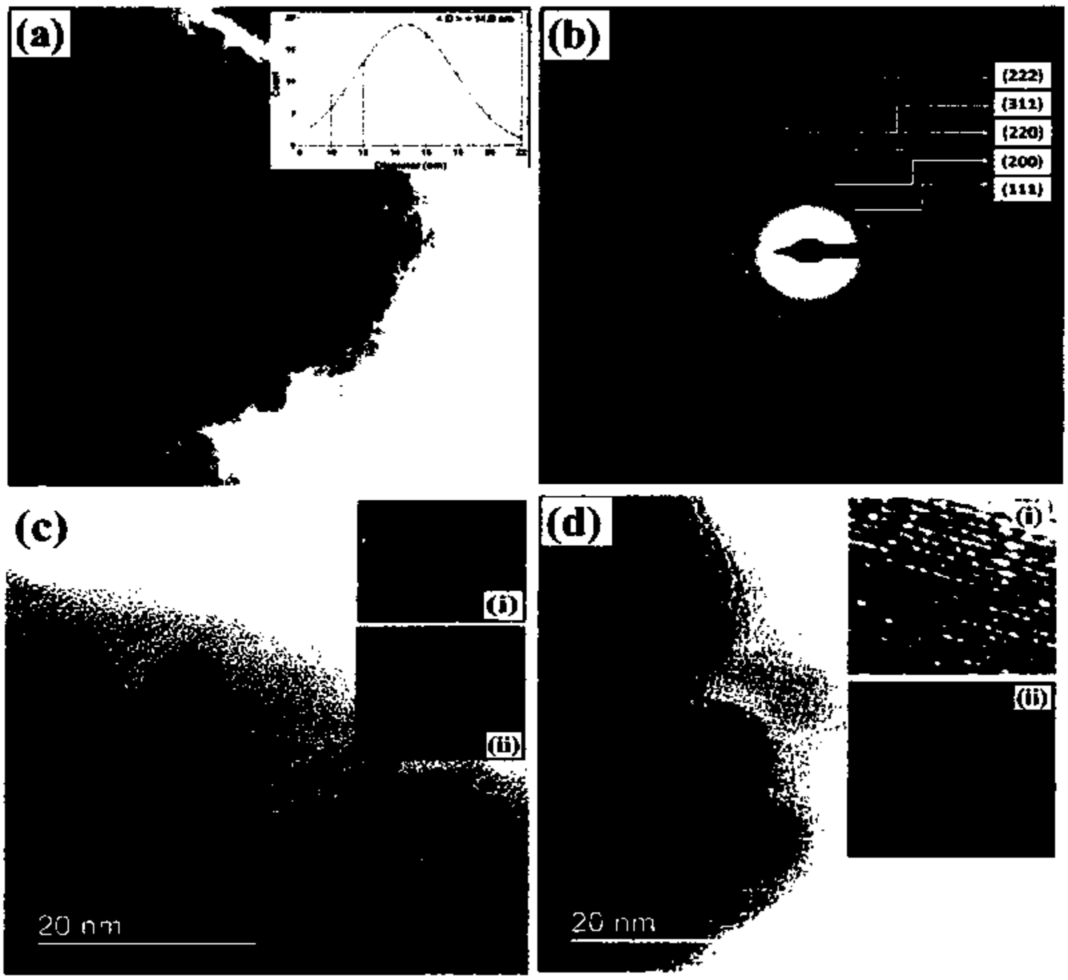

Figure 4.11: (a) TEM image of 14 nm NiO nanoparticles dispersed in 60 % SiO_2 matrix. The inset shows the particle size distribution, (b) SAED pattern indicating crystal planes of NiO nanoparticles, (c) HRTEM at 20 nm magnification Inset (i) shows magnified image of inside NiO nanoparticles and Inset (ii) shows the FFT diffraction images of the (200) lattice plane of NiO nanoparticles and (d) HRTEM image at 20 nm magnification, where inset (i) shows magnified image of inside NiO nanoparticles and (ii) shows FFT diffraction images with the (111) and (200) lattice planes of the NiO nanoparticles.

4.4.2 Zero Field Cooled (ZFC)/Field Cooled (FC) Magnetization under Different DC Magnetic Fields

In order to determine the temperature dependence of the magnetization, magnetization curves were taken in ZFC-FC condition at different applied magnetic fields as shown by the Fig. 4.12 (a-f).

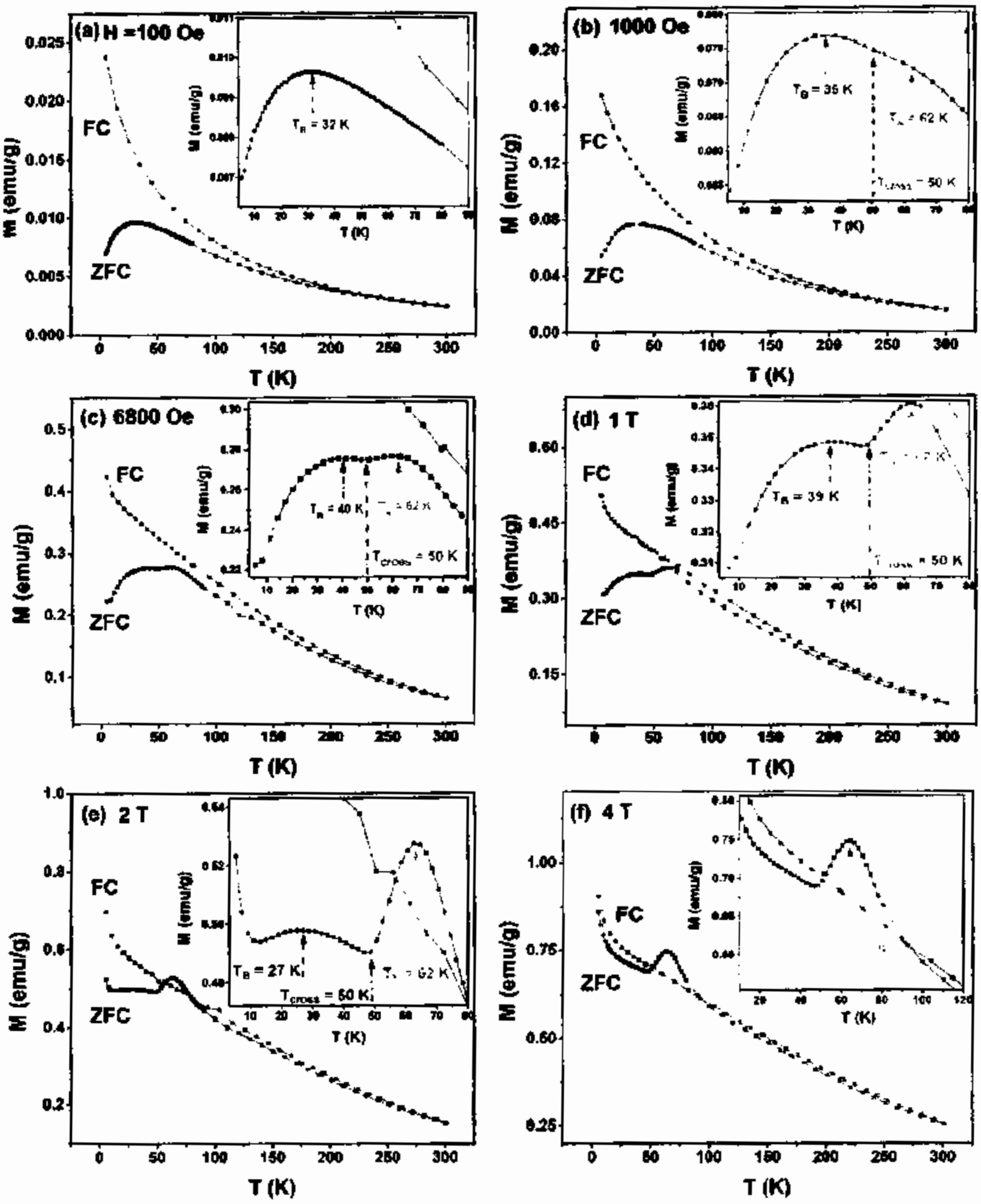

Figure 4.12: ZFC-FC magnetization scans vs. temperature of 14nm NiO nanoparticles with applied magnetic field of (a) 100 Oe, (b) 1000 Oe, (c) 6800 Oe, (d) 1 T, (e) 2 T and (f) 4 T. Insets show the section of crossover region.

The blocking peak T_B usually decreases with increasing field due to reduction of the energy barrier between the opposite easy axis orientations and finally disappears for a critical high value of the magnetic field [155]. However, in our case the T_B initially increases and then decreases with increasing applied magnetic field. Therefore, it can be inferred that the energy barrier increases and then decreases with increasing applied magnetic field. Tedaja *et al.* [156] observed the same increasing and then decreasing trend of T_B in ferritin with increasing applied magnetic field and attributed it to a resonant tunneling of magnetization. The second peak at 62 K, which can be attributed to the Néel temperature (T_N), becomes pronounced with increasing field. However, this peak was found to be field independent and it is much lower value than bulk (523 K) which indicates the presence of surface/core defects and weak exchange interactions in the small-sized NiO NPs lead to the reduction of the magnetic phase transition temperature. Thota *et al.* [28] observed a sharp decrease in T_N with decreasing NiO nanoparticle size. It can be seen from the inset of Fig. 4.12 (b-e) that 50 K is the cross-over temperature (T_{cross}) where both the SPM blocking and Néel transition states are present. However, above 6800 Oe field (see Fig. 4.12 (d-f)), the T_N peak becomes more prominent and increases further with increasing field. Interestingly, for magnetic fields above 2 T, the magnetization of T_N peak gets higher than the FC curve (see Fig. 4.12 (e) and (f)) which can be explained with the dominancy of core uncompensated spins at high field. It is in agreement with the findings of Tadic *et al.* [8], who also observed such a behavior in NiO/SiO_2 NPs.

4.4.3 M-H Loops

In order to further investigate the two competing modes of the SPM blocking and Néel transition state at T_{cross} = 50 K, a M-H loop was taken at 50 K. Usually, antiferromagnetic materials have no H_c and the M-H loop has an almost linear shape. However, with decreasing crystallite size to a critical level, H_c increases due to increasing surface disorder [157]. In our case, the non-linear M-H loop and presence of H_c indicates the blocked SPM nature of these NPs due to the uncompensated spins in the surface and core.

The non-saturation of magnetization in M-H loops indicate the strong magnetic interactions present for the uncompensated spins of the surface and the core. Interestingly, quite unusual splitting/crossover of the magnetization curves upon field reversal (~6800 Oe) was observed as shown in the inset of Fig. 4.13 (a).

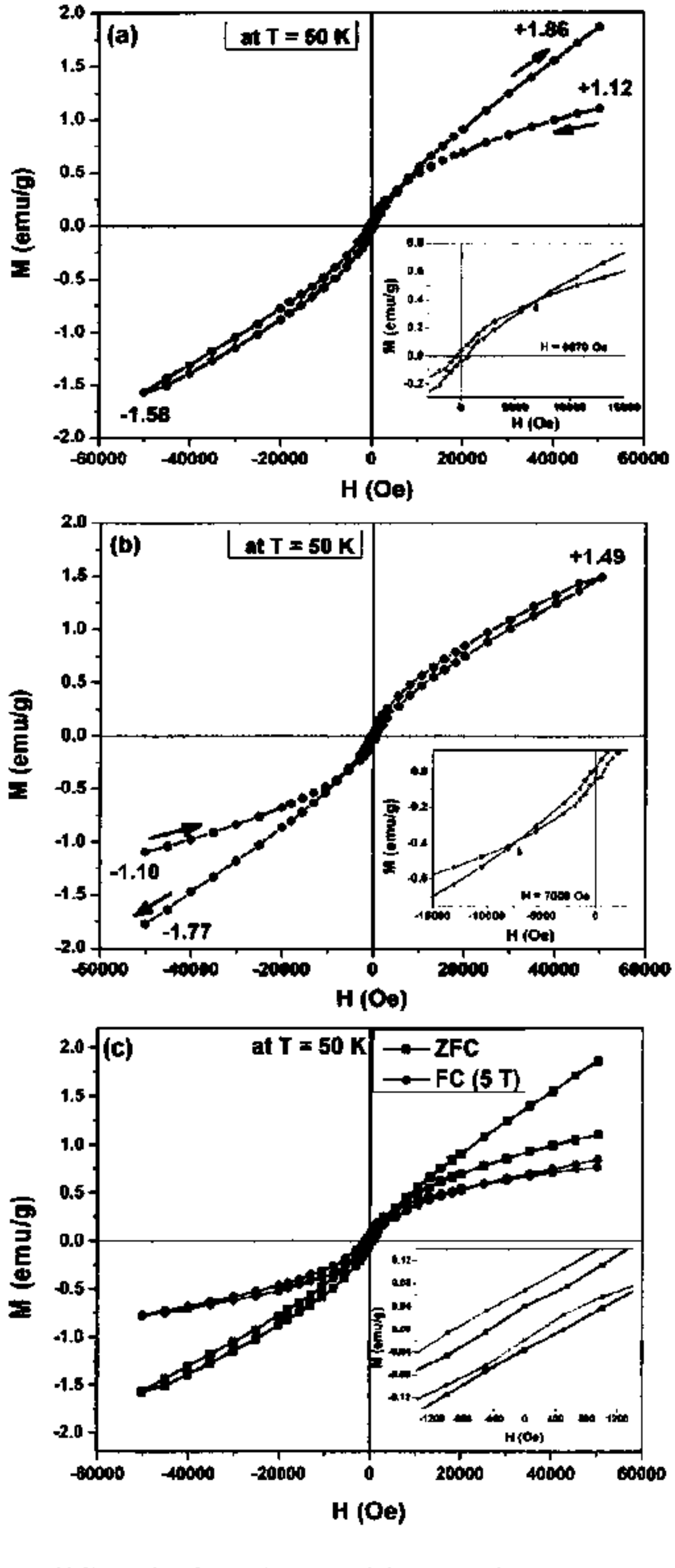

Figure 4.13: M-H loops at 50 K starting from (a) +5 T and (b) -5 T and (c) ZFC and FC (5 T) M-H loops at 50 K for 14 nm NiO nanoparticles.

The magnetization is increased from 1.12 to 1.86 emu/g upon field reversal and a large difference in magnetization (Δm=0.74 emu/g) was observed. More interestingly, the magnetization becomes higher for increasing fields at ~6800 Oe, which is the field after which the contribution from the uncompensated spins of the core becomes prominent in accordance with the ZFC-FC magnetization curves in Fig. 4.12 (c-f). In order to rule out the experimental error, a reverse M-H loop was also taken by starting the field from the opposite direction, i.e. at -5T and the same behavior was observed in the opposite quadrant with almost same crossover field and coercivity (H_C) as indicated in Fig. 4.13 (b).

For the confirmation of core-shell interactions and exchange bias phenomena, M-H loops were taken at 50 K under ZFC and FC (@ 5 T) protocols as shown in Fig. 4.13 (c). The ZFC loop was found to be symmetric around the origin whereas the FC loop showed a vertical and horizontal displacement from the origin known as exchange bias (EB). The EB effect appears due to the spin pinning mechanism at FM/AFM interface, i.e. the interface between the core and the surface shell [158]. When the AFM material is cooled down to T_N in a static magnetic field, the net magnetic moment from the uncompensated spins of the surface shell get coupled with the AFM spins of the core. This causes the displacement of the M-H loop which is denoted by the exchange bias field (H_{EB}) [159]. The H_{EB} was found to be 352 Oe and is generally defined as $H_{EB} = -\frac{(H_1-H_2)}{2}$. An enhancement of coercivity $\Delta H_C = 465\ Oe$ was also observed in FC process using the relation $\Delta H_C = H_C(FC) - H_C(ZFC)$. Additionally, a vertical shift at H=0 was also observed and found to be $M_{shift} \approx 0.029\ emu/g$. Therefore, it can be concluded that an exchange coupling is present at 50 K due to the interaction between compensated core and uncompensated surface spins.

4.4.4 M-H Loop Splitting at Different Temperatures

In order to get a deeper insight to the M-H loop splitting/crossover behavior, M-H loops of 14 nm NiO NPs were taken at different temperatures (25, 45, 50, 55, 75 and 100 K) as shown in Fig. 4.14. At 50 K, the splitting behavior reaches a sharp maximum. The splitting behavior at 25 K nearly vanished which may be due to the weak interaction between SPM blocking and Néel transition state. It is due to the fact that surface spins are in a blocked state and the core spins are biased by the AFM alignment due to decreased thermal fluctuations.

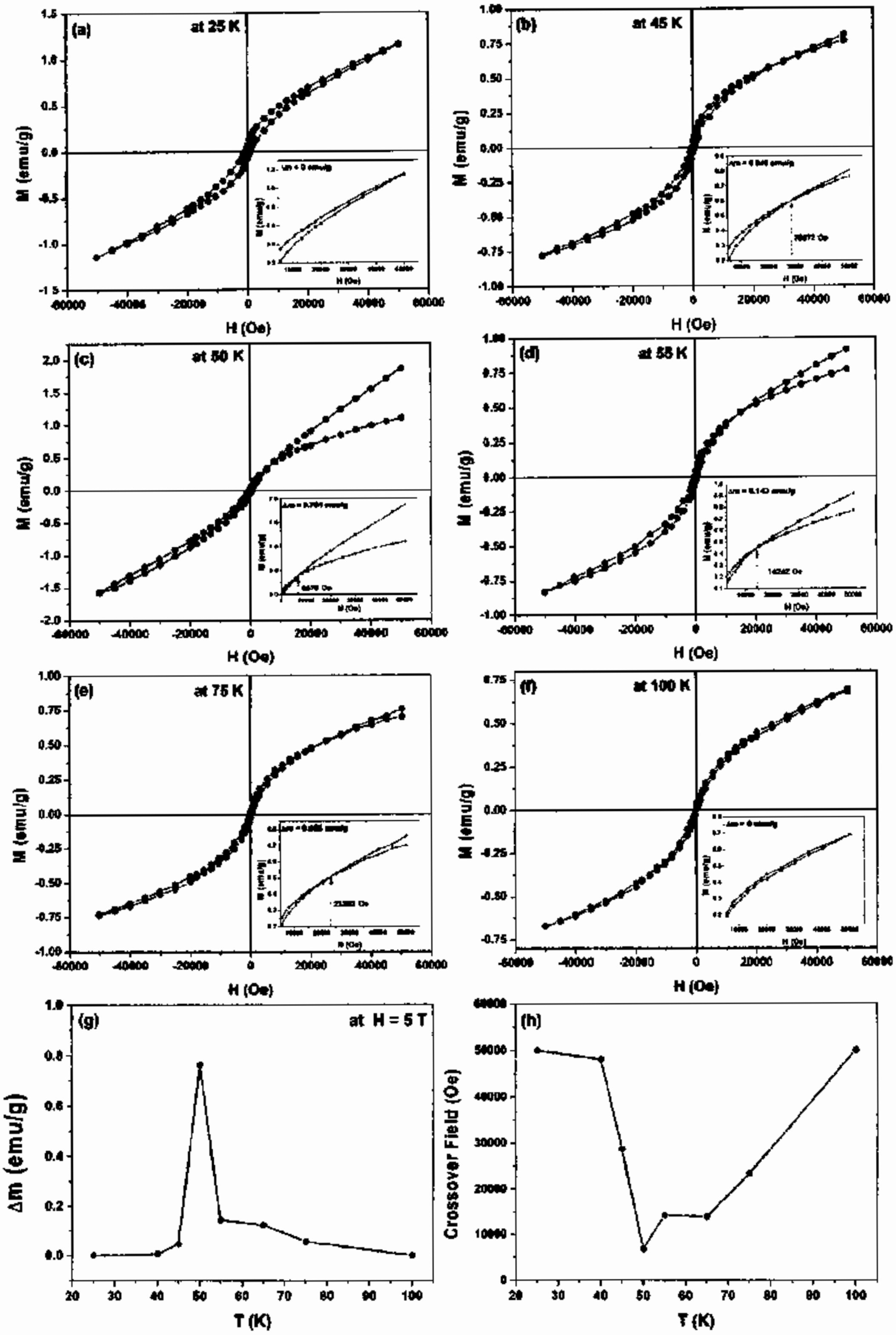

Figure 4.14: (a-f) M-H loops for 14 nm NiO nanoparticles taken at temperatures of 25, 45, 50, 55, 75 and 100 K, (g) difference in magnetization with temperature after field reversal with a prominent peak at T_{cross} and (h) crossover field at different temperatures.

This splitting behavior becomes weak above 50 K [*see* Fig. 4.14 (d-f)] and vanishes at 100 K due to the fact that surface spins are thermally fluctuating (SPM state) and the core is nearly paramagnetic, in accordance with the coincidence of ZFC-FC curves in Fig. 4.11. The change in magnetization (Δm) possesses a maximum at 50 K and the crossover/splitting field was found to be rather low (6800 Oe) which indicates the presence of a slow magnetic relaxation at this particular temperature, see Fig. 4.14 (g) and (h), respectively.

4.4.5 Field Cooled Relaxation

The magnetic relaxation is a time dependent phenomenon, where the magnetization either increases or decreases with time and it gives the information about intra-particle magnetic interactions. In order to observe the magnetic relaxation phenomenon, the field cooled (FC) magnetization was measured as a function of time at selected temperatures, i.e. at 25, 50 and 100 K as shown in Fig. 4.15 (a-c).

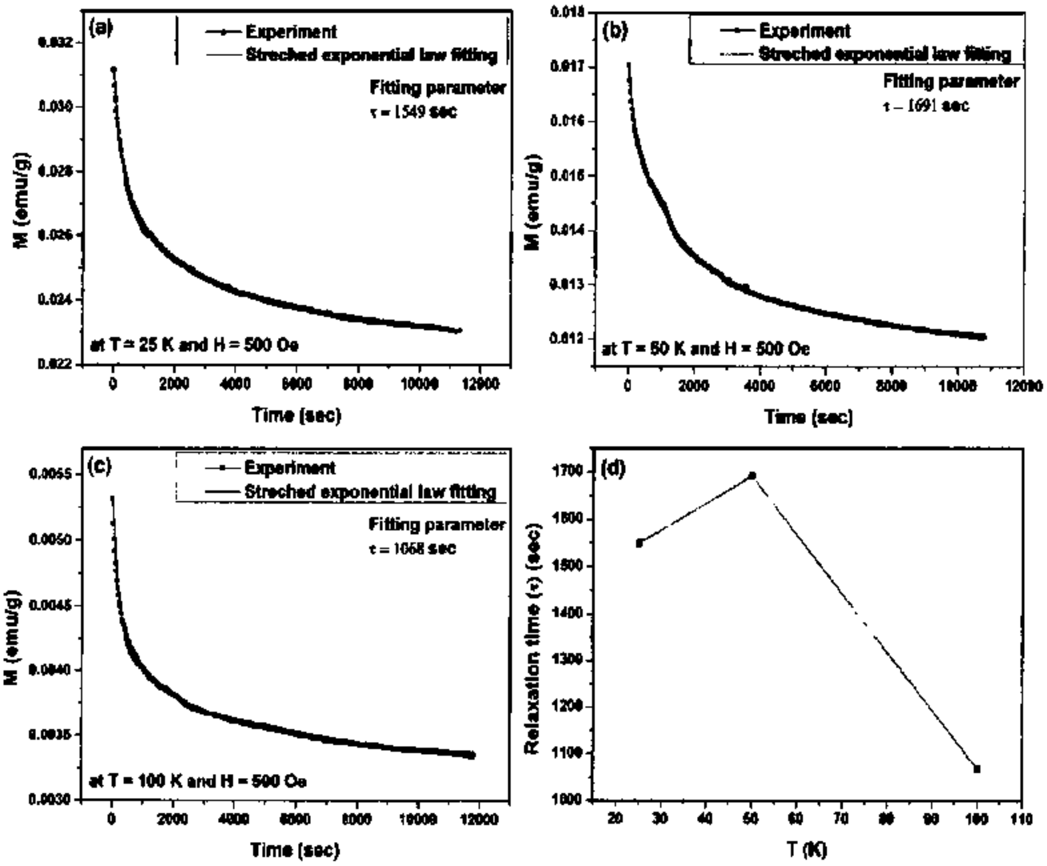

Figure 4.15: Field cooled relaxation of the 14 nm NiO nanoparticles at (a) 25 K, (b) 50 K, and (c) 100 K. (d) variation of the relaxation time with temperature.

The sample was first field cooled from room temperature to a desired temperature in the presence of 500 Oe. Then, after the field was switched off and the magnetization was measured as a function of time. For the analysis a stretched exponential law was fitted to the data [160]

$$M(t) = M_2 + (M_1 - M_2)e^{-(t/\tau)^{\beta}} , \tag{4.3}$$

where M_1 and M_2 are the steady state initial and final magnetizations, respectively. β is the stretching parameter and τ is the mean relaxation time of magnetic spins. Usually, the mean relaxation time (τ) decreases with increase in temperature [161]. However in our case, a maximum appears at 50 K as shown in Fig. 4.15 (d). The increased mean relaxation time at 50 K is an indication of the presence of slow spin relaxations at this temperature. At 50 K, the disordered frozen surface spins are getting de-blocked and at the same time the AFM core spins are transforming to PM. Hence, not all the spins were able follow the field during this transition phase, represented by a higher magnetic viscosity. Therefore, the magnetic spins are slowly following the applied magnetic field and the net magnetization becomes increased by taking enough time upon field reversal in Fig. 4.13 (a) and (b).

4.4.6 Magnetic Field Switching

To demonstrate the increase of magnetic viscosity and relaxation time, the magnetic field was switched alternately between +5T and -5T and the magnetization was observed as a function of time for 25, 50 and 100 K as shown in Fig. 4.16 (a-c). At 25 K, no amplitude variation of the net magnetization is observed from the AFM core and blocked surface spins which confirms the weakening or even absence of magnetic interactions causing fast (instantaneous) magnetic relaxation upon field reversal in M-H loop. However, quite unusually, the net magnetization started to increase with accumulation of field reversal periods at 50 K which confirms the slow spin relaxation at this temperature due to the competing interaction of SPM blocking and Néel transition state in accordance with the slow relaxation found in the FC protocol for 50 K in Fig. 4.15 (b). At 100 K, the magnetization decreases with time due to thermal fluctuations, a common phenomenon also observed in several systems such as in magnetite NPs [162-164].

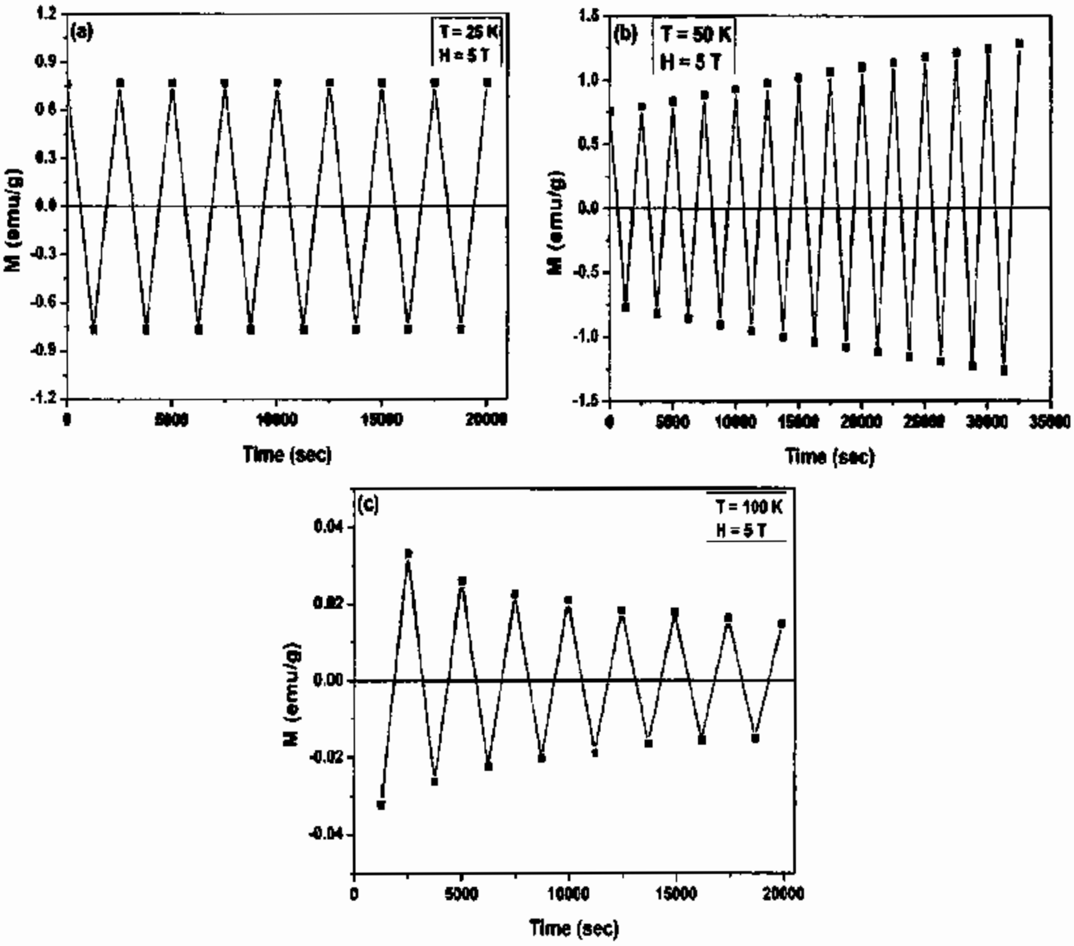

Figure 4.16: Magnetization versus time at field switching between +5T and -5T at temperatures of (a) 25 K, (b) 50 K and (c) 100 K measured on 14 nm NiO nanoparticles.

4.4.7 Particle Size Dependence of M-H loop Splitting Behavior

In order to determine the particle size dependence of the M-H loop splitting behavior, one more sample with 80 at.% of silica concentration was synthesized and the <D> was obtained as 8 nm. Fig. 4.17 (a-e) shows the M-H loops of different <D> (8, 14, 16, 18 and 29 nm) of NiO NPs at 50 K. No splitting appears for the particles with <D> = 8 nm. This may be due to the small AFM core volume compared to the large surface area.

Therefore, the surface shell dominates and the interfacial magnetic interactions might be negligible. Similarly, for the sample with <D> = 29 nm, the smaller surface-to-core ratio hinders such core-shell magnetic interactions. However, the cross-over behavior was found to be most prominent for sample with a <D> = 14 nm where the core and surface size effect compete with each other, while they are getting suppressed with increasing or decreasing crystallite size. Fig. 4.17 (f) shows that, for a critical size of 14 nm NiO NPs, the lowest crossover field and the highest Δm is observed. This demonstrates that the coupling is size-dependent and dominates in the temperature range between T_B and T_N.

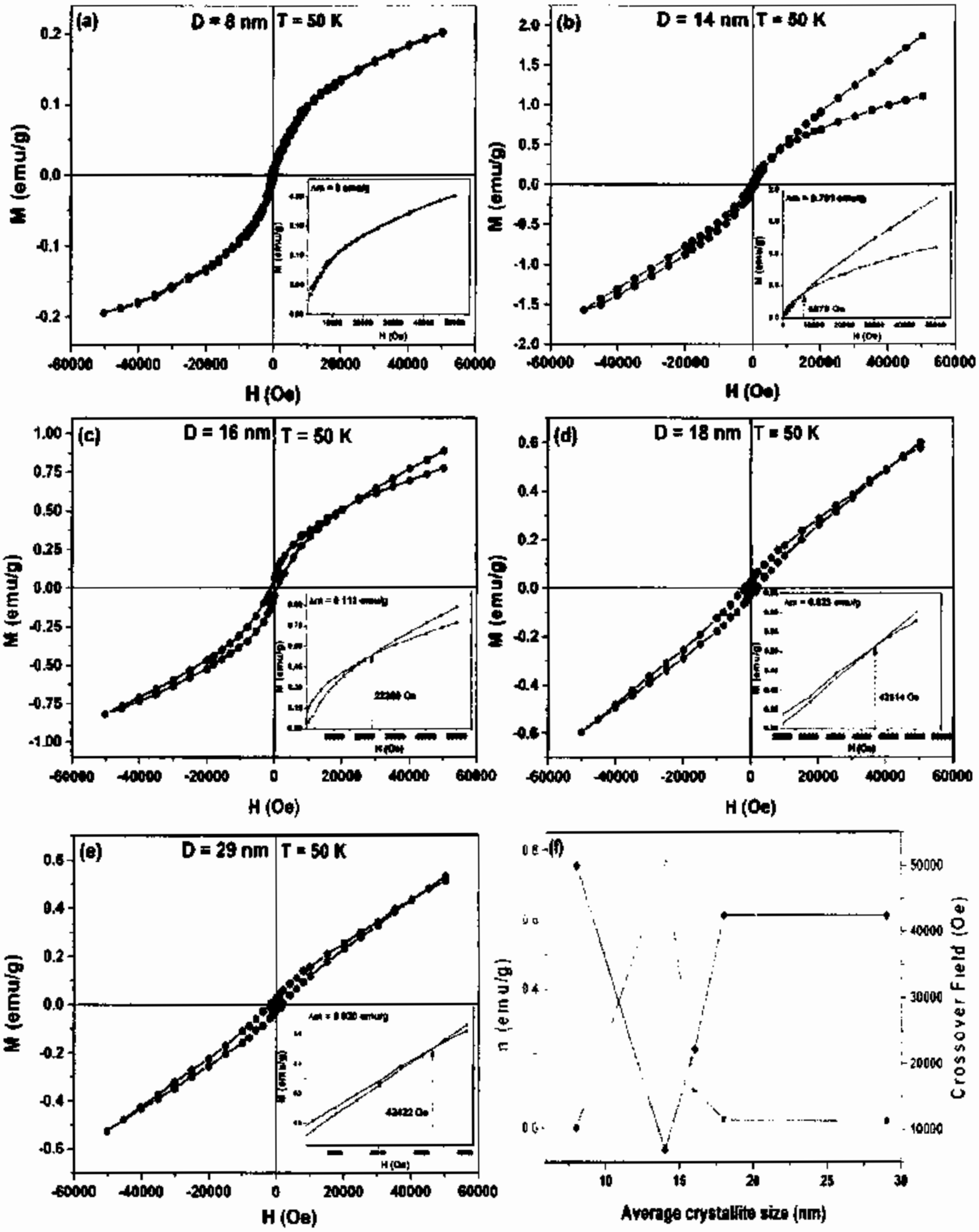

Figure 4.17: M-H loops (@ T = 50 K) of NiO nanoparticles with different <D> (a) 8 nm, (b) 14 nm, (c) 16 nm, (d) 18 nm, (e) 29 nm, and (f) shows the <D> vs change in magnetization and crossover field.

4.4.8 Neutron Diffraction

For the determination of the thickness of the AFM core and spin-glass shell, neutron diffraction patterns were measured at 4 K for three selected different sized (8, 14 and 29 nm, determined by XRD) NiO NPs as shown in Fig. 4.18 (a-c).

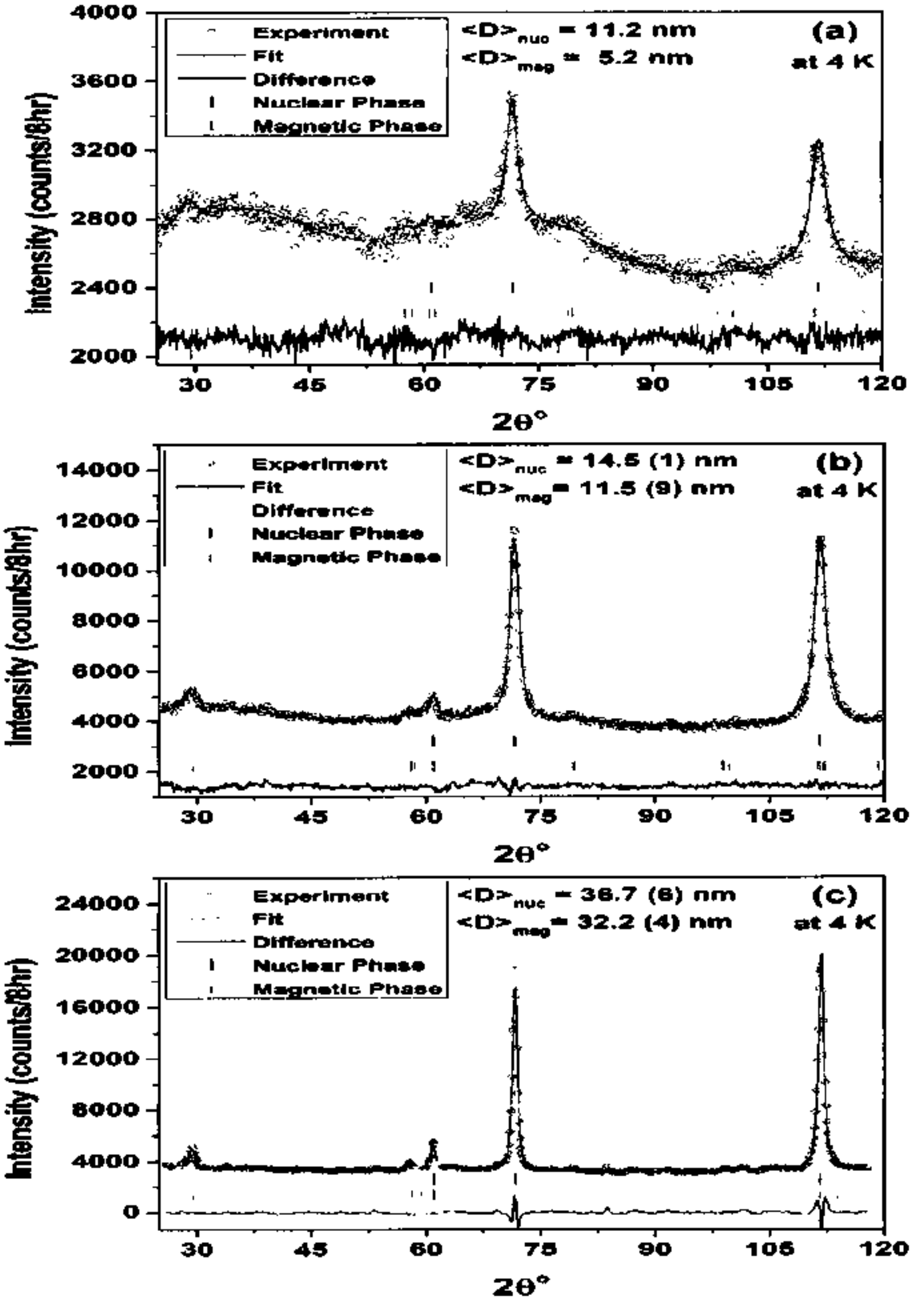

Figure 4.18: Neutron diffraction pattern taken at a temperature of 4 K for samples with <D> (a) 11.2 nm, (b) 14.5 nm, and (c) 36.7 nm. The red solid lines are the results of Rietveld refinements to the experimental data and the blue lines are the difference between the results of the fits and the experimental data. The vertical green and purple lines indicate the position of the nuclear and magnetic Bragg peaks, respectively.

The structural and magnetic phase refinement was performed by using the GSAS-II package based on the Rietveld refinement method [165]. The nuclear and magnetic peaks observed were consistent with the previously-determined NiO nuclear and magnetic structure [56, 166, 167]. The magnetic refinement of the neutron diffraction patterns of NiO corroborates the two magnetic sub-lattices with Ni spins oriented within the (111) planes and the adjacent sublattice anti-parallel to it [69]. The peak at $2\theta=\sim 29^\circ$ corresponds to the $(\frac{1}{2}\,\frac{1}{2}\,\frac{1}{2})$ magnetic reflection from the AFM coupled (111) planes [167]. The magnetic subspace group was observed to be C2/n, and derived that each Ni spin is surrounded by 12 nearest neighbours with 6 Ni spins in FM orientation sitting on the (111) plane and in AFM interaction on the other 6. This large AFM exchange interaction between next nearest neighbours is the origin of high T_N for NiO as compared to other AFM transition metal monoxides [168].

The primary purpose of conducting neutron diffraction at low temperature (4 K) was to observe the nuclear and magnetic diameters of the core and the shell of the NiO NPs for the different sized crystallites. Both the nuclear (D_{nuc}) and magnetic (D_{mag}) clusters diameter were determined from the broadening of the magnetic and nuclear reflections, respectively. For all samples, D_{mag} turns out to be smaller than D_{nuc} due to spin disorder at the surface. However, D_{nuc} is almost consistent with XRD and TEM results. As also observed previously, the thickness of magnetically disordered shell is greater than the nuclear disorder [169]. Therefore, we conclude that the AFM order is suppressed in a large fraction of the particle volume. The obtained average nuclear diameters $\langle D_{nuc}\rangle$ were 11.2, 14.5 (1) and 36.7 (6) nm while the average magnetic diameter $\langle D_{mag}\rangle$ were 5.2, 11.5 (9) and 32.2 (4) nm, respectively. This is shown in Fig. 4.19. The average crystallite size calculated from XRD and ND is shown in Table 4.2.

Table. 4.2: Average crystallite size calculated from XRD and ND.

Sample	$\langle D\rangle_{nuc}$ nm from XRD	$\langle D\rangle_{nuc}$ nm from ND
1	8	11.2
2	14	14.5 (1)
3	29	36.7 (6)

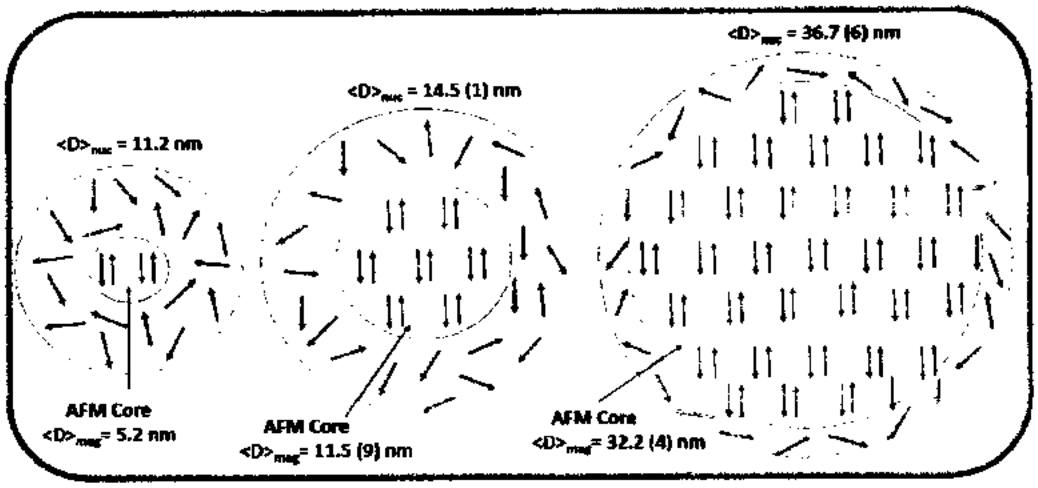

Figure 4.19: Schematic presentation of the core/shell thicknesses as determined by neutron diffraction for different sized NiO nanoparticles.

The volume ratio for spin-glass shell to AFM core (V_{shell}/V_{core}) was found to be 2.08, 0.99, and 0.11 for the 11.2, 14.5 and 36.7 nm NPs, respectively. For the 14.5 nm NPs the ratio V_{shell}/V_{core} is almost 1 which indicates that disordered shell and AFM core have almost same volume for this critical size. Therefore, it can be concluded that the SPM disordered surface and AFM core compete in such a way that a slow spin relaxation is induced. This can be considered as the main reason behind the M-H loop splitting/cross-over behaviour.

4.5 Conclusions

$NiO/SiO_2(x)$ NPs with x = 0, 30, 50, 60 and 70% have been synthesized via sol-gel method. The average crystallite size get decreased from 57 to 14 nm with increasing SiO_2 concentration. The increasing intensity of 1LO mode and diminishing 2M band with increasing SiO_2 concentration is attributed to generation of defects and achieving SPM in these NiO NPs. The ZFC/FC and M-H loops also confirmed the transition from AFM to SPM state. The strong association was found between magnetization data and Raman 2M behaviour of NiO/SiO_2 NPs. The absorbance spectra from DRS revealed that $NiO/SiO_2(x)$ NPs with x=70% has higher and wide absorption range in comparison to other samples which gave strong indication for enhanced photocatalytic activity. In photocatalytic experiment, $NiO/SiO_2(x)$ NPs with x = 70% performed highest degradation of MO dye due to the presence of surface defects that behave as traps for photo-generated electrons in NiO NPs. The amorphous SiO_2 behaved as wave guiding medium to provide maximum

UV energy to the NiO NPs. The HRTEM images supported the proposed process model that clearly showed the crystalline NiO NPs dispersed in amorphous SiO_2 matrix.

The detailed magnetic properties of smallest obtained <D> = 14 nm of NiO NPs were studied. The competing magnetic interaction between superparamagnetic blocking and Néel transition state were observed for this critical size (14 nm). The ZFC-FC magnetization curves at different fields showed a crossover temperature of 50 K for both these states. A prominent M-H loop splitting was observed at this temperature due to presence of slow spin magnetic relaxation confirmed by FC relaxation experiment. M-H loop splitting get suppressed above and below 50 K due to weak interaction of superparamagnetic blocking and Néel transition state. This anomalous M-H loop splitting behaviour was found to be particle size dependent and suppressed for diameters above and below 14 nm. The neutron diffraction patterns at 4 K confirmed that the spin-glass shell and AFM core volume fraction (V_{shell}/V_{core}) is $0.99 \approx 1$, for this critical size and there is a competition between the spin glass surface and the AFM core. It reaches a maximum for 14 nm and can therefore be accounted for the slower spin relaxation and as the reason for the M-H loop cross-over phenomenon. The obtained results are important step towards a deeper understanding of intra-particle magnetic interaction of SPM blocked and Néel transition state. SiO_2 may also have an impact on the surface disorder which was reported for nickel ferrite NPs in our previous study [170].

CHAPTER NO. 5

Effect of Doping on Optical and Magnetic Properties of NiO Nanoparticles

In this chapter, effect of single Fe doping concentration on optical and magnetic properties of NiO nanoparticles has been studied. Then, effect of Fe-Mn co-doping with equal and different doping concentration on magnetic properties of NiO nanoparticles have been studied.

5.1 Photocatalytic Activity of Ferromagnetic Fe-doped NiO Nanoparticles

The most extensive method to fabricate the nanoparticles (NPs) for desired application is to dope by ions of foreign element. The suitable dopant not only breaks the crystal symmetry and produces strain in the structure but may also disrupt the magnetic nature of the NPs. The presence of two-magnon (2M) band ~1500 cm^{-1} in Raman spectra reveal the AFM nature of bulk NiO. Mironova *et al.* [119] observed 2M peak for larger sized NiO NPs and confirmed its AFM nature by magnetic measurements also. Similarly, the absence of 2M peak can be attributed to the superparamagnetic (SPM) nature of NPs. Liu *et al.* [171] reported the disappearance of 2M peak in NiO nanocrystals due to size reduction and attributed to broken symmetry of AFM. The room temperature ferromagnetism (RTFM) in NiO NPs can be achieved by incorporation of suitable metal ions [40]. Lin *et al.* [172] reported RTFM in NiO NPs with Fe doping and ascribed to double exchange mechanism. The localized energy states generated in the host material by dopant can also have great impact on optical nature of the material. Patel *et al.* [173] observed increased optical E_g in Fe doped NiO NPs and attributed it to quantum confinement effect. Among different metal oxides, NiO NPs are reported as efficient photocatalyst [101, 140, 174] due to their higher degradation rate, better chemical stability, presence of oxygen vacancies, non-toxicity and relatively low cost of production. In order to improve the photocatalytic ability of NiO NPs, the incorporation of suitable metal ions can possibly generate oxygen vacancies that slows down the electron-hole recombination rate. The oxygen vacancies serve as charge carrier traps for electrons and is vital for photocatalytic process. Sankar *et al.* [175] reported the improved photocatalytic degradation performance of Mn doped NiO NPs and attributed it to generation of localized electronic states which possibly served as charge carrier traps. Therefore, it would be beneficial to investigate the photocatalytic ability of Fe doped NiO NPs that will be collected easily for reuse due to their magnetic nature and are not found to be reported in literature.

5.2 Results and Discussion

The samples with Fe doping concentration 0, 2, 4, 6 and 8 at.% in NiO were labelled as NF0, NF2, NF4, NF6 and NF8.

5.2.1 X-ray Diffraction (XRD) and Fourier Transform Infrared Spectroscopy (FTIR)

Fig. 5.1 (a) and (b) shows the XRD patterns and FTIR spectra of NF0, NF2, NF4, NF6 and NF8 NPs. The diffraction peaks at 37.12°, 43.14°, 62.72°, 75.12° and 79.18° correspond to (111), (200), (220), (311) and (222) planes of FCC structure of NiO, respectively. The obtained pattern was found in accordance with the standard pattern of NiO (JCPDS No. 01-073-1523). The ferromagnetic Ni phase was not observed which is most probable impurity phase observed at low temperature [65]. The other possible impurity phases, like $NiFe_2O_4$, Fe_2O_3 and Fe_3O_4 which have magnetic origin were also found absent.

The average crystallite size (<D>) was found to be 33, 32, 31, 29 and 30 nm for NF0, NF2, NF4, NF6 and NF8 NPs, respectively. No shift in the peak position has been observed which confirmed that doping did not produced any strain in the NiO structure. In FTIR spectroscopy, a dominant dip in the range of 417-432 cm^{-1} is consigned to stretching vibration mode of Ni-O molecule [114].

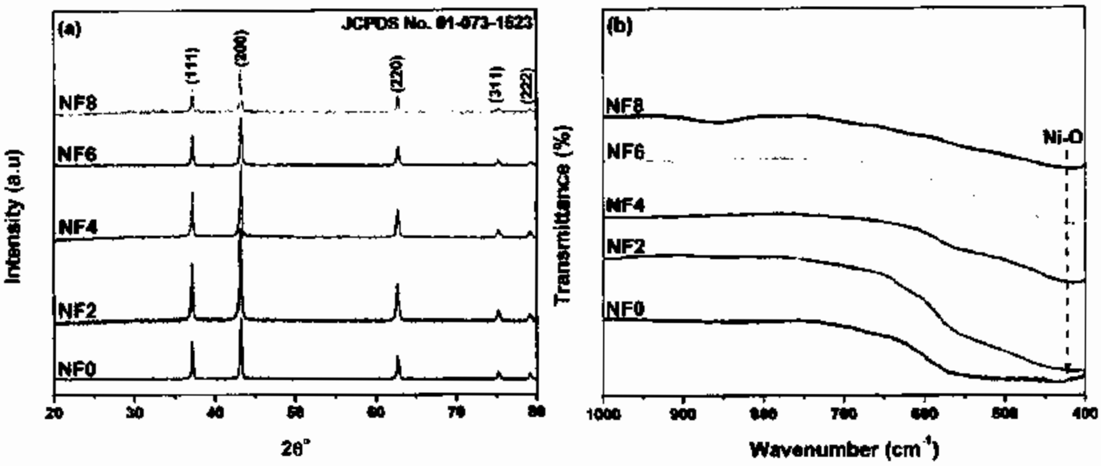

Figure 5.1: (a) XRD pattern and (b) FTIR spectra of NF0, NF2, NF4, NF6 and NF8 NPs.

5.2.2 Scanning Electron Microscopy (SEM) and Energy Dispersive X-ray (EDX) Spectroscopy

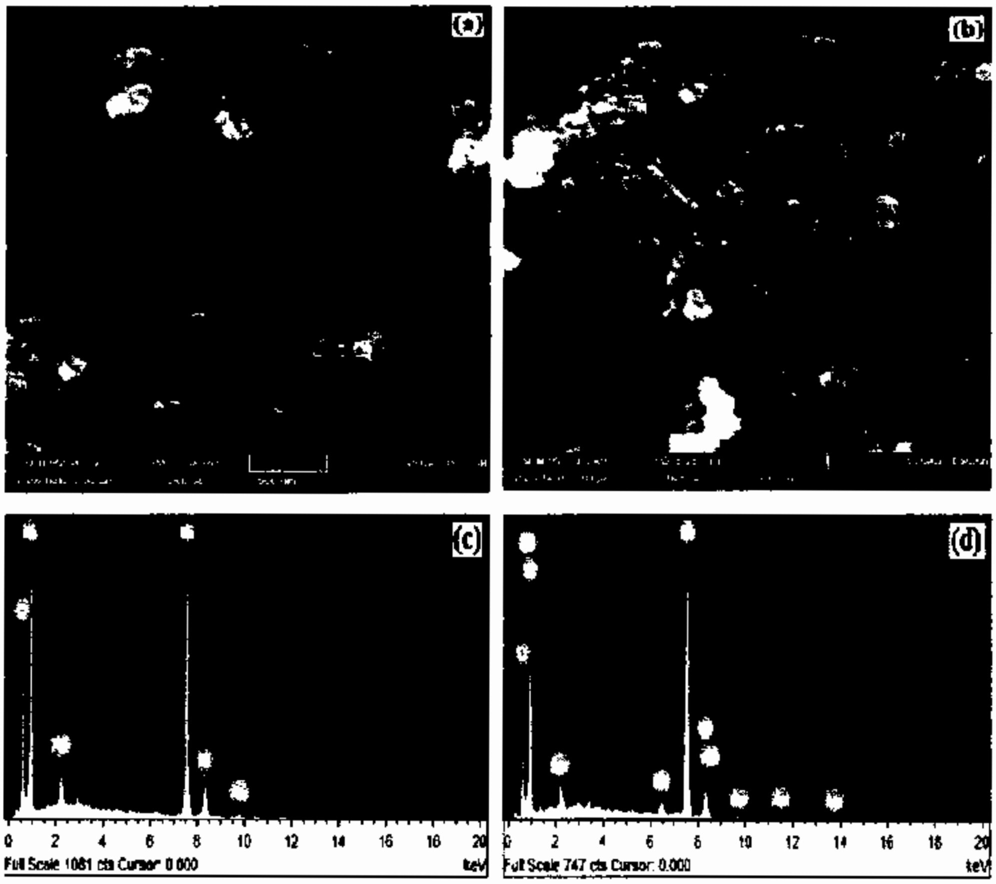

Figure 5.2: (a, b) SEM images of NF0 and NF8 NPs, respectively (c, b) EDX spectra of NF0 and NF8 NPs, respectively.

Fig. 5.2 (a, b) displays the SEM images of NF0 and NF8 NPs, respectively at 500 nm scale. It is clear that most of the NPs are spherical in shape with little agglomeration present. Fig. 5.2 (c, d) shows the EDX spectra of NF0 and NF8 NPs, respectively. The presence of Ni, Fe and O peaks confirmed the Fe doping whereas the existing Au peak is due to gold sputtering for achieving better resolution.

5.2.3 Raman Spectroscopy

This technique is a useful probe to investigate the lattice disorder, structural transitions, cationic distribution and magnetic ordering. Fig. 5.3 shows the Raman spectra of pure and Fe doped NiO NPs at room temperature.

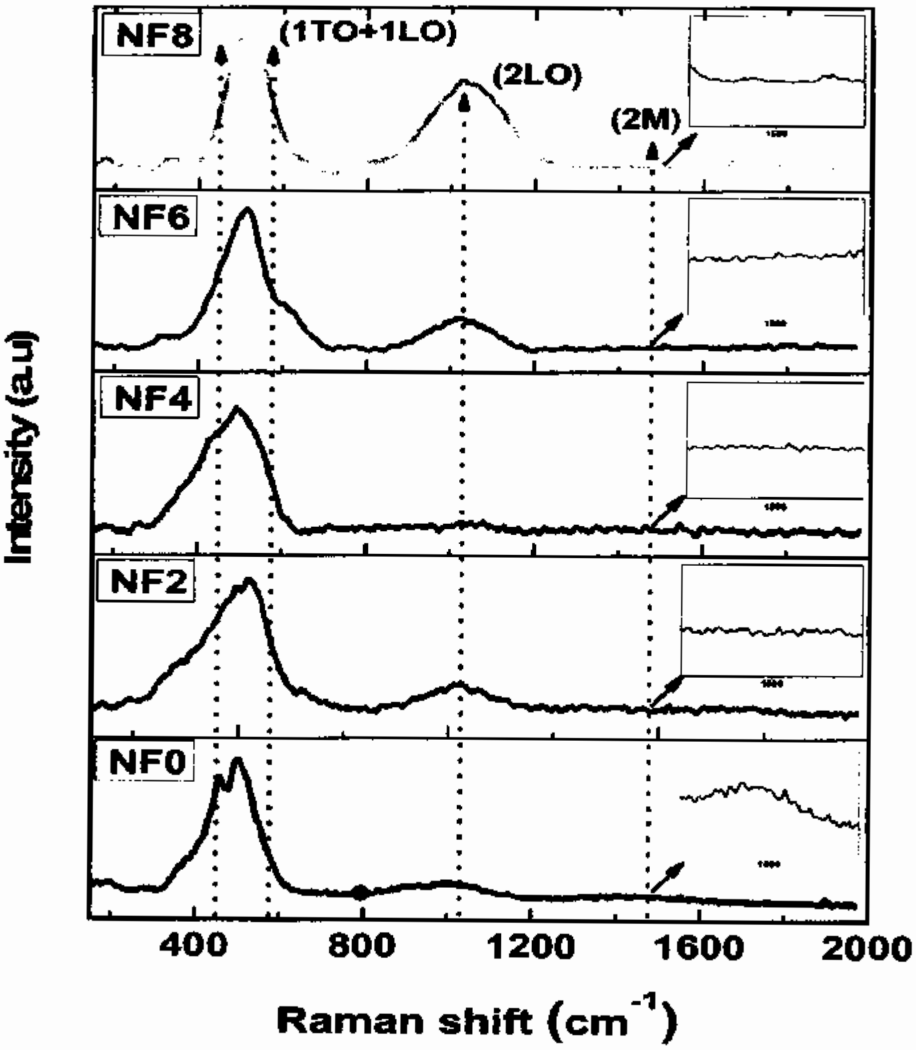

Figure 5.3: Raman spectra of NF0, NF2, NF4, NF6 and NF8 NPs. Insets show zoom portion of 2M band.

The band in the range 400-600 cm^{-1} is due to the overlapping of first order phonon (1P) (1TO = 440 cm^{-1} and 1LO = 560 cm^{-1}) [112]. The 1TO and 1LO scattering modes are not observable in bulk NiO and stoichiometric NiO, therefore the presence of these modes in NiO NPs are attributed to surface disorder, interstitial oxygen vacancies, broken symmetry and imperfectness in crystal structure [176]. Mironova *et al.* [119] observed the increased intensity of this band with decrease in crystallite size. Chen *et al.* [177] observed red shift in 1P mode of the silicon nanowires with decrease in diameter of wires and attributed it to size induced phonon confinement effect. No such red shift has been observed for our Fe doped samples due to very small difference in <D> (33-29 nm). The second order phonon (2P) band observed at 1025 cm^{-1} is attributed to longitudinal optical (2LO) stretching mode of NiO [178]. The two-magnon (2M) band has a magnetic origin and is characteristic feature of a bulk AFM material below T_N=523 K [179]. This band also gets disappear in small AFM NPs at room temperature due to reduced coordination of antiparallel spins [180]. In Fig. 5.3, insets show very weak band at 1472 cm^{-1} in NF0 that confirms weak AFM coupling in the core of NiO NPs. However, this band gets suppressed for Fe doped samples due to magnetic nature of Fe ions. Liu *et al.* [176] perceived RTFM in Fe doped NiO nanofibers and did not observed 2M peak in these samples. Therefore, absence of 2M peak in Fe doped NiO NPs is an indication of RTFM in these samples.

5.2.4 Magnetic Properties

5.2.4.1 M-H Loops

Fig. 5.4 shows the M-H loops of pure and Fe doped NiO NPs at 300 K. Bulk NiO is AFM below Néel temperature (T_N=573 K) but when its dimensions are reduced to nanoscale, the spins at the NPs surface progressively become unequal and remained uncompensated which get enhanced on reducing further crystallite size. Therefore, RT weak ferromagnetism in pure NiO NPs can be attributed to finite size effect [45]. It is clear from M-H loops that pure NiO NPs exhibited weak RTFM due to uncompensated surface spins with coercivity of 2614 Oe and remanence 0.025 emu/g. Tadic *et al.* [181] reported RTFM-like behaviour in NiO NPs with coercivity of 115 Oe and remanence 0.0087 emu/g. Continuous linear increase in magnetization with applied field is an indication of AFM core which is in agreement with the weak signal of 2M peak induced in NF0 as shown in

Fig. 5.3. The net magnetic moment increased for Fe doped samples and found maximum for NF6 sample as shown in Fig. 5.5 (a).

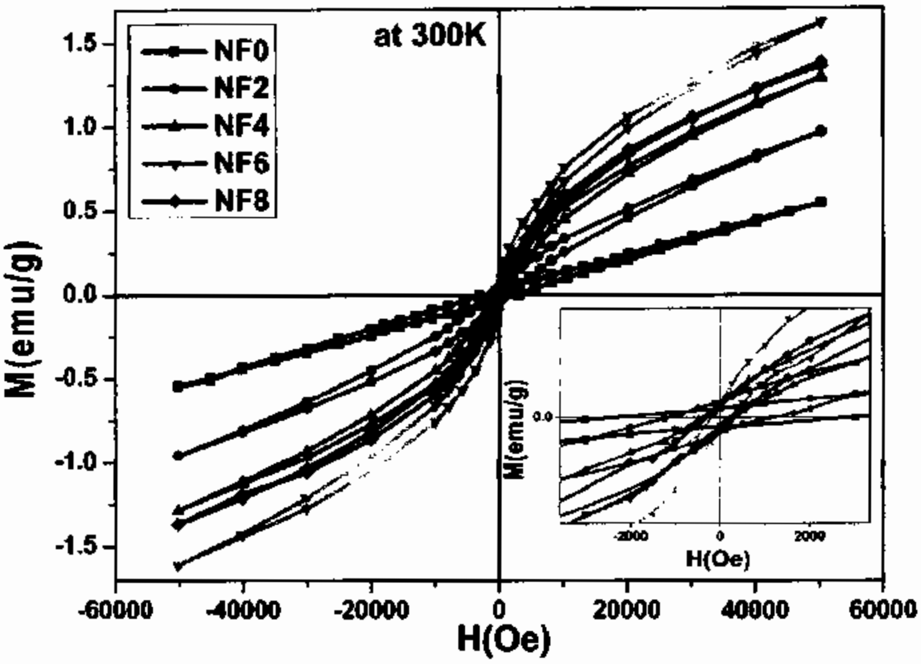

Figure 5.4: M-H loops of NF0, NF2, NF4, NF6 and NF8 NPs at 300 K.

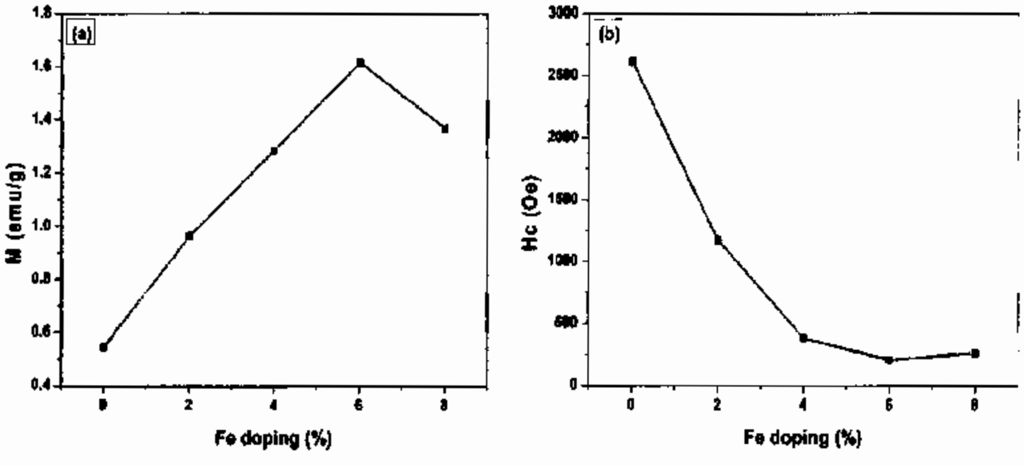

Figure 5.5: (a) Magnetization vs. Fe doping (%) at ±5T and (b) Coercivity (H_c) vs. Fe doping (%).

The doping of different metal ions induces structural disorder and have influence the <D>. Therefore, induced magnetization can be due to finite size of pure NiO NPs [68, 182, 183]. Ponnusamy *et al.* [58] observed RTFM in Fe doped NiO NPs and attributed it to decrease in <D>. In our case, Fe doping did not produced a significant change in the <D> so this aspect cannot be accounted for doped samples. From XRD and Raman results, it is also clear that no other secondary phase of Fe such as Fe_2O_3 and Fe_3O_4 is present, therefore this aspect of enhancement in net magnetization is also neglected. Many researchers [59, 184-186] reported the enhanced magnetization in Fe doped NiO NPs due to ferrimagnetic $NiFe_2O_4$ phase formation. Raja *et al.* [184] observed the ferrimagnetic $NiFe_2O_4$ phase for more than 2% Fe doping into NiO NPs but in our case no such impurity phase has been observed even up to 8% of Fe doping. The disorder generated by substitution of Ni^{2+} by Fe^{2+} (or Fe^{3+}) breaks the original translational symmetry of magnetic ions and super-exchange interaction (Ni^{2+}-O^{2-}- Ni^{2+}) in crystallites is interrupted [172]. There are two stable valance states of Fe ions exist, i.e. Fe^{2+} and Fe^{3+}. Douvalis *et al.* [186] observed the existence of Fe^{3+} ions into NiO matrix by Mossbauer spectroscopy, therefore enhanced net magnetic moment may be due to double exchange interaction of mixed valance states [187]. Khemprasit *et al.* [64] also observed the enhanced ferromagnetism in Fe doped NiO NPs and attributed it to generation of Ni vacancy defects and double exchange interactions. The net magnetic moment did not saturate up to 50 KOe which confirmed the presence of AFM phase in these NPs. The higher value of coercivity for pure NiO NPs is attributed to the presence of surface uncompensated spins. However, coercivity started decreasing with increasing Fe doping concentration due to the contribution of magnetization from core of the NPs as shown in Fig. 5.5(b).

5.2.5 Optical Properties

5.2.5.1 Optical Energy Bandgap

Before analysing the photocatalytic activity of Fe doped NiO NPs, it is necessary to investigate their optical band gap energy so that information about the activation energy of photocatalyst may be collected. The E_g of pure and Fe doped NiO NPs was evaluated from well-known Tauc's relation [188] and is shown by Tauc's plot in Fig. 5.6.

The DRS technique was employed to calculate the optical absorption coefficient [36]

$$F(R) = \frac{(1-R)^2}{2R} \tag{5.1}$$

Where $F(R)$ is Kubelka Munk function and R is the absolute reflectance of the material. The estimated E_g were 3.47, 3.51, 3.52, 3.53 and 3.57 eV for NF0, NF2, NF4, NF6 and

NF8 NPs, respectively. The smaller crystallites have larger band gap according to quantum confinement effect [189]. Hashem *et al.* [136] reported the increase in E_g from 3.51 to 3.60 eV when crystallite size of pure NiO is reduced from 34 to 14 nm. However, finite size effect cannot be considered for our Fe doped NiO NPs due to very small difference in <D> as calculated from XRD. Therefore, slight enhancement in E_g for Fe doped samples can be attributed to Moss-Burstein effect [138] in which Fermi level shift close to the conduction band due to doping which increases carrier density and leads to increase in E_g.

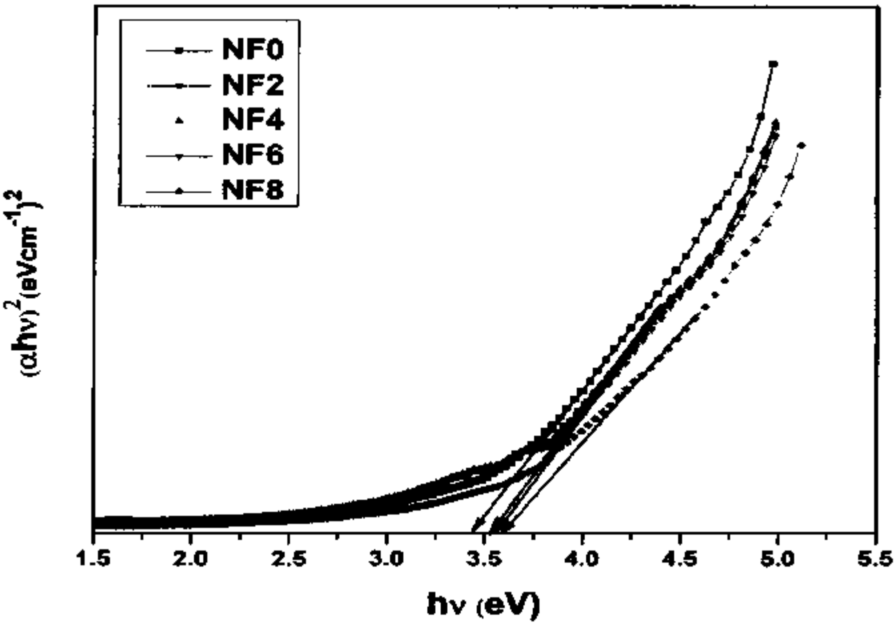

Figure 5.6: Tauc's plot for NF0, NF2, NF4, NF6 and NF8 NPs.

5.2.6 Photocatalytic Activity

The photocatalytic activity of synthesized samples was observed by using Methyl orange (MeO) dye which is widely used as model pollutant. The 70 ml MeO solution (15 mg/l) was taken in a beaker and 30 mg catalyst (Fe doped NiO NPs) was added to test photocatalytic degradation under UV illumination. In order to maintain absorption-desorption equilibrium, the MeO solution was stirred for 30 minutes in the dark. Fig. 5.7 (a-e) shows the absorbance spectra of MeO dye at various time intervals in the presence of NF0, NF2, NF4, NF6 and NF8 NPs used as photocatalyst. The maximum intensity of absorbance spectra of MeO dye was observed at 464 nm [174] which gradually get decreased with the increasing irradiation time and is attributed to the degradation of MeO dye molecules which confirms the photocatalytic ability of pure and Fe doped NiO NPs.

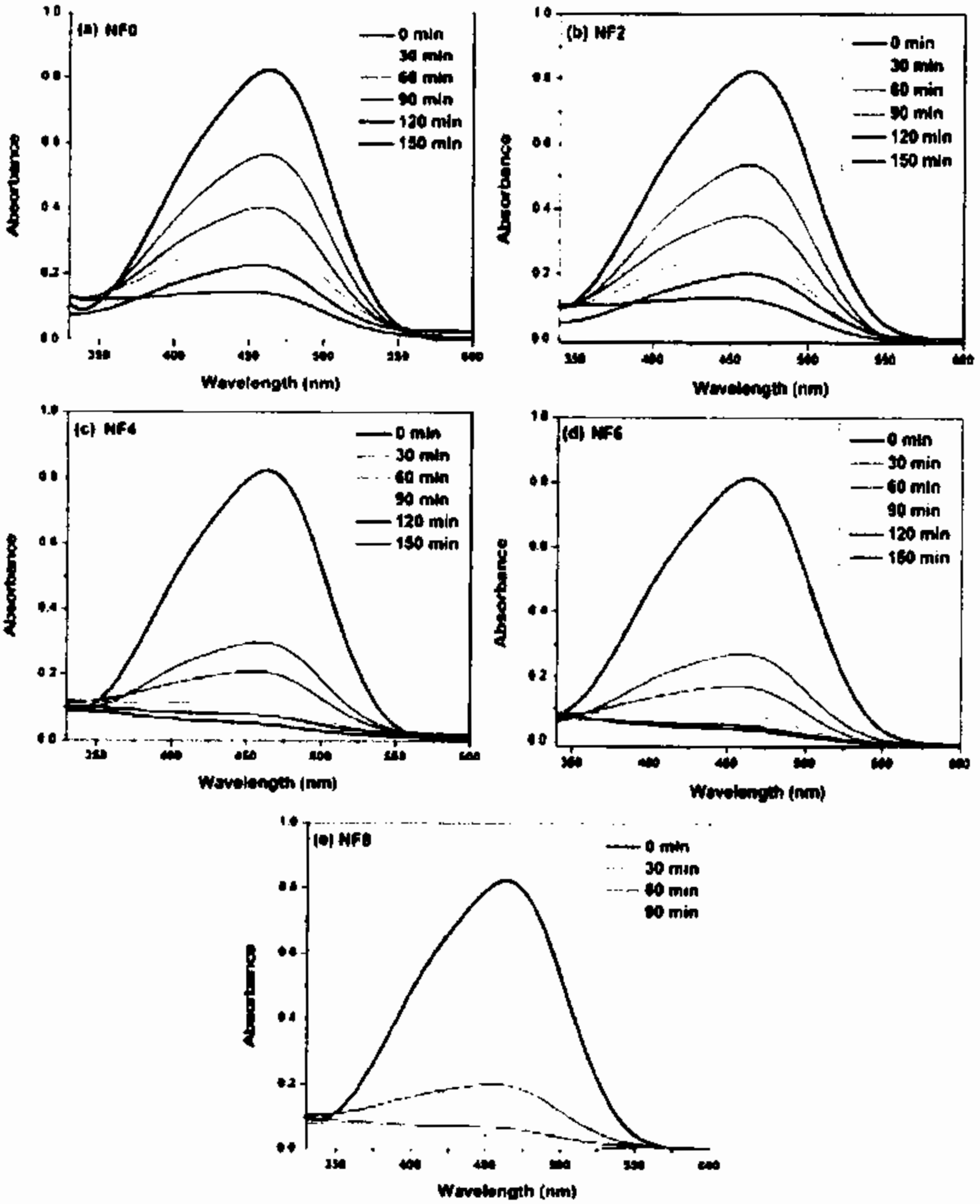

Figure 5.7: (a-e) Absorbance spectra of MeO dye in the presence of NF0, NF2, NF4, NF6 and NF8 NPs.

Fig. 5.8 (a) shows the variation in degradation percentage of MeO dye with irradiation time when pure and Fe doped NiO NPs were used as photocatalyst. The enhanced photocatalytic activity with Fe-doping may be attributed to following reasons:

(1) more absorption of photons due to generation of localized states, (2) higher doping rate increased concentration of oxygen vacancies that serve as energy traps to delay electron-hole recombination. Wang *et al.* [147] reported an enhanced photocatalytic activity of ZnO nanorods and attributed it to generation of oxygen vacancies that reduced the recombination rate of electron and holes. Fig. 5.8 (b) shows that after 90 minutes of UV irradiation, NF0 NPs only degraded 68% where NF8 completely degraded the model pollutant.

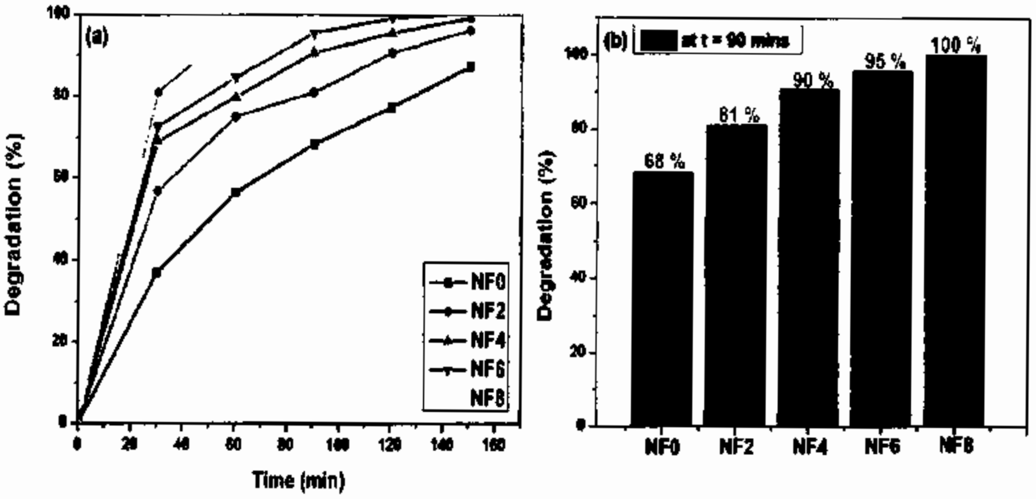

Figure 5.8: (a) Variation of Photo degradation percentage of NF0, NF2, NF4, NF6 and NF8 NPs with UV irradiation time and (b) Photo degradation percentage at 90 min UV irradiation time.

The photocatalytic dye degradation percentage was calculated by equation [99].

$$\text{Degradation (\%)} = \left(\frac{A_o - A_t}{A_o}\right) \times 100 \qquad (5.2)$$

Where A_0 and A_t are the maximum value of absorbance of MO dye at 0 and t minutes, respectively.

5.3 Magnetic Homogenity in Fe-Mn co-doped NiO Nanoparticles

Doping with different metal ions also plays a key role in controlling the magnetic properties of the NiO NPs [58-61]. The dopants in NiO can change its magnetization by adopting the parallel/antiparallel coupling to the Ni atoms or/and introducing frustrating into the magnetic structure. The room-temperature ferromagnetism is reported for NiO NPs doped with transition metals, e.g. Fe^{2+} and Mn^{2+} ions [39, 40]. In the case of single doping, there is a tendency of cluster formation between transition metals that manipulate the observed magnetic nature of the host material [190]. For example, Mn atoms often form segregated phases during annealing that makes the interpretation of magnetic behavior ambiguous [191]. Therefore, in order to avoid this, co-doping of transition metals is used to provide the necessary stability and understanding the underlying mechanism in a better way [72, 73, 192-194]. The co-doping of different transition metal ions becoming a promising strategy to effectively alter the magnetic properties of host materials such as ZnO [195], ZrO_2 [196], $BiFeO_3$ [197], etc. Manna *et al.* [73] observed the decrease in magnetic transition temperature by Fe and Li co-doping in NiO NPs. Paul *et al.* [62] reported that the clustering behavior of Mn is counteracted by Fe atoms and low clustering tendency observed for Fe and Mn co-doping in Ge matrix. The effective chemical pair interaction between Mn and Fe atom is positive, which indicates a segregating behavior of these atoms and forbids their clustering tendency [198]. The Fe and Mn doping have some interesting magnetic interactions reported in many studies [199-202]. Paul *et al.* [62] reported that the strength of FM interactions between Fe and Mn increases by increasing the Fe-doping concentration in Fe-Mn co-doped Ge matrix. However, Perumal [203] reported that the AFM interactions between Fe and Mn increase when the Mn concentration is increased in Fe-Mn-Zr alloy. Therefore, the aim of the study is to observe the effect of equal and different Fe and Mn doping concentrations on structural and magnetic properties of NiO NPs. The choice of Fe and Mn doping concentration has significant impact on the magnetic properties of NiO NPs. Layek *et al.* [40] reported maximum net magnetization for 2 at.% of Mn doping in NiO NPs and decreased sharply for higher Mn doping concentration. On the other hand, our previous study [204] revealed that the net magnetization of Fe doped NiO NPs increases up to a critical level of 6 at.% of Fe doping concentration. The higher concentration of dopants may result into a FM impurity phase which is highly undesirable for studying the AFM system. He *et al.* [185] observed a significant amount of $NiFe_2O_4$ phase for 10% of Fe doping concentration in NiO NPs. The Fe and Mn co-doping may provide necessary thermal stability for magnetic interactions in NiO and possibly induce homogeneity in the nuclear and magnetic structure which is important for different magnetic applications. In the next section, the effect of Fe and Mn co-doping on structural and magnetic properties of NiO NPs has been studied.

5.4 Results and Discussion

For single or co-doping, a maximum of 8 at.% of Fe and Mn dopants were used in NiO NPs. The samples were labelled as; Pure NiO (S1), 8% Mn doped (S2-M8F0), 6% Mn-2% Fe co-doped (S3-M6F2), 4% Mn-4% Fe co-doped (S4-M4F4), 2% Mn-6% Fe co-doped (S5-M2F6) and 8% Fe doped (S6-M0F8).

5.4.1 X-ray Diffraction (XRD)

Fig. 5.9 (a-f) shows the XRD patterns with Rietveld refinement fitting results of S1, S2-M8F0, S3-M6F2, S4-M4F4, S5-M2F6 and S6-M0F8 NPs samples by using FullProf software package. The phase formation of the NPs were confirmed by XRD. The diffraction peaks at ~ 37.1°, 43.2°, 62.8°, 75.3° and 79.3° corresponds to (111), (200), (220), (311) and (222) planes of rock-salt FCC structure of NiO, respectively with *Fm-3m* space group. The FM Ni phase which is an impurity phase and usually observed at low annealing temperature was not present in our samples [65]. The other possible impurity phases, like $NiFe_2O_4$, Fe_2O_3 and Fe_3O_4, MnO, $MnFe_2O_4$ etc. which have magnetic origin were not found either.

The average crystallite size (<D>) was found to be 38, 37, 34, 32, 33 and 35 nm for S1, S2-M8F0, S3-M6F2, S4-M4F4, S5-M2F6 and S6-M0F8 NPs samples, respectively. A very small change in <D> was observed due to insignificant difference in ionic radii of Ni^{2+} (0.69 Å), Mn^{2+} (0.67 Å) and Fe^{2+} (0.74 Å) or Fe^{3+} (0.64 Å) ions. The size effects are almost the same in these crystallites and therefore ideal case for studying the doping effects in NiO NPs. Basically, the crystallite size is the measure of the structural coherence length which is significantly influenced by the distortion in the crystal lattice. Therefore, the small difference in ionic radii of dopant and host ions induces smaller incoherence and as a result the difference in crystallite size should remain almost same under same conditions.

For our system, Mn and Fe-ions are expected to occupy the Ni^{2+} site without too much violating the crystal structure of NiO due to small difference in ionic radii. Therefore, we observed the small difference in <D> of all samples which lies in the range 32-38 nm. Boukhari *et al.* [205] reported the decrease in <D> of NiO NPs by rare earth elements (Er, Sm, Gd, Pr and Y) doping and attributed it to the large difference in ionic radii of host and dopants. Some of the important structural parameters obtained from Rietveld refinement fitting for samples S1, S2-M8F0, S3-M6F2, S4-M4F4, S5-M2F6 and S6-M0F8 along with their respective goodness-of-fit are listed in Table. 5.1.

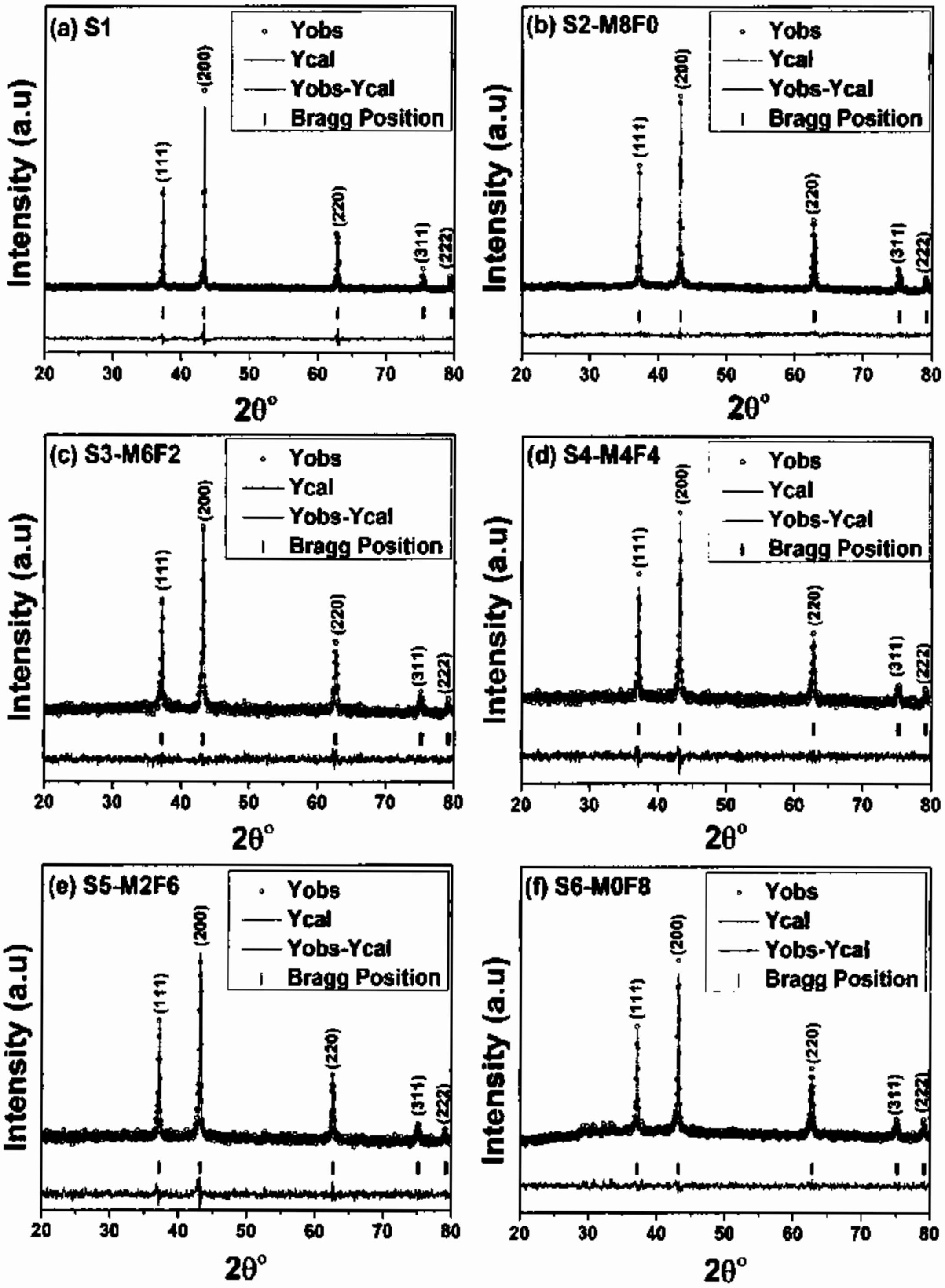

Figure. 5.9: XRD scans with Rietveld refinement fitting for samples (a) S1, (b) S2-M8F0, (c) S3-M6F2, (d) S4-M4F4, (e) S5-M2F6 and (f) S6-M0F8.

The lattice constants (a=b=c) for undoped NiO NPs was found to be 4.178 Å which is in accordance with previously reported studies [206-208]. It can be seen that the value of lattice constant is a bit greater for doped samples which may be due to micro-strain produced in the crystal structure [116]. Patel *et al.* [116] reported the increase in lattice constant with increasing Fe doping concentration in NiO NPs.

Table 5.1: Structural parameters for samples S1, S2-M8F0, S3-M6F2, S4-M4F4, S5-M2F6 and S6-M0F8 obtained from Rietveld refinement fitting.

Sample	Lattice constant (Å) a=b=c	Angle $\alpha=\beta=\gamma$	Weighted profile R-value (R_{wp})	Expected R-value (R_{exp})	Bragg R-factor (R_B)	Goodness-of-fit (χ^2)
S1	4.178	90°	35.5	32.18	8.518	1.22
S2-M8F0	4.188	90°	24.2	18.93	7.264	1.63
S3-M6F2	4.189	90°	37.3	35.66	3.805	1.10
S4-M4F4	4.191	90°	40.7	40.50	3.832	1.05
S5-M2F6	4.191	90°	41.0	37.38	9.684	1.20
S6-M0F8	4.190	90°	31.4	28.88	4.779	1.18

5.4.2 Transmission Electron Microscopy (TEM)

Fig. 5.10 (a, b) shows the TEM images of the NiO NPs at magnification of 50 and 100 nm. It is clear that some of NPs are agglomerated and cubical in shape, however majority of them are well dispersed and spherical in shape.

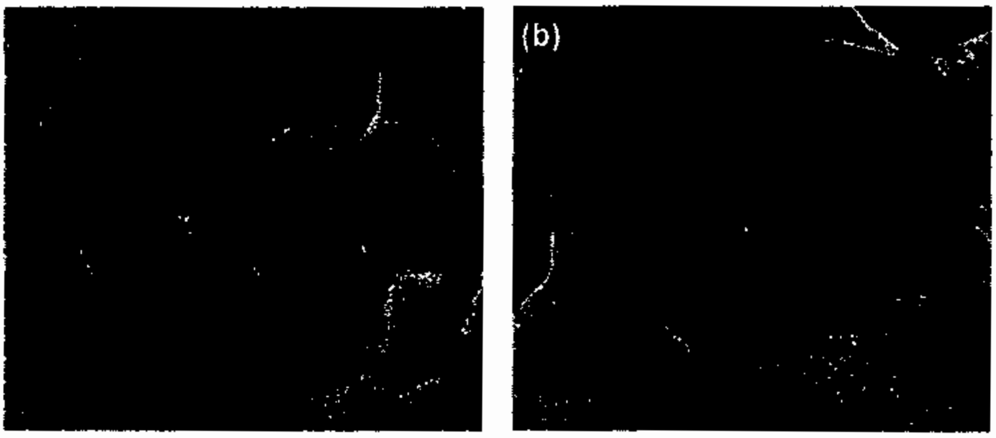

Figure 5.10: TEM image of NiO NPs at magnification of (a) 50 nm (b) 100 nm.

5.4.3 Ferromagnetic Resonance (FMR)

Ferromagnetic resonance (FMR) experiments were performed for all the samples at 9.22 GHz (X-band) as a function of a dc magnetic field (0-0.5 T) at room temperature. The FMR principle is based on the fact that the magnetic moments of atoms/ions rotate (called precession) with the same applied microwave frequency when resonance condition occur at applied resonance field H_r. The absorption of microwave frequency occur by the sample at resonance field H_r and its value indicate the strength of internal field [53].

Fig. 5.11 (a) shows the cavity FMR resonant absorption signal of all samples while Fig. 5.11 (b) shows its differential FMR absorption signal. This differential FMR absorption signal was fitted with expression for the derivative of the real part of a complex-valued combination of the Lorentzian and dispersive terms and the fit yielded the resonance field H_r and the resonance linewidth dH for all samples as shown in Fig. 5.11 (c, d). The amplitude of the absorption signal scales as the net magnetization [159] and found that it increases linearly with the Fe doping percentage in co-doped samples and reaches maximum for sample S5-M2F6 indicating maximum net magnetization for this sample.

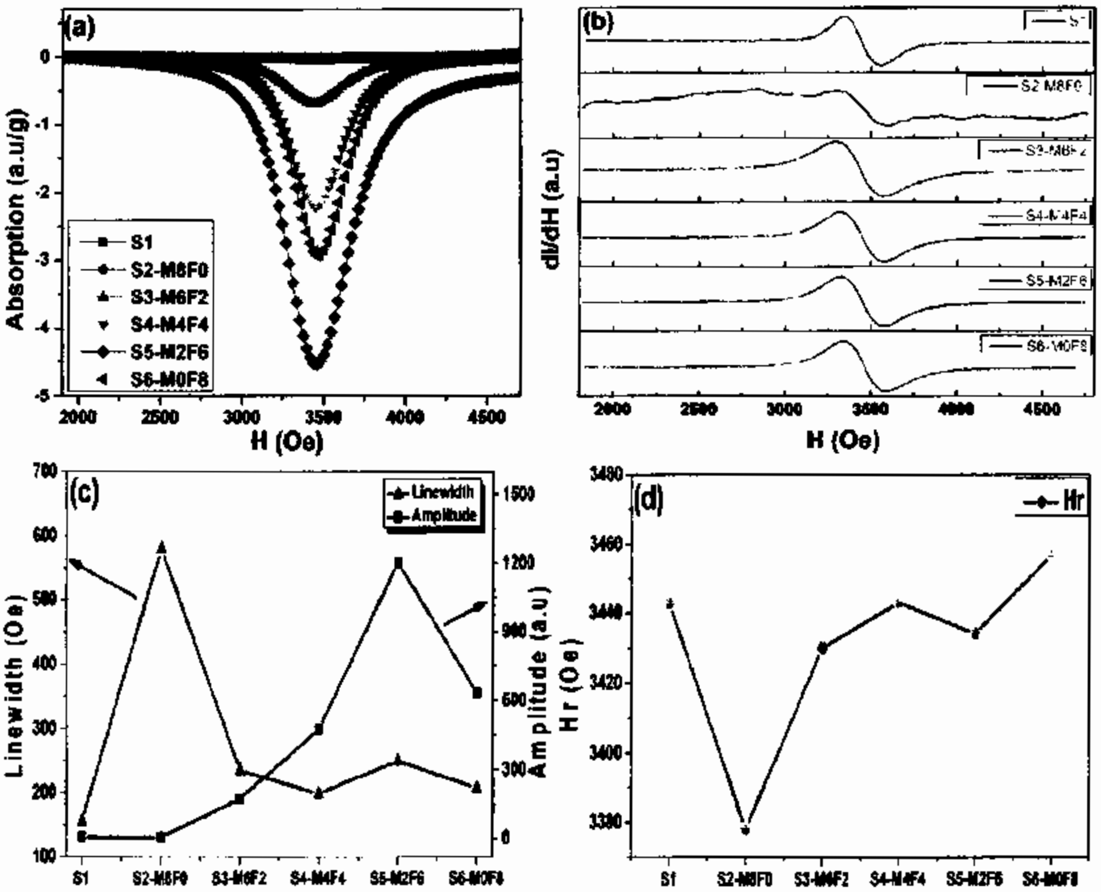

Figure 5.11: (a) FMR absorption, (b) differential absorption, (c) absorption amplitude and linewidth, and (d) resonance field for S1, S2-M8F0, S3-M6F2, S4-M4F4, S5-M2F6 and S6-M0F8 nanoparticles samples.

The dH is the measure of inhomogeneity of spin structure in the material [53]. It is observed that dH is maximum for sample S2-M8F0 indicating the presence of inhomogeneous local fields produced by Mn doping. Gandhi *et al.* [53] observed that the dH get broaden for smaller NiO NPs due to the generation of defects that produce inhomogeneous local fields. The dependence of dH on the magnetic exchange field (H_{ex}) and magnetic anisotropy field (H_a) can be described by the expression [209] $dH \sim H_a^2/H_{ex}$, which shows that dH increases with an increase in the magnetic anisotropy field and a decrease in the exchange interaction field. Therefore, it may be concluded that the broad resonance linewidth for sample S2-M8F0 is due to the large magnetic anisotropy field and small exchange interaction field in theses NPs. In general, H_r is a measure of the net magnetization, the strength of the internal static magnetic field, and magnetic anisotropy. The resonance field is also affected by inter-particle dipole coupling. The lowest value of

H_r for sample S2-M8F0 may evidence the presence of some paramagnetic spins/weak exchange interactions in the core/surface of the NiO NPs. Thus, Mn doping in NiO increases the magnetic inhomogeneity in the core spin structure.

For anisotropy field and processional magnetization damping rate observation, broadband FMR spectra (8-18 GHz) in step of 1 GHz were carried out by placing the sample on top of a micro-stripline. The measurements have been taken at room temperature for the selected samples S3-M6F2, S4-M4F4, S5-M2F6 and S6-M0F8, which have good response at different frequencies and shown in Fig. 5.12 (a).

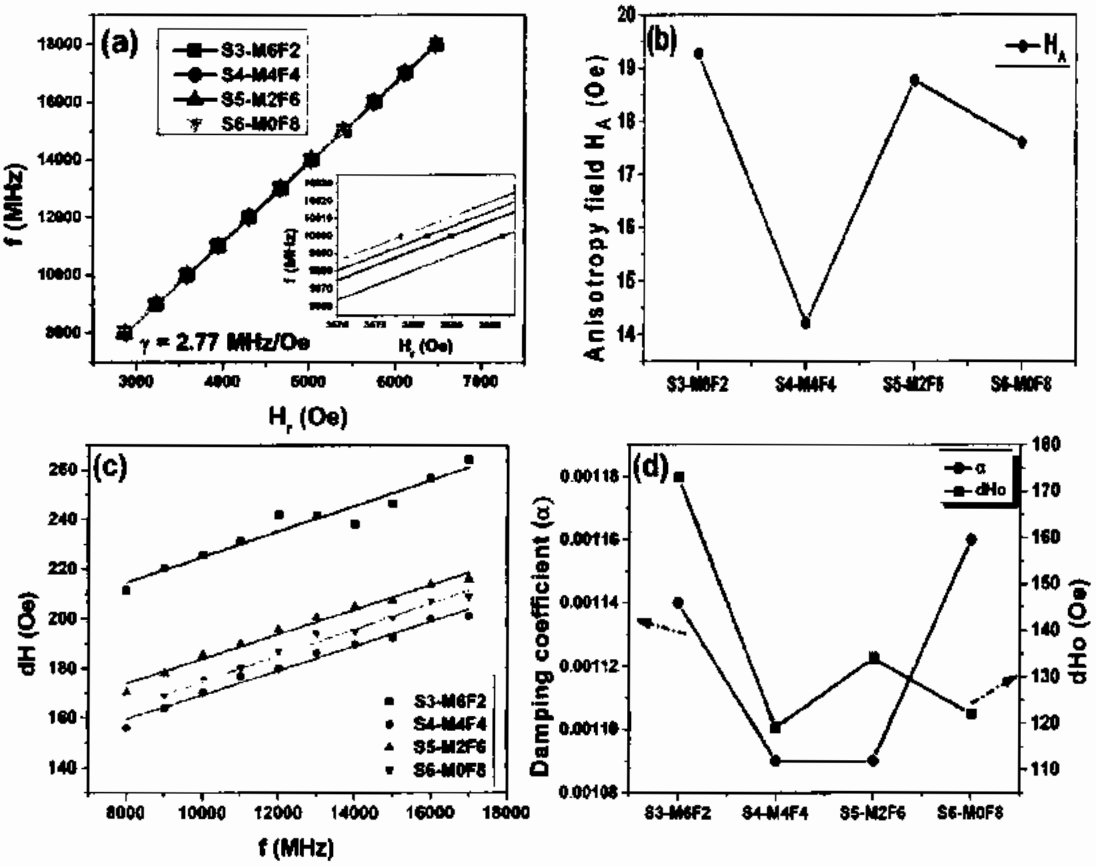

Figure 5.12: (a) Frequency dependant resonance field, (b) anisotropy field, (c) frequency dependent line width, and (d) damping coefficient (α) and extrinsic damping (dH_o) for S3-M6F2, S4-M4F4, S5-M2F6 and S6-M0F8 nanoparticles samples.

The static magnetic field was swept in the range 0-0.7 T for taking the broadband FMR measurements. In both cases, microwave absorption was detected with a microwave diode whose output was fed into a lock-in amplifier. An additional small ac modulation field was applied to the samples, and the lock-in amplifier was referenced by the modulation signal. The frequency of the signal was 21 KHz for the cavity FMR and 220 Hz for the stripline one. In these conditions, the output voltage of the lock-in amplifier scales as the first derivative of the FMR absorption signal with respect to the applied field ("differential absorption").

The FMR mode for a particle with a spherical shape is given by the equation [210], $\omega_r = \gamma(H_r + H_A)$, where ω_r, γ, H_r and H_A are the resonance frequency, the gyromagnetic ratio, resonance field and the effective magnetic-anisotropy field, respectively. The gyromagnetic ratio for all samples was found to be ~2.77 MHz/Oe. It is known that the precessing magnetization vector in a magnetic system experiences a damping torque. There are two fundamental damping mechanisms, intrinsic and extrinsic, and the total resonance linewidth obeys an equation [211], $dH = dH_0 + \frac{4\pi\alpha}{\gamma}f$, where and α is the intrinsic contribution to the damping (known as Gilbert damping) considered as fundamental to a system and calculated from the Landau–Lifshitz–Gilbert (LLG) equation [212] and dH_0 represents the extrinsic contribution to damping of magnetization precession [213]. The intrinsic damping in a material is related to the spin-orbit coupling [212] which dissipates energy to the lattice and represents the main source of damping. The intrinsic damping in the system with impurity or doping is due to the change of electron-magnon interaction [214, 215]. The extrinsic damping arises due to the inhomogeneity in the crystal structure by lattice defects [214, 216], local structural defects arising from impurity (doping), surface defects, strain due to lattice mismatch, and local variations in magnetic properties linked with structural defects such as local anisotropies etc [217, 218]. Therefore, the large density of these inhomogeneities tends to block the magnetization to process uniformly. Fig. 5.12 (b-d) shows the anisotropy field (H_A), frequency dependent dH, and intrinsic damping coefficient (α) and extrinsic contribution to the damping (dH_0), respectively for the samples S3-M6F2, S4-M4F4, S5-M2F6 and S6-M0F8. It is clear that the sample S3-M6F2 containing 6% Mn has higher value of H_A, α and dH_0 which indicate that the sample has higher inhomogeneity and structural defects and therefore smaller magnetization in comparison to other samples. However, the small value of H_A, α and dH_o for sample S4-M4F4 indicate the smaller structural inhomogeneity and small local variation in magnetic properties caused by co-doping.

5.4.4 Magnetic Properties

The magnetic measurements such as M-H loops (0-5 T), ZFC-FC magnetization in 5-300 K range, were carried out with SQUID magnetometer.

5.4.4.1 M-H Loops

Fig. 5.13 (a) shows the M-H loops taken at 300 K for samples S1, S2-M8F0, S3-M6F2, S4-M4F4, S5-M2F6 and S6-M0F8 whereas the inset to the figure shows zoom-in to the loop area near the origin. Fig. 5.13 (b) shows the variation in net magnetization (M) at 5 T and the coercive field (H_c) for these samples. We did not observed the saturation in magnetization and therefore calculated the net magnetization at 5 T by relation, $M = (\frac{M^+ + M^-}{2})$. Similarly, the coercivity is calculated by the relation, $H_c = (\frac{H_c^+ + H_c^-}{2})$.

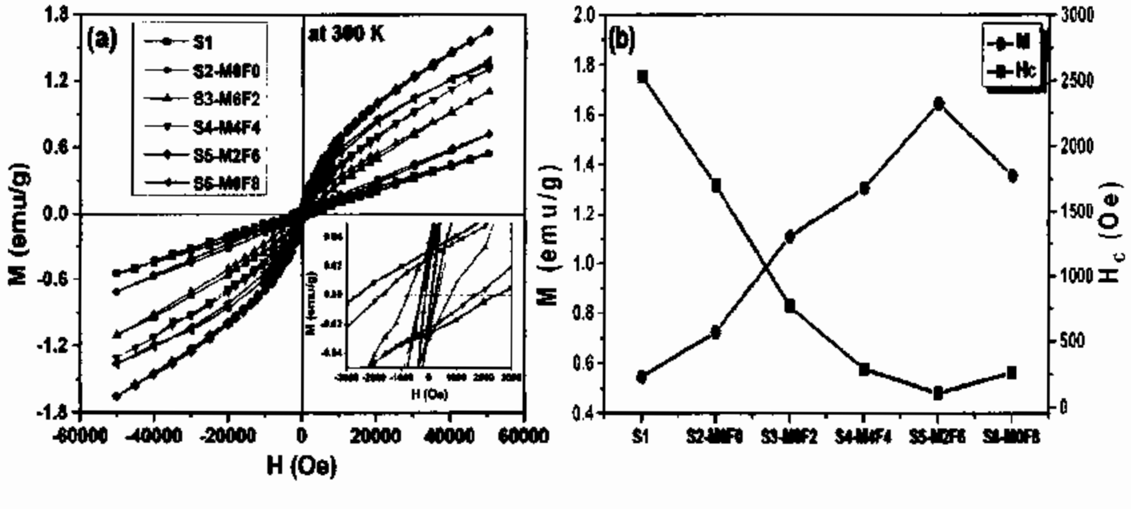

Figure 5.13: (a) M-H loops at 300 K whereas inset shows the zoom-in to the area near origin, and (b) magnetization (at 5T) and coercivity of samples S1, S2-M8F0, S3-M6F2, S4-M4F4, S5-M2F6 and S6-M0F8.

Bulk NiO is AFM at room temperature, however when its dimensions are reduced down to nanoscale (below 20 nm), the uncompensated spins at the surface and in the core induces net magnetization and room temperature ferromagnetism is reported [121]. Hence, room temperature ferromagnetism in NiO NPs can be attributed to the finite size effect [45]. However, in our case, NiO NPs (S1) have large size (38 nm) and therefore the contribution from the uncompensated core spins is negligible and small net magnetization is from the uncompensated surface spins. The continuous linear increase in magnetization with applied magnetic field in M-H loop indicate its AFM nature. Furthermore, higher value of coercivity (H_C) for this sample (S1) indicates the presence of surface uncompensated spins. For sample S2-M8F0, linear increase in magnetization with relatively smaller H_C indicate its AFM nature. The higher Mn doping concentration decreases the magnetic homogeneity in the system (as also evident from its large linewidth in Fig.5.11 (c)) and therefore magnetization get decreased. Layek *et al.* [40] reported the decrease in magnetization with increasing Mn concentration in NiO NPs. However, when the Fe doping percentage is increased (Mn doping concentration decreased), the formation of S-like shape of M-H loops indicate the room temperature ferromagnetism like behaviour. As there is no significant change in <D> occurred by doping, therefore finite size effect can be ruled out. On the basis of XRD analysis, the possibility of enhancement in magnetization due to other secondary phases is also ruled out. The maximum net magnetization with S-like shape of M-H loop was observed for S5-M2F6 sample in accordance to its maximum absorption amplitude in Fig. 5.11 (c) and indicate that it is the doping effect. The previous reports of single Fe and Mn doping concentration into NiO NPs is also 6% and 2%, respectively for the maximum net magnetization [204, 219] and was attributed to the double exchange interaction. The electron transport between mixed valance states such as Fe^{2+} and Fe^{3+} via oxygen ion (Fe^{2+}-O^{2-}- Fe^{3+}) is known as double exchange interaction. This interaction tends to couple the ions in FM order, however, long range magnetic order did not produced due to the small amount of Fe^{3+} ions. However, increasing Fe doping concentration convert Fe^{3+} state to Fe^{2+} state and favours the AFM super-exchange interactions (Fe^{2+}-O^{2}—Fe^{2+}) which is responsible for decreased magnetization after a critical doping level [220, 221]. Soni *et al.* [220] reported the RTFM in Fe doped CeO_2 polycrystalline samples and observed decrement of net magnetization after 5% of Fe doping concentration. However, in our case, net magnetization start decreasing after 6% Fe doping concentration in NiO NPs. The same behaviour is observed for Co [222] and Ni [223] doped CeO_2 samples, in which magnetization increases up to a certain doping level and then decreased. It is also observed that the net magnetization did not even saturate for 50 kOe, confirming the presence of AFM phase in all samples. The decrease in Hc with increasing Fe doping concentration (minimum for sample S5-M2F6) is due to the magnetization contribution from the core. Moura *et al.* [61] observed the decrease of Hc with increasing Fe doping concentration in NiO NPs.

5.4.4.2 Zero field cooled (ZFC) and field cooled (FC) Magnetization

Fig. 5.14 (a-f) shows the temperature dependent magnetic behaviour of samples S1, S2-M8F0, S3-M6F2, S4-M4F4, S5-M2F6 and S6-M0F8.

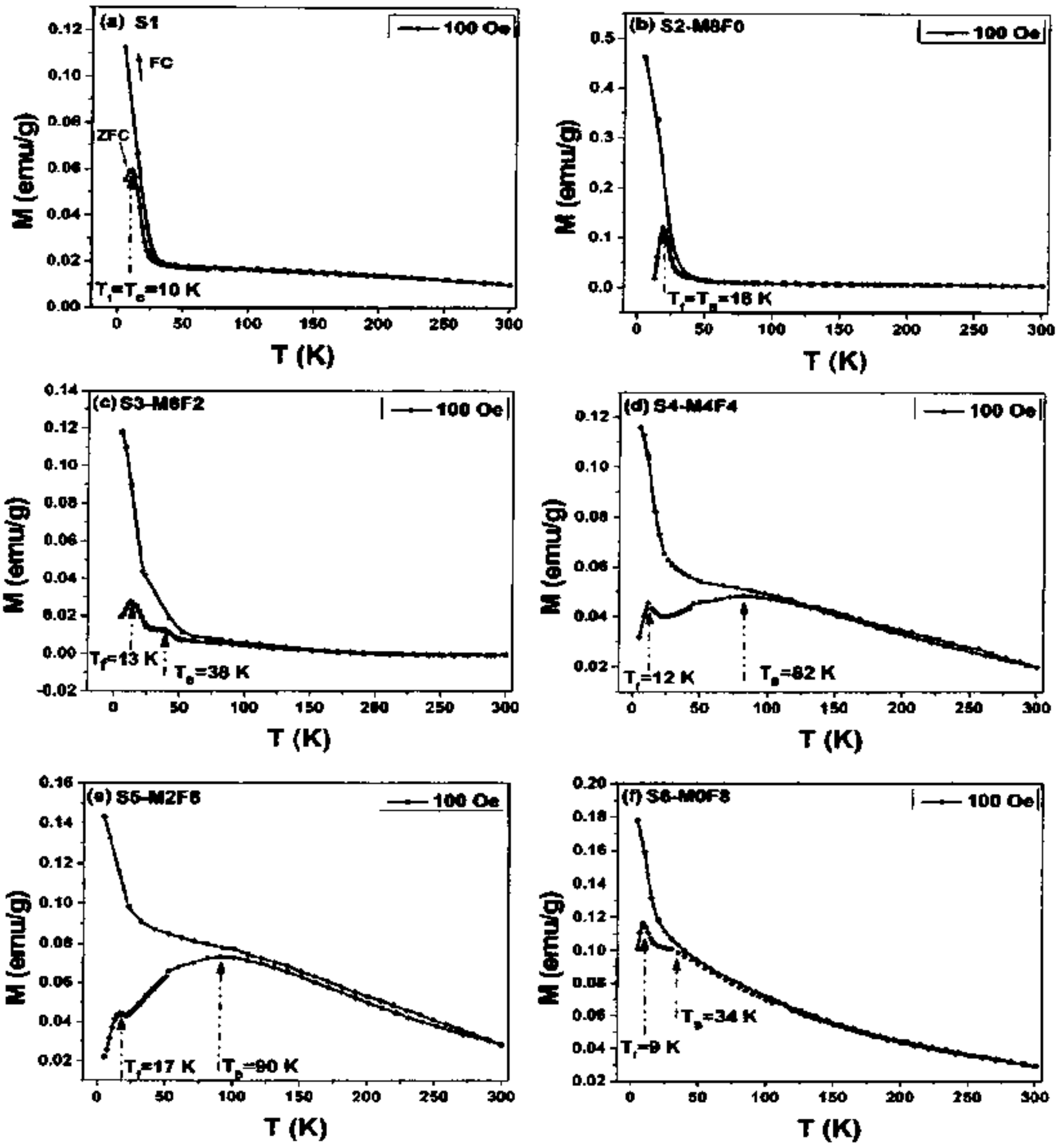

Figure 5.14: (a-f) ZFC/FC magnetization curves for samples S1, S2-M8F0, S3-M6F2, S4-M4F4, S5-M2F6 and S6-M0F8, respectively at 100 Oe.

The ZFC-FC magnetization curves were taken in the temperature range of 5-300 K at 100 Oe. In ZFC curves, the low temperature peak in the range 9-18 K is due to the frozen uncompensated spins at the surface of NPs and designated as freezing temperature (T_f) peak reported in many studies on NiO NPs [70, 224, 225]. However, another peak observed at higher temperature is due to the magnetization contribution from the core of NPs and is known as blocking temperature (T_B) peak [226]. This peak is absent for samples S1 and S2-M8F0, due to small net magnetization from the core of nanoparticle which is thermally unstable at high temperature. As a result, T_f and T_B may overlap and lie in the same temperature range. The T_B peak was prominent for samples S4-M4F4 (82 K) and S5-M2F6 (90 K) in comparison to other samples due to the presence of magnetic interactions which blocked the net magnetization against thermal energy. There is no Néel transition region observed for any sample in the temperature range of 5-300 K, which shows that the T_N lies above the room temperature.

5.4.4.3 AC-Susceptibility

In order to further investigate the presence of magnetic interactions for samples S1, S3-M6F2, S4-M4F4 and S5-M2F6, the ac-susceptibility measurements were taken at frequency of 100 Hz and $H_{ac} = 5\ Oe$, as shown in Fig. 5.15 (a-d).

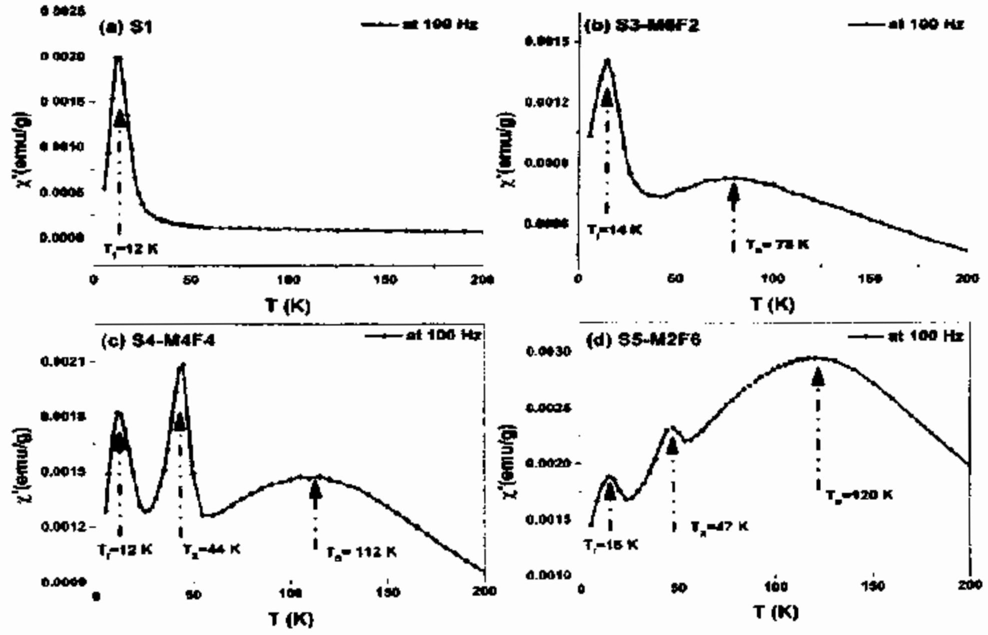

Figure 5.15: In-phase ac-susceptibility for (a) S1, (b) S3-M6F2, (c) S4-M4F4 and (d) S5-M2F6 nanoparticles samples, respectively at 100 Hz.

An unusual third peak at T_X appears for co-doped S4-M4F4 and S5-M2F6 samples which is completely absent for S1, and higher Mn concentration sample i.e. S3-M6F2. The T_X peak is found to be concentration dependent and found prominent in the case when concentration of both Fe and Mn atoms are equal, i.e. 4% Mn-4% Fe. Paul *et al.* [38] reported that the presence of Fe and Mn in Ge matrix increases the fraction of magnetic homogeneity and also the Fe and Mn coupling is FM. Therefore, the origin of T_X peak may be due to the FM coupling of Fe^{2+} and Mn^{2+} ions, which has maximum probability of coupling at equal concentration.

5.4.5 Neutron Diffraction

For the confirmation of magnetic homogeneity and magnetic coupling inside the core of interesting sample S4-M4F4, neutron diffraction patterns were taken at different temperatures 4, 12 (T_f), 44 (T_X), 112 (T_B), and 300 K as shown in Fig. 5.16 (a-e). The GSAS-II package based on Rietveld refinement method was used to perform the structural and magnetic phase refinement [165]. The high resolution neutron diffractometer (ECHIDNA) with highly sensitive detectors was used to obtain neutron diffraction patterns at the OPAL research reactor of Australian Nuclear Science and Technology (ANSTO) with a monochromatic neutron wavelength of 2.44 Å.

The observed nuclear and magnetic structure was found consistent with the previously-determined NiO nuclear and magnetic structure [56, 166, 167]. The nuclear and magnetic space groups were observed to be $Fm\bar{3}m$ and C2/n, respectively. The magnetic refinement corroborates the two magnetic sub-lattices theory with Ni spins oriented along (111) plane and the adjacent $\overline{\text{Ni}}$ plane anti-parallel to it [68, 69]. The large value of AFM exchange interaction between nearest neighbours in NiO is one of the reason behind the high value of its T_N in comparison to other transition metal mono-oxides [168, 227]. The magnetic reflection $(\frac{1}{2}\,\frac{1}{2}\,\frac{1}{2})$ from the AFM coupled (111) planes [167] is the focus of our study and observed at $2\theta \approx 29.2^\circ$ for all selected temperatures which confirms the homogenous AFM ordering of the core. Thus, the Fe^{2+} and Mn^{2+} ions coupled AFM to Ni^{2+} ions by super-exchange interaction. However, the mutual interaction between Fe^{2+} and Mn^{2+} ions may be FM and could be the possible reason behind the T_X peak. It can be seen that the intensity of this magnetic reflection decreases with increasing temperature, indicating the decreasing AFM-core diameter.

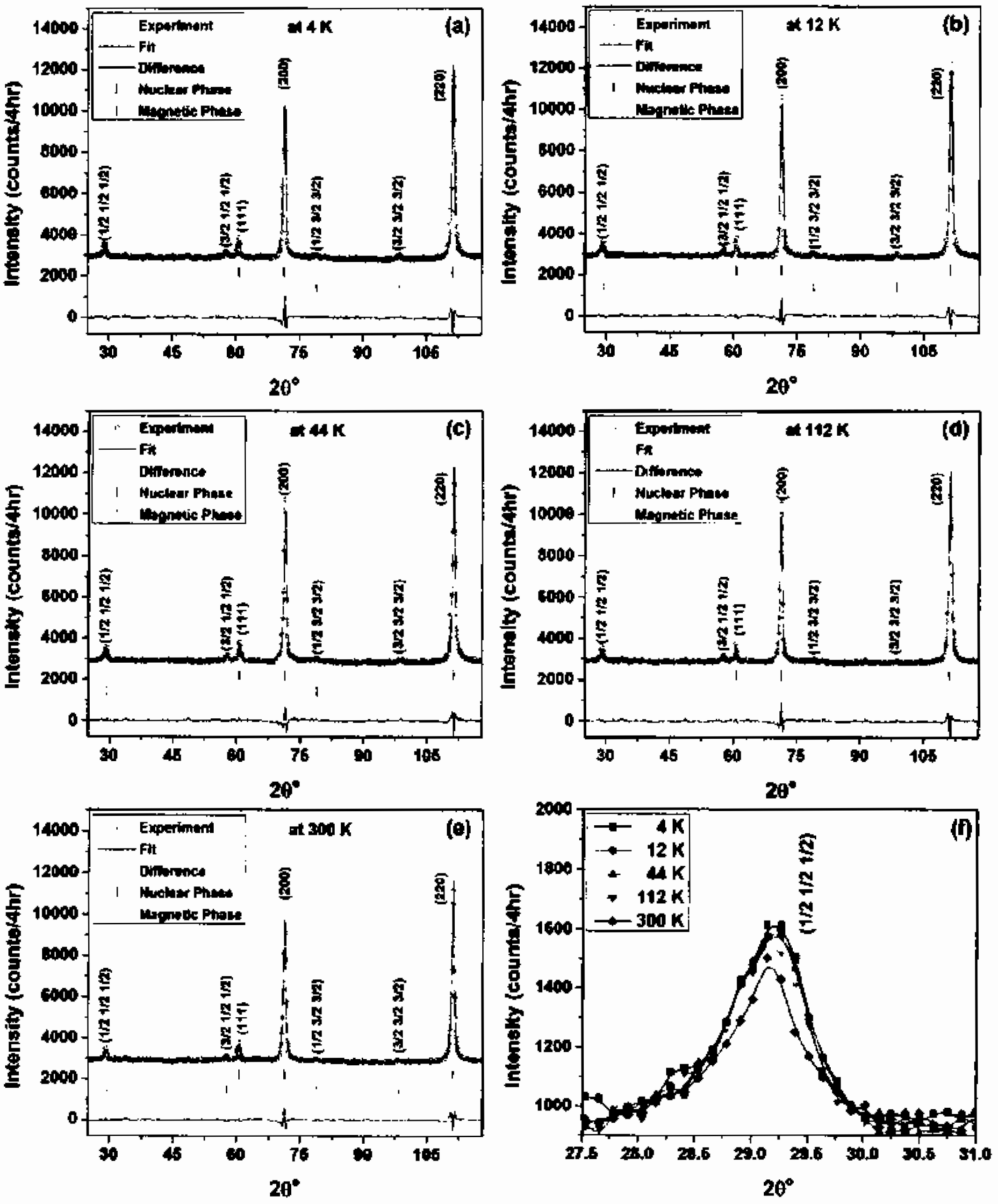

Figure 5.16: (a-e): Neutron diffraction pattern at 4, 12, 44, 112, and 300 K for sample S4-M4F4. The red solid lines are the results of Rietveld refinements to the experimental data and the blue lines are the difference between the results of the fits and the experimental data. The vertical green and purple lines indicate the position of the nuclear and magnetic Bragg peaks, respectively. And (f) shows the magnified portion of $(\frac{1}{2}\ \frac{1}{2}\ \frac{1}{2})$ magnetic reflection at 4, 12, 44, 112, and 300 K for sample S4-M4F4 without refinement.

The nuclear (D_{nuc}) and magnetic (D_{mag}) diameters were calculated from the broadening of nuclear and magnetic reflections, respectively and observed that the D_{mag} is smaller than the D_{nuc} due to surface spin disorder and the thickness of magnetic disorder shell is usually greater than nuclear disorder [169]. The D_{nuc} were observed to be $\langle D_{nuc} \rangle$ = 44.2 (5), 43.6 (4), 43.7 (5), 43.4 (5), 43.6 (4) nm and corresponding $\langle D_{mag} \rangle$ = 37.0 (4), 36.6 (3), 36.2 (3), 35.8 (4), 33.7 (4), respectively at temperature 4, 12, 44, 112, and 300 K. It is observed that the D_{nuc} is almost same at different temperatures whereas D_{mag} started decreasing with increase in thermal energy and expected to zero till Néel transition state (paramagnetic phase) occur.

Therefore, it may be concluded that the small and equal amounts of Fe and Mn co-doping in NiO NPs increase the magnetic homogeneity, increases thermal stability and reduce the structural defects that make the co-doped magnetic semiconductor attractive towards magnetic applications.

5.5 Conclusions

The Fe doped and Fe-Mn co-doped NiO NPs have been synthesized by CHM approach. The phase formation of pure and Fe doped NiO NPs has been confirmed by XRD and possible impurities which were commonly observed in literature such as Ni, Fe_2O_3, Fe_3O_4 and $NiFe_2O_4$ were not found. The Fe doping did not produced any significant change in the <D> due to small difference in ionic radii of Ni^{2+} and Fe^{2+} ions. FTIR spectroscopy revealed the presence of Ni-O bonding whereas SEM images showed the spherical shape of the both pure and Fe doped NiO NPs. The small 2M peak in Raman spectra reveal weak AFM in pure NiO NPs due to contribution from the core whereas high coercivity is attributed to uncompensated spins present on its surface. The M-H loops confirmed the RTFM in Fe doped NiO NPs and magnetization get increased with Fe doping and found maximum at 6% Fe doping. The optical energy band gap was found to be increased from 3.47 to 3.57 eV with increasing Fe doping which is attributed to shift in fermi level towards conduction band due to higher carrier concentration. The photocatalytic activity of NiO NPs was observed to be increased with increasing Fe doping concentration due to generation of oxygen vacancies and localized energy states that suppressed the electron-hole recombination rate.

For Fe-Mn co-doped NiO NPs, a maximum of 8 at.% of doping concentration was used with same and different concentration and the results have compared with 8 at.% of single doped Fe and Mn in NiO NPs. The FCC crystal structure of NiO was observed in all samples with <D> in 32-38 nm range. The FMR measurements confirmed that the sample with equal Fe and Mn co-doping concentration (4%) has the smallest structural and magnetic inhomogeneity. From room temperature M-H loops, the net magnetization increases with increasing Fe concentration in co-doped samples. In ZFC-FC curve, the T_B peak for samples with 4%Mn-4%Fe and 2%Mn-6%Fe co-doping in NiO NPs was observed at 82 and 90 K, respectively which was higher than observed in other samples and is attributed to the existence of magnetic interactions. In ac-susceptibility, an anomalous peak (T_X) in between T_f and T_B was observed which was more prominent in the sample with 4% Mn-4% Fe co-doping. The neutron diffraction patterns at different temperatures confirmed the AFM core of this sample, i.e AFM coupling between Ni^{2+} and Fe^{2+}/Mn^{2+} ions by super-exchange interaction. Therefore, the existence of T_X peak is attributed to the FM coupling of Fe^{2+} or Mn^{2+} ions. However, further investigation may be needed for making sound argument about the origin of $\mathrm{T_X}$ peak. The magnetic measurements confirmed that the small and equal Fe-Mn doping concentration in NiO NPs increases the magnetic homogeneity and reduces the structural defects that make it suitable for different magnetic applications.

General Conclusions

In first part of this dissertation, effect of different SiO_2 concentration on the magnetic and optical properties of NiO nanoparticles have been studied. It has been observed that the increasing SiO_2 concentration reduced the average crystallite size from 57 to 14 nm and enhanced photocatalytic activity of NiO NPs was observed in the presence of higher SiO_2 concentration (70 %). The higher concentration of SiO_2 behaved as wave-guiding medium to provide maximum energy to photocatalyst (NiO). The smallest (14 nm) obtained NiO nanoparticles was further investigated by magnetic measurements and neutron diffraction and showed most interesting properties. It has been observed that there is competing magnetic interaction between superparamagnetic blocking and Néel transition states for this critical size of 14 nm which resulted into an unusual and novel M-H loop splitting phenomenon. The main reason behind M-H loop splitting was due to the presence of slow spin relaxation which was further confirmed by some other experiments. Also, neutron diffraction confirmed the competing core-shell volume for this critical size of 14 nm.

In the second part of this dissertation, single (Fe) and co-doping (Fe-Mn) effects on optical and magnetic properties of NiO nanoparticles have been studied. It has been observed that the increasing Fe doping concentration (2 to 8 %) enhanced the photocatalytic activity of NiO nanoparticles due to generation of oxygen vacancies and localized energy states that suppressed the electron-hole recombination rate. The small 2M peak in Raman spectra reveal weak AFM in pure NiO NPs due to contribution from the core whereas high coercivity is attributed to uncompensated spins present on its surface. The M-H loops confirmed the RTFM in Fe doped NiO NPs and magnetization get increased with Fe doping and found maximum at 6% Fe doping. The cavity and broadband ferromagnetic resonance measurements confirmed that the 4%Fe-4%Mn co-doping induced structural and magnetic homogeneity in NiO nanoparticles and make it attractive for different magnetic applications. The complex magnetic structure of NiO NPs at nanoscale is fundamentally important for the future application in spintronic devices.

References

1. Mulay, L.N. and E.A. Boudreaux, Theory and applications of molecular diamagnetism. Wiley, 1976
2. Meiklejohn, W.H. and C.P. Bean, New magnetic anisotropy. Phy. Rev, 1956. **102**(5): p. 1413.
3. Takahashi, Y., On the origin of the Curie-Weiss law of the magnetic susceptibility in itinerant electron ferromagnetism. J. Phys. Soc. Jpn., 1986. **55**(10): p. 3553-3573.
4. Bozorth, R.M., Ferromagnetism, by Richard M. Bozorth, ISBN 0-7803-1032-2. Wiley-VCH, 1993.
5. Anderson, P., Antiferromagnetism. Theory of superexchange interaction. Phy. Rev, 1950. **79**(2): p. 350.
6. Seehra, M. and A. Punnoose, Deviations from the Curie-law variation of magnetic susceptibility in antiferromagnetic nanoparticles. Phys. Rev. B, 2001. **64**(13): p. 132410.
7. Rubinstein, M., R. Kodama, and S.A. Makhlouf, Electron spin resonance study of NiO antiferromagnetic nanoparticles. J. Magn. Magn. Mater., 2001. **234**(2): p. 289-293.
8. Tadic, M., et al., Magnetic properties of NiO (nickel oxide) nanoparticles: blocking temperature and Neel temperature. J. Alloys Compd., 2015. **647**: p. 1061-1068.
9. Khaetskii, A.V. and Y.V. Nazarov, Spin-flip transitions between Zeeman sublevels in semiconductor quantum dots. Phys. Rev. B, 2001. **64**(12): p. 125316.
10. Keffer, F. and H. Chow, Dynamics of the antiferromagnetic spin-flop transition. Phys. Rev. Lett., 1973. **31**(17): p. 1061.
11. Berkowitz, A. and K. Takano, Exchange anisotropy—a review. J. Magn. Magn. Mater., 1999. **200**(1-3): p. 552-570.
12. Zener, C., Interaction between the d shells in the transition metals. Phy. Rev, 1951. **81**(3): p. 440.
13. Wahl, P., et al., Exchange interaction between single magnetic adatoms. Phys. Rev. Lett., 2007. **98**(5): p. 056601.
14. Moriya, T., Anisotropic superexchange interaction and weak ferromagnetism. Phy. Rev, 1960. **120**(1): p. 91.
15. Rondinone, A.J., A.C. Samia, and Z.J. Zhang, Superparamagnetic relaxation and magnetic anisotropy energy distribution in CoFe2O4 spinel ferrite nanocrystallites. J. Phys. Chem. B, 1999. **103**(33): p. 6876-6880.
16. Grechka, V., P. Singh, and I. Das, Estimation of effective anisotropy simultaneously with locations of microseismic events. Geophysics, 2011. **76**(6): p. WC143-WC155.
17. Arelaro, A., et al., Interparticle interactions and surface contribution to the effective anisotropy in biocompatible iron oxide nanoparticles used for contrast agents. J. Appl. Phys., 2005. **97**(10): p. 10J316.

18. Franco, V. and A. Conde, Thermal effects in a Stoner–Wohlfarth model and their influence on magnetic anisotropy determination. J. Magn. Magn. Mater., 2004. **278**(1-2): p. 28-38.

19. Wernsdorfer, W., et al., Experimental evidence of the Néel-Brown model of magnetization reversal. Phys. Rev. Lett., 1997. **78**(9): p. 1791.

20. Néel, L. and T.D.T.M. Des Ferromagnetiques, En Grains Fins Avec Applications Aux Terres Cuites. Ann. Geophys, 1949. **5**: p. 99-136.

21. Hergt, R., S. Dutz, and M. Zeisberger, Validity limits of the Néel relaxation model of magnetic nanoparticles for hyperthermia. Nanotechnology, 2009. **21**(1): p. 015706.

22. Payet, B., et al., Influence of particle size distribution on the initial susceptibility of magnetic fluids in the Brown relaxation range. J. Magn. Magn. Mater., 1998. **186**(1-2): p. 168-174.

23. Mikhaylova, M., et al., Superparamagnetism of magnetite nanoparticles: dependence on surface modification. Langmuir, 2004. **20**(6): p. 2472-2477.

24. Dickson, D.P., Nanostructured magnetism in living systems. J. Magn. Magn. Mater., 1999. **203**(1-3): p. 46-49.

25. Gonzales-Weimuller, M., M. Zeisberger, and K.M. Krishnan, Size-dependant heating rates of iron oxide nanoparticles for magnetic fluid hyperthermia. J. Magn. Magn. Mater., 2009. **321**(13): p. 1947-1950.

26. Hiergeist, R., et al., Application of magnetite ferrofluids for hyperthermia. J. Magn. Magn. Mater., 1999. **201**(1-3): p. 420-422.

27. Dormann, J., L. Bessais, and D. Fiorani, A dynamic study of small interacting particles: superparamagnetic model and spin-glass laws. J Phys C Solid State Phys, 1988. **21**(10): p. 2015.

28. Thota, S., J. Shim, and M. Seehra, Size-dependent shifts of the Néel temperature and optical band-gap in NiO nanoparticles. J. Appl. Phys., 2013. **114**(21): p. 214307.

29. Moriyama, T., et al., Anti-damping spin transfer torque through epitaxial nickel oxide. Appl. Phys. Lett., 2015. **106**(16): p. 162406.

30. Ahmed, A.S., et al., Band gap narrowing and fluorescence properties of nickel doped SnO_2 nanoparticles. J. Lumin., 2011. **131**(1): p. 1-6.

31. Chukwuocha, E.O., M.C. Onyeaju, and T.S. Harry, Theoretical studies on the effect of confinement on quantum dots using the brus equation. World Journal of Condensed Matter Physics, 2012. **2**(02): p. 96.

32. Al-Sehemi, A.G., et al., Microwave synthesis, optical properties and surface area studies of NiO nanoparticles. J. Mol. Struct, 2014. **1058**: p. 56-61.

33. https://ars.els-cdn.com/content/image/3-s2.0-B9780081019757000038-f03-03-9780081019757.jpg.

34. Wikipedia. Moss-Burstein effect. 2020; Available from: https://en.wikipedia.org/wiki/Moss%E2%80%93Burstein_effect.

35. Lang, F., et al., Improved size-tunable synthesis of monodisperse NiO nanoparticles. Mater. Lett, 2016. **181**: p. 328-330.

36. Kortüm, G., Reflectance spectroscopy: principles, methods, applications. 2012: Springer Science & Business Media.

37. Dhineshbabu, N., et al., Study of structural and optical properties of cupric oxide nanoparticles. Appl. Nanosci., 2016. **6**(6): p. 933-939.

38. Saravanan, R., F. Gracia, and A. Stephen, Basic principles, mechanism, and challenges of photocatalysis, in Nanocomposites for visible light-induced photocatalysis. 2017, Springer. p. 19-40.

39. Wang, J., et al., Room-temperature ferromagnetism observed in Fe-doped NiO. Appl. Phys. Lett., 2005. **87**(20): p. 202501.

40. Layek, S. and H. Verma, Room temperature ferromagnetism in Mn-doped NiO nanoparticles. J. Magn. Magn. Mater., 2016. **397**: p. 73-78.

41. Tadić, M., et al., Unusual magnetic properties of NiO nanoparticles embedded in a silica matrix. J. Alloys Compd., 2011. **509**(25): p. 7134-7138.

42. Ichiyanagi, Y., et al., Magnetic properties of NiO nanoparticles. Physica B Condens, 2003. **329**: p. 862-863.

43. Thota, S. and J. Kumar, Sol–gel synthesis and anomalous magnetic behaviour of NiO nanoparticles. J Phys Chem Solids, 2007. **68**(10): p. 1951-1964.

44. Makhlouf, S.A., et al., Magnetic anomalies in NiO nanoparticles. J. Appl. Phys., 1997. **81**(8): p. 5561-5563.

45. Bi, H., et al., Ferromagnetic-like behavior of ultrafine NiO nanocrystallites. J. Magn. Magn. Mater., 2004. **277**(3): p. 363-367.

46. Rinaldi-Montes, N., et al., Interplay between microstructure and magnetism in NiO nanoparticles: breakdown of the antiferromagnetic order. Nanoscale, 2014. **6**(1): p. 457-465.

47. Li, L., et al., Magnetic crossover of NiO nanocrystals at room temperature. Appl. Phys. Lett., 2006. **89**(13): p. 134102.

48. Sugiyama, I., et al., Ferromagnetic dislocations in antiferromagnetic NiO. Nat. Nanotechnol., 2013. **8**(4): p. 266.

49. Tajiri, T., et al., Size dependence of crystal structure and magnetic properties of NiO nanoparticles in mesoporous silica. J. Phys. Chem. C, 2015. **119**(2): p. 1194-1200.

50. Gao, H., et al., Synthesis and anomalous magnetic behaviour of NiO nanotubes and nanoparticles. Micro Nano Lett., 2012. **7**(1): p. 5-8.

51. Meneses, C., et al., Competing interparticle interactions and surface anisotropy in NiO nanoparticles. J. Appl. Phys., 2010. **108**(1): p. 013909.

52. Ge, M., et al., Monodispersed NiO nanoflowers with anomalous magnetic behavior. Nanotechnology, 2010. **21**(42): p. 425702.

53. Gandhi, A.C., et al., Size confined magnetic phase in NiO nanoparticles. Mater. Res. Express, 2016. **3**(3): p. 035017.

54. Rinaldi-Montes, N., et al., Scrutinizing the role of size reduction on the exchange bias and dynamic magnetic behavior in NiO nanoparticles. Nanotechnology, 2015. **26**(30): p. 305705.

55. Shahzad, F., et al., Magnetic behavior of NiO nanoparticles determined by SQUID magnetometry. Mater. Res. Express, 2017. **4**(8): p. 086102.

56. Cooper, J., et al., Core/shell magnetism in NiO nanoparticles. J. Appl. Phys., 2013. **114**(8): p. 083906.

57. Lopez-Ortega, A., et al., Applications of exchange coupled bi-magnetic hard/soft and soft/hard magnetic core/shell nanoparticles. Phys. Rep., 2015. **553**: p. 1-32.

58. Ponnusamy, P., et al., Structural, optical and magnetic properties of undoped NiO and Fe-doped NiO nanoparticles synthesized by wet-chemical process. Mater. Charact., 2016. **114**: p. 166-171.

59. Mishra, A., S. Bandyopadhyay, and D. Das, Structural and magnetic properties of pristine and Fe-doped NiO nanoparticles synthesized by the co-precipitation method. Mater. Res. Bull., 2012. **47**(9): p. 2288-2293.

60. Mallick, P. and N. Mishra, Evolution of structure, microstructure, electrical and magnetic properties of nickel oxide (NiO) with transition metal ion doping. Am. J. Mater. Sci., 2012. **2**(3): p. 66-71.

61. Moura, K., et al., Tuning the surface anisotropy in Fe-doped NiO nanoparticles. Nanoscale, 2014. **6**(1): p. 352-357.

62. Paul, A. and B. Sanyal, Chemical and magnetic interactions in Mn-and Fe-codoped Ge diluted magnetic semiconductors. Phys. Rev. B, 2009. **79**(21): p. 214438.

63. Patel, K.N., et al., Effect of Mn doping concentration on structural, vibrational and magnetic properties of NiO nanoparticles. Adv Powder Technol, 2018. **29**(10): p. 2394-2403.

64. Khemprasit, J., et al., Effects of calcining temperature on structural and magnetic properties of nanosized Fe-doped NiO prepared by diol-based sol– gel process. J. Magn. Magn. Mater., 2011. **323**(18-19): p. 2408-2412.

65. Nadeem, K., et al., Effect of air annealing on structural and magnetic properties of Ni/NiO nanoparticles. J. Magn. Magn. Mater., 2016. **417**: p. 6-10.

66. Shahid, T., et al., Synthesis of pyramid-shaped NiO nanostructures using low-temperature composite-hydroxide-mediated approach. J Mater Sci and Eng, 2016. **5**(6): p. 6.

67. Nikolić, D., et al., Annealing-dependent structural and magnetic properties of nickel oxide (NiO) nanoparticles in a silica matrix. J. Eur. Ceram. Soc., 2015. **35**(14): p. 3843-3852.

68. Kodama, R.H., S.A. Makhlouf, and A.E. Berkowitz, Finite size effects in antiferromagnetic NiO nanoparticles. Phys. Rev. Lett., 1997. **79**(7): p. 1393.

69. Rinaldi-Montes, N., et al., Size effects on the Néel temperature of antiferromagnetic NiO nanoparticles. AIP Adv., 2016. **6**(5): p. 056104.

70. Pradeep, R., et al., Magnetic anomalies in Fe-doped NiO nanoparticle. Mater. Res. Express, 2017. **4**(9): p. 096103.

71. Sankar, S., et al., Photocatalytic properties of Mn-doped NiO spherical nanoparticles synthesized from sol-gel method. Optik, 2016. **127**(22): p. 10727-10734.

72. Srikesh, G. and A.S. Nesaraj, Chemical synthesis of Co and Mn co-doped NiO nanocrystalline materials as high-performance electrode materials for potential application in supercapacitors. Ceram. Int., 2016. **42**(4): p. 5001-5010.

73. Manna, S. and S. De, Magnetic properties of Li and Fe co-doped NiO. Solid State Commun., 2009. **149**(7-8): p. 297-300.

74. Madhu, G., K. Maniammal, and V. Biju, Defect induced ferromagnetic interaction in nanostructured nickel oxide with core–shell magnetic structure: the role of Ni 2+ and O 2− vacancies. Phys. Chem. Chem. Phys., 2016. **18**(17): p. 12135-12148.

75. Aragón, F., et al., Spin-glass-like behavior of uncompensated surface spins in NiO nanoparticulated powder. Physica B Condens, 2012. **407**(13): p. 2601-2605.

76. Duan, W., et al., Size effects on properties of NiO nanoparticles grown in alkalisalts. J. Phys. Chem. C, 2012. **116**(49): p. 26043-26051.

77. Iimori, T., et al., Magnetic moment distribution in nanosized antiferromagnetic NiO. J. Appl. Phys., 2020. **127**(2): p. 023902.

78. Popkov, S., et al., Size effects in the formation of an uncompensated ferromagnetic moment in NiO nanoparticles. J. Appl. Phys., 2019. **126**(10): p. 103904.

79. Wang, Y. and Y. Xia, Bottom-up and top-down approaches to the synthesis of monodispersed spherical colloids of low melting-point metals. Nano Lett., 2004. **4**(10): p. 2047-2050.

80. Rawat, R. Dense plasma focus-from alternative fusion source to versatile high energy density plasma source for plasma nanotechnology. in Journal of Physics: Conference Series. 2015. IOP Publishing.

81. Niederberger, M., Nonaqueous sol–gel routes to metal oxide nanoparticles. Acc. Chem. Res., 2007. **40**(9): p. 793-800.

82. Hu, C., et al., Composite-hydroxide-mediated approach as a general methodology for synthesizing nanostructures. J. Mater. Chem., 2009. **19**(7): p. 858-868.

83. Patterson, A., The Scherrer formula for X-ray particle size determination. Phy. Rev, 1939. **56**(10): p. 978.

84. https://images.app.goo.gl/qFvSzQUDE5osvfUt6.

85. Bardeen, J., L.N. Cooper, and J.R. Schrieffer, Theory of superconductivity. Phy. Rev, 1957. **108**(5): p. 1175.

86. Fagaly, R., Superconducting quantum interference device instruments and applications. Rev. Sci. Instrum., 2006. **77**(10): p. 101101.

87. Ricci, R.W., M. Ditzler, and L.P. Nestor, Discovering the Beer-Lambert Law. J. Chem. Educ., 1994. **71**(11): p. 983.

88. Wikipedia. Raman spectroscopy. 2019; Available from: https://en.wikipedia.org/wiki/Raman_spectroscopy.

89. Ninjas, P., Raman spectroscopy. 2020.

90. Wikipedia. Raman Spectroscopy. 2020; Available from: https://en.wikipedia.org/wiki/Raman_spectroscopy.

91. Yalçın, O., Ferromagnetic Resonance: Theory and Applications. 2013: BoD–Books on Demand.

92. Guerrero-Martínez, A., J. Pérez-Juste, and L.M. Liz-Marzán, Recent progress on silica coating of nanoparticles and related nanomaterials. Adv. Mater., 2010. **22**(11): p. 1182-1195.

93. Sun, W., et al., Specific role of polysorbate 80 coating on the targeting of nanoparticles to the brain. Biomaterials, 2004. **25**(15): p. 3065-3071.

94. Abramov, O., et al., Pilot scale sonochemical coating of nanoparticles onto textiles to produce biocidal fabrics. Surf. Coat. Technol., 2009. **204**(5): p. 718-722.

95. Kobayashi, Y., et al., Preparation and properties of silica-coated cobalt nanoparticles. J. Phys. Chem. B, 2003. **107**(30): p. 7420-7425.

96. Deng, Y.-H., et al., Investigation of formation of silica-coated magnetite nanoparticles via sol–gel approach. Colloids Surf. A Physicochem. Eng. Asp., 2005. **262**(1-3): p. 87-93.

97. Nadeem, K., et al., Effect of silica coating on the structural, dielectric, and magnetic properties of maghemite nanoparticles. J. Non·Cryst. Solids, 2014. **404**: p. 72-77.

98. Vaidya, S., et al., Synthesis of homogeneous NiO@ SiO_2 core– shell nanostructures and the effect of shell thickness on the magnetic properties. Cryst. Growth Des., 2009. **9**(4): p. 1666-1670.

99. Ramasami, A.K., M. Reddy, and G.R. Balakrishna, Combustion synthesis and characterization of NiO nanoparticles. Mater Sci Semicond Process, 2015. **40**: p. 194-202.

100. Duan, H., et al., Sub-3 nm NiO nanoparticles: Controlled synthesis, and photocatalytic activity. Mater. Lett, 2012. **81**: p. 245-247.

101. Wan, X., et al., Effects of catalyst characters on the photocatalytic activity and process of NiO nanoparticles in the degradation of methylene blue. Appl. Surf. Sci., 2013. **277**: p. 40-46.

102. Farzaneh, F. and S. Haghshenas, Facile synthesis and characterization of nanoporous NiO with folic acid as photodegredation catalyst for congo red. Mater. Sci. App., 2012. **3**(10): p. 697.

103. Li, X., et al., Controlling oxygen vacancies and properties of ZnO. Curr. Appl. Phys., 2014. **14**(3): p. 521-527.

104. Chaudhary, R.G., et al., Silica-coated nickel oxide a core-shell nanostructure: synthesis, characterization and its catalytic property in one-pot synthesis of malononitrile derivative. J Chinese Adv Mater Soc., 2017. **5**(2): p. 103-117.

105. Ali, A.M. and R. Najmy, Structural, optical and photocatalytic properties of NiO–SiO_2 nanocomposites prepared by sol–gel technique. Catal. Today, 2013. **208**: p. 2-6.

106. Akhtar, M.S., et al., Core-shell structured epoxide functional NiO/SiO_2 nanocomposite particles and photocatalytic decolorization of congo red aqueous solution. Colloids Surf. A Physicochem. Eng. Asp., 2017. **529**: p. 783-792.

107. Ullah, S., et al., Enhanced photocatalytic properties of core@ shell SiO_2@ TiO_2 nanoparticles. Appl. Catal. B, 2015. **179**: p. 333-343.

108. Sreethawong, T., S. Ngamsinlapasathian, and S. Yoshikawa, Surfactant-aided sol–gel synthesis of mesoporous-assembled TiO2–NiO mixed oxide nanocrystals and their photocatalytic azo dye degradation activity. Chem. Eng. J., 2012. **192**: p. 292-300.

109. Vinoth, R., et al., TiO_2–NiO p–n nanocomposite with enhanced sonophotocatalytic activity under diffused sunlight. Ultrason Sonochem, 2017. **35**: p. 655-663.

110. Mironova-Ulmane, N., et al. Raman scattering in nanosized nickel oxide NiO. in Journal of Physics: Conference Series. 2007. IOP Publishing.

111. Fukushima, H., et al., Evaluation of oxygen vacancies in ZnO single crystals and powders by micro-Raman spectroscopy. J. Ceram. Soc. JAPAN, 2017. **125**(6): p. 445-448.

112. Cazzanelli, E., et al., Study of vibrational and magnetic excitations in NicMg1− cO solid solutions by Raman spectroscopy. J. Condens. Matter Phys., 2003. **15**(12): p. 2045.

113. Nadeem, K., et al., Influence of SiO 2 matrix and annealing time on properties of Ni-ferrite nanoparticles. Solid State Sci., 2013. **19**: p. 27-31.

114. Meng, T., et al., The electrochemical capacitive behaviors of NiO nanoparticles. Electrochim. Acta, 2014. **125**: p. 586-592.

115. Nadeem, K., et al., Sol–gel synthesis and characterization of single-phase Ni ferrite nanoparticles dispersed in SiO2 matrix. J. Alloys Compd., 2010. **493**(1-2): p. 385-390.

116. Patel, K.N., et al., Structural and optical analysis of Fe doped NiO nanoparticles synthesized by chemical precipitation route. Mater. Res. Bull., 2018. **106**: p. 187-196.

117. Kremenović, A., et al., Temperature-induced structure and microstructure evolution of nanostructured Ni0. 9Zn0. 1O. J. Appl. Crystallogr., 2010. **43**(4): p. 699-709.

118. George, G. and S. Anandhan, Synthesis and characterisation of nickel oxide nanofibre webs with alcohol sensing characteristics. RSC Adv., 2014. 4(107): p. 62009-62020.

119. Mironova-Ulmane, N., et al. Structural and magnetic properties of nickel oxide nanopowders. in Solid State Phenomena. 2011. Trans Tech Publ.

120. Gandhi, A.C., et al., Short-range magnon excitation in NiO nanoparticles. J. Phys. Chem. C, 2013. **117**(36): p. 18666-18674.

121. Ravikumar, P., B. Kisan, and A. Perumal, Enhanced room temperature ferromagnetism in antiferromagnetic NiO nanoparticles. AIP Adv., 2015. **5**(8): p. 087116.

122. Patel, K.N., et al., Synthesis, structural and photoluminescence properties of nanocrystalline Cu doped NiO. Mater. Res. Express, 2017. **4**(10): p. 105027.

123. Arora, A.K., M. Rajalakshmi, and T. Ravindran, Phonon confinement in nanostructured materials, in Encyclopedia of Nanoscience and Nanotechnology. 2004, American Scientific Publishers. p. 499-512.

124. Wu, S.Y., Application of Raman Microscopy for Spin-Phonon Coupling & Magnon Excitation Study in Nanocrystals. 2012.

125. Zysler, R., et al., Surface effect in the magnetic order of antiferromagnetic nanoparticles. Physica B Condens, 2006. **384**(1-2): p. 277-281.

126. Abdelhalim, M.A.K., M.M. Mady, and M.M. Ghannam, Dielectric constant, electrical conductivity and relaxation time measurements of different gold nanoparticle sizes. Int. J. Phys. Sci., 2011. **6**(23): p. 5487-5491.

127. Rao, G.N., Y. Yao, and J. Chen, Superparamagnetic behavior of antiferromagnetic CuO nanoparticles. IEEE Trans. Magn., 2005. **41**(10): p. 3409-3411.

128. Tadić, M., et al., Synthesis and magnetic properties of concentrated α-Fe2O3 nanoparticles in a silica matrix. J. Alloys Compd., 2007. **441**(1-2): p. 291-296.

129. Cannas, C., et al., Superparamagnetic behaviour of γ-Fe 2 O 3 nanoparticles dispersed in a silica matrix. Phys. Chem. Chem. Phys., 2001. **3**(5): p. 832-838.

130. Moura, K., et al., Fe-doped NiO nanoparticles: synthesis, characterization, and magnetic properties. Revista Mexicana de Física, 2012. **58**(2): p. 167-170.

131. Rong, C.b., et al., Size-dependent chemical and magnetic ordering in L10-FePt nanoparticles. Adv. Mater., 2006. **18**(22): p. 2984-2988.

132. He, X. and H. Shi, Synthesis and anomalous magnetic properties of hexagonal CoO nanoparticles. Mater. Res. Bull., 2011. **46**(10): p. 1692-1697.

133. Wesselinowa, J., Size and anisotropy effects on magnetic properties of antiferromagnetic nanoparticles. J. Magn. Magn. Mater., 2010. **322**(2): p. 234-237.

134. Barbarić-Mikočević, V.D.-M.Ž. and K. Itrić, Kubelka-Munk theory in describing optical properties of paper (I). Technical Gazette, 2011. **18**(1): p. 117-124.

135. Franco Jr, A. and H. Pessoni, Effect of Gd doping on the structural, optical band-gap, dielectric and magnetic properties of ZnO nanoparticles. Physica B Condens, 2017. **506**: p. 145-151.

136. Hashem, M., et al., Fabrication and characterization of semiconductor nickel oxide (NiO) nanoparticles manufactured using a facile thermal treatment. Results Phys., 2016. **6**: p. 1024-1030.

137. Carbone, M., et al., NiO morphology dependent optical and electrochemical properties. Colloids Surf. A Physicochem. Eng. Asp., 2017. **532**: p. 178-182.

138. Fabbiyola, S., et al., Optical and magnetic properties of Ni-doped ZnO nanoparticles. J. Alloys Compd., 2017. **694**: p. 522-531.

139. Anandan, K. and V. Rajendran, Effects of Mn on the magnetic and optical properties and photocatalytic activities of NiO nanoparticles synthesized via the simple precipitation process. Mater Sci Eng B, 2015. **199**: p. 48-56.

140. Fazlali, F., A. reza Mahjoub, and R. Abazari, A new route for synthesis of spherical NiO nanoparticles via emulsion nano-reactors with enhanced photocatalytic activity. Solid State Sci., 2015. **48**: p. 263-269.

141. Lee, H., S. Koo, and J. Yoo, TiO2–SiO2 nanoparticles for suppressing photocatalytic activities and improving hydrophilicity. J. Ceram. Process. Res, 2012. **13**: p. S300-S303.

142. Miyashita, K., et al., Photo-Catalytic and Photo-Conductive Properties of SiO2/TiO2 Multiayer Film Prepared by Vacuum-Deposition Method. J. Ceram. Soc. JAPAN, 2002. **110**(1281): p. 450-454.

143. Buso, D., et al., Porous sol gel silica films doped with crystalline NiO nanoparticles for gas sensing applications. J. Sol-Gel Sci. Technol., 2006. **40**(2-3): p. 299-308.

144. Kamata, H., et al., Dispersed and high loading Ni catalyst stabilized in porous SiO2 matrix for substituted natural gas production. Catal. Today, 2018. **299**: p. 193-200.

145. Li, L., et al., Ultrafine cobalt oxide nanoparticles embedded in porous SiO2 matrix as efficient and stable catalysts for methane combustion. Mol. Catal., 2019.

146. Lv, X., T. Wang, and W. Jiang, Enhance photocatalysis of TiO2 and ZnO ceramics by addition of fused silica as a UV guiding medium. Ceram. Int., 2017. **43**(17): p. 15237-15245.

147. Wang, C., et al., Effect of oxygen vacancy on enhanced photocatalytic activity of reduced ZnO nanorod arrays. Appl. Surf. Sci., 2015. **325**: p. 112-116.

148. Tang, Y., et al., Visible-light-active ZnO via oxygen vacancy manipulation for efficient formaldehyde photodegradation. Chem. Eng. J., 2015. **262**: p. 260-267.

149. D'Arienzo, M., et al., Photogenerated defects in shape-controlled TiO2 anatase nanocrystals: a probe to evaluate the role of crystal facets in photocatalytic processes. J. Am. Chem. Soc., 2011. **133**(44): p. 17652-17661.

150. Pal, A., T. Jana, and K. Chatterjee, Silica supported TiO2 nanostructures for highly efficient photocatalytic application under visible light irradiation. Mater. Res. Bull., 2016. **76**: p. 353-357.

151. Batlle, X. and A.l. Labarta, Finite-size effects in fine particles: magnetic and transport properties. J PHYS D APPL PHYS, 2002. **35**(6): p. R15-R42.

152. Abarra, E., et al., Thermodynamic measurements of magnetic ordering in antiferromagnetic superlattices. Phys. Rev. Lett., 1996. **77**(16): p. 3451.

153. Makhlouf, S.A., H. Al-Attar, and R. Kodama, Particle size and temperature dependence of exchange bias in NiO nanoparticles. Solid State Commun., 2008. **145**(1-2): p. 1-4.

154. Sabyasachi, S., S. Majumdar, and S. Giri, Nanocrystallite interface effect and exchange bias phenomenology in Cr2O3 and NiO nanoparticles. Solid State Commun., 2011. **151**(21): p. 1515-1519.

155. Mottaghi, N., et al., Insights into the magnetic dead layer in La0. 7Sr0. 3MnO3 thin films from temperature, magnetic field and thickness dependence of their magnetization. AIP Adv., 2018. **8**(5): p. 056319.

156. Tejada, J., et al., Macroscopic resonant tunneling of magnetization in ferritin. Phys. Rev. Lett., 1997. **79**(9): p. 1754.

157. Vasilakaki, M., K.N. Trohidou, and J. Nogués, Enhanced magnetic properties in antiferromagnetic-core/ferrimagnetic-shell nanoparticles. Sci. Rep., 2015. **5**: p. 9609.

158. Ohldag, H., et al., Correlation between exchange bias and pinned interfacial spins. Phys. Rev. Lett., 2003. **91**(1): p. 017203.

159. Gandhi, A.C. and J.G. Lin, Exchange bias in finite sized NiO nanoparticles with Ni clusters. J. Magn. Magn. Mater., 2017. **424**: p. 221-225.

160. Mukadam, M., et al., Spin-glass behavior in ferromagnetic Fe [Fe (CN) 6]· x H 2 O nanoparticles. J. Appl. Phys., 2008. **103**(12): p. 123902.

161. Hrianca, I., C. Caizer, and Z. Schlett, Dynamic magnetic behavior of Fe 3 O 4 colloidal nanoparticles. J. Appl. Phys., 2002. **92**(4): p. 2125-2132.

162. Kong, I., et al. The effect of temperature on magnetic behavior of magnetite nanoparticles and its nanocomposites. in AIP Conference proceedings. 2009. AIP.

163. Zhang, D., et al., Magnetization temperature dependence in iron nanoparticles. Phys. Rev. B, 1998. **58**(21): p. 14167.

164. Caizer, C. and I. Hrianca, The temperature dependence of saturation magnetization of γ-Fe2O3/SiO2 magnetic nanocomposite. Annalen der Physik, 2003. **12**(1-2): p. 115-122.

165. Toby, B.H. and R.B. Von Dreele, GSAS-II: the genesis of a modern open-source all purpose crystallography software package. J. Appl. Crystallogr., 2013. **46**(2): p. 544-549.

166. Brok, E., et al., Polarized neutron powder diffraction studies of antiferromagnetic order in bulk and nanoparticle NiO. Phys. Rev. B, 2015. **91**(1): p. 014431.

167. Baran, S., et al., Size effects in antiferromagnetic NiO nanoparticles. Acta Phys. Pol., A, 2016. **129**: p. 35-39.

168. Fischer, G., et al., Exchange coupling in transition metal monoxides: Electronic structure calculations. Phys. Rev. B, 2009. **80**(1): p. 014408.

169. Balagurov, A., et al., Neutron diffraction study of microstructural and magnetic effects in fine particle NiO powders. physica status solidi (b), 2016. **253**(8): p. 1529-1536.

170. Nadeem, K., et al., Comparison of surface effects in SiO2 coated and uncoated nickel ferrite nanoparticles. Appl. Surf. Sci., 2014. **288**: p. 677-681.

171. Liu, D., D. Li, and D. Yang, Size-dependent magnetic properties of branchlike nickel oxide nanocrystals. AIP Adv., 2017. **7**(1): p. 015028.

172. Lin, Y.-H., et al., Ferromagnetism and electrical transport in Fe-doped NiO. Phys. Rev. B, 2006. **73**(19): p. 193308.

173. Patel, K.N., et al., Structural and optical analysis of Fe doped NiO nanoparticles synthesized by chemical precipitation route. Mater. Res. Bull., 2018.

174. Christy, A.J. and M. Umadevi, Novel combustion method to prepare octahedral NiO nanoparticles and its photocatalytic activity. Mater. Res. Bull., 2013. **48**(10): p. 4248-4254.

175. Sankar, S., et al., Photocatalytic properties of Mn-doped NiO spherical nanoparticles synthesized from sol-gel method. Optik-International Journal for Light and Electron Optics, 2016. **127**(22): p. 10727-10734.

176. Liu, S., et al., Synthesis of Fe-doped NiO nanofibers using electrospinning method and their ferromagnetic properties. J. Magn. Magn. Mater., 2012. **324**(13): p. 2070-2074.

177. Chen, Y., B. Peng, and B. Wang, Raman spectra and temperature-dependent Raman scattering of silicon nanowires. J. Phys. Chem. C, 2007. **111**(16): p. 5855-5858.

178. Vivek, S., P. Arunkumar, and K.S. Babu, In situ generated nickel on cerium oxide nanoparticle for efficient catalytic reduction of 4-nitrophenol. RSC Adv., 2016. **6**(51): p. 45947-45956.

179. Grimsditch, M., S. Kumar, and R. Goldman, A Brillouin scattering investigation of NiO. J. Magn. Magn. Mater., 1994. **129**(2-3): p. 327-333.

180. Gandhi, A.C., et al., Growth mechanism and magnon excitation in NiO nanowalls. Nanoscale Res. Lett., 2011. **6**(1): p. 485.

181. Tadic, M., et al., NiO core–shell nanostructure with ferromagnetic-like behavior at room temperature. J. Alloys Compd., 2014. **586**: p. S322-S325.

182. Kisan, B., et al., Finite size effects in magnetic and optical properties of antiferromagnetic NiO nanoparticles. IEEE Trans. Magn., 2014. **50**(1): p. 1-4.

183. Khadar, M.A., V. Biju, and A. Inoue, Effect of finite size on the magnetization behavior of nanostructured nickel oxide. Mater. Res. Bull., 2003. **38**(8): p. 1341-1349.

184. Raja, S.P. and C. Venkateswaran, Investigation of magnetic behaviour of Ni–Fe–O prepared by the solid state method. J. Phys. D Appl. Phys., 2009. **42**(14): p. 145001.

185. He, J., et al., Exchange bias and the origin of room-temperature ferromagnetism in Fe-doped NiO bulk samples. J. Appl. Phys., 2008. **103**(2): p. 023906.

186. Douvalis, A., L. Jankovic, and T. Bakas, The origin of ferromagnetism in 57Fe-doped NiO. J. Condens. Matter Phys., 2007. **19**(43): p. 436203.

187. Zener, C., Interaction between the d-shells in the transition metals. II. Ferromagnetic compounds of manganese with perovskite structure. Phy. Rev, 1951. **82**(3): p. 403.

188. Kahouli, M., et al., Structural and optical properties of ZnO nanoparticles prepared by direct precipitation method. Superlattices Microstruct., 2015. **85**: p. 7-23.

189. Anandan, K. and V. Rajendran, Morphological and size effects of NiO nanoparticles via solvothermal process and their optical properties. Mater Sci Semicond Process, 2011. **14**(1): p. 43-47.

190. Sanyal, B., et al., Inhomogeneity in Co doped ZnO diluted magnetic semiconductor. J. Appl. Phys., 2008. **103**(7): p. 07D131.

191. Kang, J.-S., et al., Spatial chemical inhomogeneity and local electronic structure of Mn-doped Ge ferromagnetic semiconductors. Phys. Rev. Lett., 2005. **94**(14): p. 147202.

192. Dinesha, M., et al., Structural, electrical and magnetic properties of Co and Fe co-doped ZnO nanoparticles prepared by solution combustion method. J. Alloys Compd., 2010. **490**(1-2): p. 618-623.

193. Ashokkumar, M. and S. Muthukumaran, Electrical, dielectric, photoluminescence and magnetic properties of ZnO nanoparticles co-doped with Co and Cu. J. Magn. Magn. Mater., 2015. **374**: p. 61-66.

194. Beltrán, J., et al., Magnetic properties of Fe doped, Co doped, and Fe+ Co co-doped ZnO. J. Appl. Phys., 2013. **113**(17): p. 17C308.

195. Jayakumar, O., et al., Magnetic properties of hydrogenated Li and Co doped ZnO nanoparticles. Appl. Phys. Lett., 2006. **89**(20): p. 202507.

196. Okabayashi, J., et al., Fabrication and magnetic properties of Fe and Co co-doped ZrO2. AIP Adv., 2011. **1**(4): p. 042138.

197. Sen, A., et al., Influence of Ba and Mo co-doping on the structural, electrical, magnetic and optical properties of BiFeO 3 ceramics. Mater. Res. Express, 2020.

198. Paul, A., Low-angle polarized neutron and X-ray scattering from magnetic nanolayers and nanostructures. Vol. 273. 2017: Springer.

199. Mirzoev, A., M. Yalalov, and D. Mirzaev, Energy of mixing and magnetic state of components of Fe-Mn alloys: A first-principles calculation for the ground state. Phys. Met. Metallogr., 2006. **101**(4): p. 341-348.

200. Kulikov, N. and C. Demangeat, Spin polarization of disordered Fe-Cr and Fe-Mn alloys. Phys. Rev. B, 1997. **55**(6): p. 3533.

201. Lintzen, S., et al., The Fe–Mn enthalpy phase diagram from first principles. J. Alloys Compd., 2013. **577**: p. 370-375.

202. Umebayashi, H. and Y. Ishikawa, Antiferromagnetism of γ Fe-Mn alloys. J. Phys. Soc. Jpn., 1966. **21**(7): p. 1281-1294.

203. Perumal, A., Study of Magnetic Properties of Amorphous Fe-Mn-Zr Alloys. Proc. Indian National Sci. Acad., 2006. **72**(1): p. 43.

204. Abbas, H., et al., Enhanced Photocatalytic activity of ferromagnetic Fe-doped NiO Nanoparticles. Optik, 2019: p. 163637.

205. Al Boukhari, J., et al., Structural, optical and magnetic properties of pure and rare earth-doped NiO nanoparticles. Appl. Phys. A, 2020. **126**: p. 1-13.

206. Zorkipli, N.N.M., N.H.M. Kaus, and A.A. Mohamad, Synthesis of NiO nanoparticles through sol-gel method. Procedia Chem., 2016. **19**: p. 626-631.

207. El-Kemary, M., N. Nagy, and I. El-Mehasseb, Nickel oxide nanoparticles: synthesis and spectral studies of interactions with glucose. Mater Sci Semicond Process, 2013. **16**(6): p. 1747-1752.

208. Mallick, P., C. Sahoo, and N. Mishra. Structural and Optical Characterization of NiO nanoparticles synthesized by sol-gel route. in AIP Conference Proceedings. 2012. American Institute of Physics.

209. Datt, G., C. Kotabage, and A. Abhyankar, Ferromagnetic resonance of $NiCoFe_2O_4$ nanoparticles and microwave absorption properties of flexible NiCoFe 2 O 4–carbon black/poly (vinyl alcohol) composites. Phys. Chem. Chem. Phys., 2017. **19**(31): p. 20699-20712.

210. Hernández-Gómez, P., et al., Synthesis, structural characterization and broadband ferromagnetic resonance in Li ferrite nanoparticles. J. Alloys Compd., 2018. **765**: p. 186-192.

211. Rossing, T.D., Resonance linewidth and anisotropy variation in thin films. J. Appl. Phys., 1963. **34**(4): p. 995-995.

212. Hickey, M.C. and J.S. Moodera, Origin of intrinsic Gilbert damping. Phys. Rev. Lett., 2009. **102**(13): p. 137601.

213. Azzawi, S., A. Hindmarch, and D. Atkinson, Magnetic damping phenomena in ferromagnetic thin-films and multilayers. J. Phys. D Appl. Phys., 2017. **50**(47): p. 473001.

214. Safonov, V.L. and H.N. Bertram, Impurity relaxation mechanism for dynamic magnetization reversal in a single domain grain. Phys. Rev. B, 2000. **61**(22): p. R14893.

215. Silberglitt, R., Effect of spin waves on the phonon energy spectrum of a heisenberg ferromagnet. Phy. Rev, 1969. **188**(2): p. 786.

216. McMichael, R.D., et al., Ferromagnetic resonance mode interactions in periodically perturbed films. J. Appl. Phys., 2002. **91**(10): p. 8647-8649.

217. Hartmann-Boutron, F., Effect of Rare-Earth Impurities on the Ferrimagnetic Resonance and Nuclear Relaxation in Yttrium Iron Garnet. J. Appl. Phys., 1964. **35**(3): p. 889-891.

218. Suhl, H., Theory of the magnetic damping constant. IEEE Trans. Magn., 1998. **34**(4): p. 1834-1838.

219. Layek, S. and H. Verma, Room temperature ferromagnetism in Mn-doped NiO nanoparticles. J. Magn. Magn. Mater., 2016. **397**: p. 73-78.

220. Soni, S., et al., Structural, optical and magnetic properties of Fe-doped CeO_2 samples probed using X-ray photoelectron spectroscopy. J. Mater. Sci. Mater., 2018. **29**(12): p. 10141-10153.

221. Phokha, S., S. Pinitsoontorn, and S. Maensiri, Structure and magnetic properties of monodisperse Fe 3+-doped CeO_2 nanospheres. Nanomicro Lett, 2013. **5**(4): p. 223-233.

222. Wen, Q.-Y., et al., Room-temperature ferromagnetism in pure and Co doped CeO2 powders. J. Condens. Matter Phys., 2007. **19**(24): p. 246205.

223. Thurber, A., et al., Ferromagnetism in chemically synthesized CeO_2 nanoparticles by Ni doping. Phys. Rev. B, 2007. **76**(16): p. 165206.

224. Winkler, E., et al., Surface anisotropy effects in NiO nanoparticles. Phys. Rev. B, 2005. **72**(13): p. 132409.

225. Gandhi, A.C., J. Pant, and S.Y. Wu, Dense inter-particle interaction mediated spontaneous exchange bias in NiO nanoparticles. RSC Adv., 2016. **6**(3): p. 2079-2086.

226. Gandhi, A.C., et al., Strong Pinned-Spin-Mediated Memory Effect in NiO Nanoparticles. Nanoscale Res. Lett., 2017. **12**(1): p. 1-8.

227. Hutchings, M.T. and E. Samuelsen, Measurement of spin-wave dispersion in NiO by inelastic neutron scattering and its relation to magnetic properties. Phys. Rev. B, 1972. **6**(9): p. 3447.